

Surface Study of Niobium
for Superconducting Radio Frequency (SRF) Accelerators

Hui Tian

Jinchang City, Gansu Province, China

Ph.D Candidate, Tsinghua University, 2000
Master of Science, Guangxi University, 1999
Bachelor of Science, Central South University, 1997

A Dissertation presented to the Graduate Faculty
of the College of William and Mary in Candidacy for the Degree of
Doctor of Philosophy

Department of Applied Science/Materials Science

The College of William and Mary
August, 2008

APPROVAL PAGE

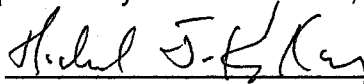
This "Dissertation" is submitted in partial fulfillment of
the requirements for the degree of

Doctor of Philosophy

Hui Tian


Hui Tian.

Approved by the Committee, May 20, 2008

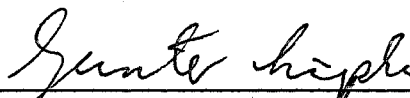


Committee Chair

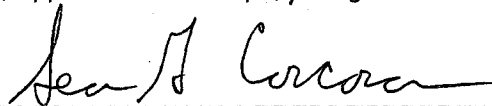
Dr. Michael J. Kelley, Applied Science Dept., College of William and Mary



Dr. Charles E. Reece, SRF Institute, Jefferson Lab



Dr. Gunter Luepke, Applied Science Dept., College of William and Mary



Dr. Sean G. Corcoran, MSE Dept., Virginia Tech University

ABSTRACT PAGE

Niobium rf superconductivity is a near-surface phenomenon because of the shallow rf penetration depth. Accordingly, the performance of Nb SRF accelerator cavities is strongly impacted by the topmost few nanometers interior surface, especially as impacted by the final surface conditioning treatments.

Surface topography impacts performance through local loss of superconductivity caused by intrusion of the rf magnetic field, which is enhanced at sharp protrusions. "Sharpness" comprises both vertical and lateral aspects, requiring development a new characterization approach beyond the familiar roughness measurements (R_a , R_z), which view only the vertical component. Stylus profilometry and atomic force microscopy traces view surface topography from mm size to near atomic dimensions. Power spectral density analysis combines data across this whole dimensional scale, so that the effect of preparation variables on topography has been studied systematically for the first time.

Surface chemistry impacts performance through the presence of a complex surface oxide structure and the response of the surface to post-treatments, notably low temperature baking (e.g., 125°C, 24 hrs). Previous XPS studies consistently found that the surface chiefly comprises a few nm of Nb₂O₅ on top of Nb metal, with small amount of Nb suboxides near the interface. Efforts to unambiguously discern the variation of composition with depth in the surface region by angle-resolved XPS have been confounded by the effect of surface roughness. The problem was avoided here by, for the first time, using a synchrotron source to vary x-ray photon energy at fixed take-off angle, obtaining a range of sample depths in a fixed column of material spanning the oxide layer thickness. One result is that variation of etching practice chiefly affects the thickness of the top Nb₂O₅ layer, but the sub-oxide accommodation zone at the interface remains substantially constant. A second is that low temperature baking in vacuum results in significant thinning and reduction of the oxide layer, which is completely recovered on subsequent air exposure without loss of the SRF performance improvement.

The effect of the most commonly employed treatment-BCP on polycrystalline niobium sheet over a range of realistic solution flow rates has been examined through multiple surface characterization techniques. The surface exhibits micron-scale roughness, whose extent does not change with treatment conditions. The outermost surface consists of a few-nm thick layer of Nb₂O₅, whose thickness increases with solution flow rate to a maximum of 1.3~1.4 times that resulting from static solution.

Electropolishing is believed to be an effective technique to treat niobium cavity surfaces for achieving reproducibly high performance SRF cavities. However the operation condition is basically optimized through practical processing. By using improved electrochemical techniques, the temperature, flow rate and HF concentration dependence of each potential were identified. The first use of electrochemical impedance spectroscopy (EIS) on this system was reported. EIS results are consistent with the compact salt film mechanism for niobium electropolishing in hydrofluoric sulfuric acid electrolyte and do not support either the porous salt film or the adsorbate-acceptor mechanism.

Dedicated to my parents, Guilan Li & Hailin Tian

TABLE OF CONTENTS

Acknowledgements.....	ix
List of Tables.....	x
List of Figures.....	xi
CHAPTER 1 Introduction.....	2
1.1. Motivation.....	2
1.2. Organization of the Dissertation.....	8
1.3. References.....	10
CHAPTER 2 Surface Topography Studies of Niobium.....	16
2.1. Introduction.....	16
2.2. Experimental Studies.....	18
2.2.1: Sample Preparation.....	18
2.2.2: Surface Topography Measurement.....	20
2.2.2.1. Stylus Profilometry.....	20
2.2.2.2. Atomic Force Microcopy (AFM).....	21
2.2.2.3. Power Spectral Density (PSD).....	23
2.3. Results and Discussion.....	25

2.3.1. Surface Topography of BCP/EP Single Crystal and Polycrystalline Nb	25
2.3.2. Surface Topography with Incremental BCP/EP Treatment	28
2.4. Conclusions	30
2.5. References	32
CHAPTER 3 XPS Studies of Niobium Surface Oxide	46
3.1. Introduction	46
3.2. Experimental Studies	51
3.2.1: Sample Preparation	51
3.2.2: Surface Chemistry	52
3.2.2.1. X-ray Photon-electron Spectroscopy (XPS)	52
3.2.2.2. Depth profiling–Angle Resolved XPS (ARXPS) & Variable Energy XPS	53
3.2.2.3. Variable Photon Energy XPS with Synchrotron Radiation	55
3.2.2.4. Peak Fitting	57
3.3. Results and Discussion	61
3.3.1. Surface Depth Profiling-ARXPS and Variable Energy XPS	61
3.3.2. Surface Oxide Before and After Low T Baking	63
3.3.2.1. Effect of Baking Temperature	64
3.3.3.2. Effect of Baking Duration	65
3.3.3.3. Effect of Air Baking	66

3.4. Conclusions.....	67
3.5. References.....	68

CHAPTER 4 Surface Study of Niobium Buffered Chemical

Polished (BCP) under Conditions for SRF

Cavity Production.....	89
4.1. Introduction.....	89
4.2. Experimental Studies.....	91
4.2.1. Sample Preparation.....	91
4.2.2. Surface Orientation.....	92
4.2.3. Surface Profilometry	93
4.2.4. Laboratory X-ray Photon-electron Spectroscopy (XPS).....	93
4.2.5. Synchrotron X-ray Photoelectron Spectroscopy.....	94
4.3. Results and Discussion.....	94
4.3.1. Surface Orientation.....	94
4.3.2. Reproducibility of Topography and Surface Chemistry Results.....	95
4.3.3. Effect of Solution Flow Rate.....	97
4.4. Conclusions.....	99
4.5. References.....	101

CHAPTER 5 Novel Characterization of the Electropolishing

of Nb with a Hydrofluoric and Sulfuric Acid

Electrolyte.....	112
5.1. Introduction	112
5.2. Electropolishing Fundamentals.....	114
5.2.1. Electrochemical Cell of Niobium Electropolishing.....	114
5.2.2. Electrical Double Layer.....	115
5.2.3. Anode Polarization Curve of Niobium Electropolishing.....	116
5.2.4. Electrochemical Impedance Spectroscopy (EIS).....	121
5.3. Experimental Procedures.....	124
5.4. Results	125
5.4.1. Polarization Behavior.....	125
5.4.2. Area Ratio of Anode and Cathode.....	126
5.4.3. Effect of HF Volume Concentration.....	127
5.4.4. Effect of Electrolyte Temperature.....	128
5.4.5. Impedance Experiments.....	129
5.5. Discussion.....	130
5.6. Conclusions.....	135
5.7. References.....	136
Vita.....	154

ACKNOWLEDGEMENT

I wish to express my first and foremost thanks to my advisors, Dr. Michael J. Kelley and Dr. Charles E. Reece, not only for their encouragements, advices and mentoring throughout my doctoral studies at the College of William and Mary, but also for all that they have shared with me over the years that I know will benefit me in many ways throughout my career. Without their support and guidance, this work would not have been done.

My sincere gratefulness goes to my doctoral dissertation committee member, Dr. Sean G. Corcoran, for his inspired visions and suggestions about this work, and his comments during the course of completing manuscripts and this dissertation. I would also like to express my thanks to my doctoral dissertation committee member, Dr. Gunter Lüpke, for agreeing to serve. I really appreciate his comments on this dissertation.

I wish to express my sincere gratitude to our research group members for their friendships and collective encouragements to finish this dissertation, especially to Zhengmao Zhu, for his help to troubleshoot the “OLD” XPS on the weekends, and Binping Xiao, for his kindness support for taking some of night-shifts at X1B with an empty stomach. I am fortunate to have the opportunity to work with a group of energetic people in Dr. Kelvin E. Smith’s lab of Boston University at X1B, NSLS of BNL. They are: Dr. Cormac McGuinness, Dr. Per Anders Glans, Dr. Lukasz Plucinski, Dr. Shangcai Wang, Dr. Yufeng Zhang, Dr. Louis Piper, and Alexander DeMasi. I have enjoyed every moment that we have worked together at the X1B without knowing day or night and we desperately hunted for an eatable Chinese restaurant at the “rural” Long Island.

I also want to acknowledge the exceptional support of SRF institute of Jefferson lab, especially to Carolyn Camp, Dr. Gigi Ciovati, Anne-Marie Valente-Feliciano, Dr. Rongli Geng, Dr. Peter Kneisel, Dr. John Mammoss, Dr. Larry Philips, Dr. Joan Thomas and Will Sommer. I want to thank the support of the department of Applied Science and the Applied Research Center, especially to Natalie Percy, Olga Trofimova Amy L. Wilkerson and Lydia C. Whitaker. Thanks go to Guilhem Ribeill of North Carolina State University for his diligent work on surface topographic measurements and PSD developments during his SUUI Internship at the Jefferson lab.

Finally, I wish to express my deepest gratitude to my family. Thanks to my mother, father, and sister, for believing in me, encouraging me, and selflessly supporting me. Your constant love has always been the source of my strength and motivation. Special thanks to my husband, Xin Zhao, for his years love, understanding and support.

LIST OF TABLES

Table 3.1: Reported binding energy positions of the Nb3d _{3/2-5/2} doublets (unit: eV)	76
Table 3.2: The parameters in TPP-2M equation used for calculating the inelastic mean free path (IMFP) for Nb ₂ O ₅ at the different photon energy . (Curtsey of S. Tanuma, C.J. Powell, D.R. Penn, Surf. Interf. Anal., Vol. 17, 1991, pp. 911, S. Tanuma, C.J. Powell, D.R. Penn, Surf. Interf. Anal., Vol, 17, 1991, pp. 927 and W. H. Gries, Surf. Interf. Anal., 24, 1996, pp. 38.)	78
Table 5.1: Characteristic features of Nyquist diagram expected for various EP models obtained from the high frequency loops (Curtsey of M. Matlosz, S. Magaino and D. Landolt, J. Electrochem. Soc., Issue 2, Vol. 141, 1994, pp. 410 and M. Matlosz, Electrochimica Acta. Issue 4, Vol. 40, 1995, pp. 393.)	153

LIST OF FIGURES

Figure 1-1: Q vs. E_{acc} for an electropolished niobium 9-cell cavity. The acceleration gradient reaches $32 MV/m$. Courtesy of Jefferson lab.

.....13

Figure 1-2: A schematic illustration of electric and magnetic field distributions in a typical single-cell SRF cavity (From <http://www.lns.cornell.edu/public/CESR/SRF>. Reprinted with permission of Cornell University).

.....14

Figure 1-3: Surface electric field and magnetic field as a function of distance from equator ($E_{pk} = 1 MV/m$) (From J. Knobloch, PhD thesis, 1997. Reprinted with permission of Cornell University).

.....15

Figure 2.1: Optical images of the polycrystal niobium surface after a) BCP and c) EP etch, and single crystal niobium surface after b) BCP and d) EP etch. (Bar in the lower right of Figures 2.1 a and b represents $20 \mu m$; Bar in the lower right of Figures 2.1 c and d represents $50 \mu m$).

.....35

Figure 2.2: AFM images of a) BCP treated single crystal niobium ($20\ \mu\text{m} \times 20\ \mu\text{m}$), and b) EP treated single crystal niobium ($40\ \mu\text{m} \times 40\ \mu\text{m}$).

.....36

Figure 2.3: RMS roughness values computed from AFM and profilometer data taken at different scan lengths ($20\ \mu\text{m} \times 20\ \mu\text{m}$, $50\ \mu\text{m} \times 50\ \mu\text{m}$, and $100\ \mu\text{m} \times 100\ \mu\text{m}$ by AFM; $200\ \mu\text{m} \times 200\ \mu\text{m}$ and $1000\ \mu\text{m} \times 1000\ \mu\text{m}$ by stylus profilometry) for different treatments (blue: ground + 5 mins BCP; dark purple: light BCP; green: heavy BCP; light purple: ground + 30 mins EP).

.....37

Figure 2.4: Combined AFM and profilometer power spectral densities from all scan sizes (purple: $20\ \mu\text{m} \times 20\ \mu\text{m}$; magenta : $50\ \mu\text{m} \times 50\ \mu\text{m}$; red: $100\ \mu\text{m} \times 100\ \mu\text{m}$ - by AFM; dark blue: $200\ \mu\text{m} \times 200\ \mu\text{m}$; blue: $1000\ \mu\text{m} \times 1000\ \mu\text{m}$ -by stylus profilometry) from the sample having undergone 5 minutes of BCP treatment. (Adapt from H. Tian, M. J. Kelley, S. C. Cocoran, and C. E. Reece, "Proc. of 13th SRF workshop", Beijing, China, 2007, WE104

<http://www.pku.edu.cn/academic/srf2007/proceeding.html>).

.....38

Figure 2.5: PSD spectra from scan sizes ($20\ \mu\text{m} \times 20\ \mu\text{m}$ by AFM and $1000\ \mu\text{m} \times 1000\ \mu\text{m}$ by stylus profilometry) for the different polishing methods (blue: 5mins BCP; red: light BCP; green: heavy BCP; black: 30 mins EP performed on a mechanically ground sample. (Adapt from H. Tian, M. J. Kelley, S. C. Cocoran, and

C. E. Reece, "Proc. of 13th SRF workshop", Beijing, China, 2007, WE104, <http://www.pku.edu.cn/academic/srf2007/proceeding.html>).

.....39

Figure 2.6: The corresponding AFM images for Figure 2.5 were measured at $50 \mu\text{m} \times 50 \mu\text{m}$ scan area with 6000 nm data scale in vertical direction for "untreated" (a), light BCP (b) and heavy BCP samples (c), $100 \mu\text{m} \times 1000 \mu\text{m}$ scan area with 3000 nm data scale in vertical direction for 30 minutes EP sample (d).

.....40

Figure 2.7: Power spectral density plots (a: $1000 \mu\text{m} \times 1000 \mu\text{m}$ by stylus profilometry, b: $100 \mu\text{m} \times 100 \mu\text{m}$ by AFM, c: $20 \mu\text{m} \times 20 \mu\text{m}$ by AFM) of 90 mins electropolished samples that have undergone different duration BCP etch (green: ground sample; red: light BCP; blue: heavy BCP)

.....41

Figure 2.8: Power spectral density plots (a: $100 \mu\text{m} \times 100 \mu\text{m}$ by AFM; $1000 \mu\text{m} \times 1000 \mu\text{m}$ by stylus profilometry) for incremental electropolished ground niobium sample (red: ground sample; purple: 30 mins EP; green: 60 mins EP; magenta: 90 mins EP)

.....42

Figure 2.9: The corresponding AFM images ($100 \mu\text{m} \times 100 \mu\text{m}$) for Figure 2.8.

.....43

Figure 2.10: RMS roughness values computed from AFM data taken at different scan lengths ($20 \mu\text{m} \times 20 \mu\text{m}$, $50 \mu\text{m} \times 50 \mu\text{m}$, and $100 \mu\text{m} \times 100 \mu\text{m}$) for ground sample after different step EP etch.

.....44

Figure 2.11: Power spectral density plots (dot : $100 \mu\text{m} \times 100 \mu\text{m}$ by AFM; square: $1000 \mu\text{m} \times 1000 \mu\text{m}$ by stylus profilometry) for ground sample after different temperature (red: $T=24^\circ\text{C}$, blue: $T=30^\circ\text{C}$) EP etch , (Adapt from H. Tian, M. J. Kelley, S. C. Cocoran, and C. E. Reece, “Proc. of 13th SRF workshop”, Beijing, China ,2007, WE104, <http://www.pku.edu.cn/academic/srf2007/proceeding.html>).

.....45

Figure 3-1: A wide range spectrum of a buffed chemical polishing BCP treated single crystal niobium collected at 45° take off angle relative to the surface normal with monochromated Al anode.

.....77

Figure 3.2: A schematic diagram of the arrangement of the components used at the beamline X1B, NSLS.

.....79

Figure 3.3: $Nb\ 3d$ spectra of BCP treated single crystal collected using $930\ eV$ at take off angles 0° (red), 41° (blue) and 60° (olive) relative to the surface normal.

.....80

Figure 3.4: *Nb 3d* spectra of BCP treated single crystal collected at 0° take off angle relative to the surface normal using 300 eV (a), 550 eV (b) and 930 eV (c) photons. (The full line indicates the simulation and the dots represent various components)

.....81

Figure 3.5: a) BCP and b) EP single crystal *Nb 3d* spectra before (blue) and after (red) low T baking (120°C, 48 hrs, 10⁻⁹ torr). The top *Nb₂O₅* layer is partially transformed to suboxides, evident decreased *Nb⁵⁺* associated doublet intensity and increased of suboxides-associated peaks.

.....82

Figure 3.6: *Nb 3d* spectra before (red), after 120°C for 12 hrs (blue), and 165°C for 3 hrs (olive) *in-situ* baking. 160°C, 3hrs baking causes almost the same amount of *Nb₂O₅* to transform to suboxides as that of 120°C, 12 hrs .

.....83

Figure 3.7: *Nb 3d* spectra before (black), after 120°C for 12 hrs (red), and 165°C for 12 hrs (olive) *in-situ* baking. A long baking duration for higher temperature produces more *Nb₂O₅* transformation.

.....84

Figure 3.8: The intensity ratio of $\frac{I_{Nb_2O_5}}{\sum I_{Nb}}$ decreases with the baking duration, the

intensity ratio of $\frac{I_{Nb_{suboxides}}}{\sum I_{Nb}}$ increases with the baking duration.

.....85

Figure 3.9: The intensity ratio of $I_{Nb^{2+}(0<rs>5)} / \sum I_{Nb}$ decreases with the baking duration.
.....86

Figure 3.10: *Nb 3d* spectra after over 8 hrs air-exposure (*in situ* baked at different duration—black: before baking; red: 3hrs bake-out; blue: 12 hrs bake-out). The change of oxide layer associated with Nb_2O_5 transformation disappeared and the spectra cannot be distinguished from those obtained prior to baking
.....87

Figure 3.11: *Nb 3d* spectra before (blue), after 120°, 24 hrs *in situ* baking (red) and air baking (black). Air baking at 120°C produces a thicker Nb_2O_5 layer (4~4.5 nm) than that of *in-situ* baking.
.....88

Figure 4.1: The rotating "Teflon" fixture to provide constant surface flow rate etching for multiple specimens.
.....104

Figure 4.2: Optical image of the niobium surface after static BCP etch. Bar in the lower right represents 200 mm. (Optical microscopy image was taken by Institute of Laser Technology, Aachen, Germany).
.....105

Figure 4.3: Pole figures obtained by EBSD from a 1.5 x 1.5 mm field after static BCP etching (The sample normal direction is located in the center of the pole figures. The RD and

TD direction are arbitrary in this case. The scale value on the bar is in the units of times random)

.....106

Figure 4.4: Map of grain orientations after static BCP etching from the same field as Figure 3.3. The grain maps show grains randomly colored to the highlight size and shape .

.....107

Figure 4.5: Components of Nb 3d manifold (The dot indicate the collected spectrum. The full line-black, indicates the simulation. The components of Nb 3d are: pink: Nb₂O₅; blue: NbO₂; light blue: NbO; green: Nb₂O; dark yellow: Nb), adapted from From H. Tian, C. Reece, and M. Kelley, *Proceedings of the 11th Workshop on RF Superconductivity 2003*. Reprint with permission of DESY, Germany)

.....108

Figure 4.6: The effect of flow rate on the surface roughness (RMS:μm), error bars correspond to one standard deviation. No significant effect on surface roughness at the different flow rate can be observed.

.....109

Figure 4.7: Comparison of Nb 3d region photoelectron spectra of static (red) vs. flowing BCP etching (blue) polycrystal Nb (They were collected 0° takeoff angle relative to surface normal by using 930 eV photon energy-X1B beamline, NSLS, BNL)

.....110

Figure 4.8: The effect of flow rate on the surface chemistry ($I^{Nb_{s+}} / I_{Nb_{Total}}$) a significant effect on surface chemistry at the different flow rate can be observed, which is much larger than the difference associated with sample-to-sample variation.

.....111

Figure 5.1: The Nb electropolishing cell set up and data acquisition scheme.

.....139

Figure 5.2: Double layer formed at the electrode-electrolyte interface (From A. J. Bard, and L. R. Faulkner, *Electrochemical Methods Fundamentals and Applications*, 2nd edition, 2001. Reprint with the permission of John Wiley & Sons, Inc)

.....140

Figure 5.3: Typical polarization behavior for the Nb-Al system in HF (49%): H₂SO₄ (96%) = 1: 9 (volume ratio) at 31.5 °± 1.5 C.

.....141

Figure 5.4: Horizontal EP set-up developed at KEK. (From K. Satio, Y. Kojima, T. Furuya, S. Mitsunobu, S. Noguchi, K. Hosoyama, T. Nakazato, T. Tajima, K. Asano, K. Inoue, Y. Iino, H. Nomura and K. Takeuchi, *Proc. of 4th SRF workshop*, Vol .2, 1989. Reprint with permission of KEK, Tsukuba, Japan)

.....142

Figure 5.5: Polarization curves were determined for the different area ratio Nb and Al in 1:9 HF (49%): H₂SO₄ (96%). Above: cathode area kept constant; below: anode area kept constant).

.....143

Figure 5.6: Polarization curves were determined for the Nb-Al system in different volume ratios of HF (49%): H₂SO₄ (96%).
.....144

Figure 5.7: The anode plateau current density decreases with decreasing HF volume ratio. A typical 1:9 volume ratio HF and H₂SO₄ corresponds to 0.111. The data plotted below corresponds to the current density at the anode voltage of 6 V from Figure 5.6.
.....145

Figure 5.8: Anode (a) and cathode (b) polarization curves determined for Nb in HF (49%): H₂SO₄ (96%) = 1: 9 (volume ratio) at 54.6 °C, 45.6 °C, 33.5 °C, 26.3 °C and 21.3 °C under static electrolyte conditions.
.....146

Figure 5.9: Anode current density along the limiting current region of polarization curves as a function of electrolyte temperature. Data was taken from polarization curves of Figure 5.8a.
.....147

Figure 5.10: Impedance diagrams determined for Nb in HF (49%): H₂SO₄ (96%) = 1: 9 (volume ratio) at different applied potential as indicated.
.....148

Figure 5.11: High frequency Nyquist impedance diagrams determined for Nb in HF (49%): H₂SO₄ (96%) = 1: 9 (volume ratio) at static vs. flow condition. The flow rate was estimated to be 4~ 5 cm/sec.

.....149

Figure 5.12: Polarization resistance (R_p) obtained from the high frequency impedance response as a function of different potential and flow rate for Nb in HF (49%): H_2SO_4 (96%) = 1: 9 (volume ratio) at 9.0 ± 0.2 °C.

.....150

Figure 5.13: Effective double layer capacitance (C_{dl}) obtained from the high frequency loop as a function of applied potential and flow for Nb in HF (49%): H_2SO_4 (96%) = 1: 9 (volume ratio) at 9.0 ± 0.2 °C.

.....151

Figure 5.14: Schematic Nyquist plot (a, top) and equivalent circuit (b, bottom) corresponding to the high-frequency part of the impedance diagram.

.....152

**SURFACE STUDY OF NIOBIUM
FOR SUPERCONDUCTING RADIO
FREQUENCY (SRF) ACCELERATORS**

CHAPTER 1

Introduction

1.1. Motivation

Superconducting radio frequency (SRF) technology has become an important foundation for particle accelerators at the energy and luminosity frontier as well as at the cutting edge of nuclear physics, higher energy physics, basic material science and life science [1-3]. Superconducting radio frequency machines include: TRISTAN at High Energy Accelerator Research Organization (KEK) in Japan, the Large Electron Positron Collider (LEP) at Conseil Eutopéene pour la Recherche Nucleaire (CERN) in Switzerland and the Hadron-Elektron-Ringanlage (HERA) at Deutsches Elektronen-Synchrotron laboratory (DESY) in Germany. The Cornell Electron-positron Storage Ring (CESR) at Cornell University in US and the KEK-B electron positron collider in Japan stand at the energy frontier and luminosity frontier. At the cutting edge of nuclear and elementary particle science, the Continues Electron Beam Accelerator Facility (CEBAF) at the Jefferson Lab in US and LEP-II have been two

of the largest SRF installations. The Spallation Neutron Source (SNS) at the Oak Ridge National Laboratory (ORNL) in US, the X-ray Free Electron Laser (XFEL) under construction at DESY and the storage ring light sources, such as CESR, Taiwan Light Source, Canadian Light Source are known work well for basic material science and life science. The most important project in the field of high energy physics, after the Large Hadron Collider (LHC) at CERN, is the International Linear Collider (ILC). It is planned to stretch approximately 35 kilometers in length and use 16,000 superconducting cavities operating at 31 MV/m to accelerate electrons and positrons. The beams of this facility will collide 14,000 times every second at extremely high energies 0.5 TeV center-of-mass with luminosity greater than $10^{34} \text{ cm}^{-2}\text{s}^{-1}$ [3-4].

Since the first use of SRF cavities of Stanford University in 1974 [3], the performance of niobium SRF cavities has improved significantly over the past few decades. The acceleration gradient has increased from 5-10 MV/m typical of early 1990's to 25~ 40 MV/m [3] and even pushed performance toward the theoretical limit of 50 MV/m [4]. The quality factor, Q_0 values at this gradient now approach 10^{10} . New applications of niobium SRF cavities for high energy and high luminosity electron-positron colliders – (such as ILC), proton-proton colliders, storage ring light sources are forthcoming. Free electron lasers, linac-based light sources, energy recovering linacs (ERL), muon storage rings for neutrino sources and eventually high energy muon collider are also imminent [3].

Compared to normal conducting copper cavities, superconducting niobium cavities, like those installed at CEBAF at Jefferson Lab, routinely have about five

orders of magnitude lower energy losses. Even when taking account of the cost of refrigeration at cryogenic temperature, their efficiency in converting ac power into beam power is about five times higher than that of normal conducting cavities [5]. In addition to the capability for operating SRF cavities at higher acceleration gradient due to the reduced power demand, the large aperture of superconducting cavities minimizes disruptive interactions with the beam, making them more suitable for use in high current accelerators [6].

Superconducting cavities are commonly operated in the transverse magnetic TM_{010} mode* (The transverse magnetic modes are classified as TM_{mnp} , where the integers m , n and p count the number of sign changes of E_z in the ϕ , ρ and z direction. Only TM_{0np} ($n = 1, 2, 3, \dots$, $p = 0, 1, 2, \dots$) modes have a non vanishing longitudinal electric field on axis and the TM_{010} is used for acceleration in most cavities [7]) and their performance is characterized by the dependence of the quality factor, Q_0 on the acceleration field E_{acc} or on the surface fields (electric or magnetic) as shown in Figure 1.1[8]. The quality factor, $Q_0 = \omega U / P$ is defined as the ratio between the cavity stored energy (U) and the power dissipated in the one RF radian (P/ω).

A schematic illustration of electric field and magnetic field distribution in a typical SRF cavity in the TM_{010} mode is shown in Figure 1.2. The electric field is greatest at the irises and near the symmetry axis, while the magnetic field is concentrated in the equator region [9]. To maximize the potential cavity performance, it is important to

minimize the ratios of E_{pk} / E_{acc} and H_{pk} / E_{acc} , where E_{pk} is the peak electric surface field that occurs at the iris, H_{pk} is the peak magnetic surface field which occurs near the equator, E_{acc} is the acceleration gradient, defined as

$$E_{acc} = \frac{V}{d} = \frac{1}{d} \int_0^d E(z) e^{i\omega_0 z/c} dz \quad 1-1$$

where V is the accelerating voltage, d is the cell gap length.

Theoretically, the acceleration gradient limitation for bulk niobium would be approximately 50 MV/m [10], corresponding to a peak electric surface field, E_{pk} can sustain 100 MV/m [10] for a typical cell shape. However, this gradient has been limited by various anomalous loss mechanisms in practice[10]; (1) Thermal breakdown or “quench” (a transition of the cavity to the normal conducting state), which can be triggered by local surface defects, field emission, multipacting or the Bardeen-Cooper-Schrieffer (BCS) surface resistance[11-13]. (2) Enhanced field emission, characterized by the tunneling of electron under high surface electric field from a spot (“emitter”) on the cavity surface, accompanied by bremsstrahlung x-rays and heating. (3) Multipacting which is the resonant impact of electrons in an RF cavity, where an electron emitted from the cavity surface is accelerated by RF field and eventually impacts a cavity wall again, producing secondary electrons.

Niobium is the material most widely used for construction of superconducting radio frequency cavities because it has the highest critical transition temperature ($T_c = 9.25 \text{ K}$) of the pure metals, sufficiently high thermodynamic critical field

($B_c \sim 200\text{mT}$) for SRF applications and metallurgical properties adequate for fabrication and service load [10, 13]. Niobium metal superconductivity is a nanoscale, near-surface phenomenon because of the shallow RF penetration; e.g., 36 nm at 1.5 GHz [10]. Considerable published evidence indicates that cavity interior surface chemistry and topography strongly impacts SRF accelerator performance. *Undesirable surface effects including: magnetic field enhancement at a sharp transition, such as a grain boundary edge, the creation of anomalous "hot spots," and electron multipacting [6, 10, 11-17]. These limiting effects create sufficient motivation to investigate how they are affected by post-fabrication treatments.*

In the preparation of niobium SRF cavities, surface damage and contamination are intended to be removed by chemical etching, followed by post-etch treatments. The two widely practiced etch technologies are buffered chemical polishing (BCP) and electropolishing (EP) [10]. Typically, in a BCP solution, the 1:1:1 or 1:1:2 (volume) mixture of HNO₃ (69%), HF (49%) and H₃PO₄ (85%), flows end-to-end through the cavity at approximately 10°C for a time sufficient to remove the mechanically-damaged and contaminated layer. The cavity shapes used for accelerator applications result in considerably different local surface flow rates because of a non-uniform interior surface of the cavity [18]. Electropolishing is believed to be a superior technique to treat niobium cavity surfaces for achieving high performance SRF cavities [19] and is selected to replace BCP for the highest gradient applications. For EP, a mixture of hydrofluoric (49%) and sulfuric acid (95 ~98 %) in a volume ratio of 1 : 9 is typically used with a temperature range of 30 °C ~ 40 ° C, a

current density of 30 ~ 100 mA/cm², and an applied voltage of 10~20 volts. However, large variation of cavity performance has resulted from the presently applied empirical EP processes [20-21]. It becomes a major limitation for pursuing reproducible high gradient cavities for next-generation particle accelerators. Microscopic understanding of the basic Nb EP mechanism is expected to provide an appropriate foundation to optimize the preparation of high-field niobium cavity surfaces.

The surface morphology of niobium after etching has not been systematically characterized, with the result that it is unknown at what scale roughness is important to SRF performance. The roughness of niobium surface has been measured for a range of sizes and resolutions, and can only be accomplished using several different diagnostic instruments. A method of combining the measurements from the different diagnostic tools is therefore needed in order to obtain a comprehensive picture [22].

Niobium has a large negative free energy and is dominated by high reactivity toward oxygen [23-24]. The outermost oxide layers (~ 2-6 nm) are always found to be Nb₂O₅. Suboxides such as NbO₂, NbO, and Nb₂O are proposed to be between the Nb₂O₅ and the underlying metal[25-32]. In order to understand how chemical composition varies with depth under different treatments, a damage free surface characterization method, dominantly x-ray photoelectron spectroscopy (XPS) has been used. To obtain the near-surface (depth) information, it is necessary to minimize ion damage from sputter profiling [28, 32] which may alter the stoichiometry or

apparent thickness of niobium oxide layer as a result of preferential removal of oxygen and/or “knock-on” effect [28, 33].

Over the last few decades, a steady improvement in the polishing techniques and cleaning procedures has enabled production of Nb SRF cavities made of bulk niobium which could sustain peak surface electric field E_{acc} beyond 30 mV/m without field emission. Today, a primary limit of niobium is mainly characterized by a new category of “anomalous” loss, which was first reported in 1997[34-35]. It is represented by a severe degradation of quality factor (Q -drop) at peak magnetic surface field above 90 mT . An empirical method that is effective in reducing the Q -drop is low temperature ($100\sim 140 \text{ }^\circ\text{C}$) *in situ* baking of the cavity within high vacuum [36-37]. It has now become an indispensable procedure for cavity production. A number of models have been proposed to explain the origin of Q -drop and baking effect [38-39], none of which is fully able to account for all the observations. Since the penetration depth of the RF current is only about 40 nm [38-39], a systematic study of the effect of baking on Nb samples surface in parallel to RF tests on cavities is very important and scientifically necessary.

1.2. Organization of the Dissertation

Chapter 2 presents systematic study of the surface topography of niobium under typical cavity production conditions. Stylus profilometry and atomic force microscopy (AFM) were used to view surface topography. For the first time, a power

density spectral (PSD) method has been explored to combine the topographic data taken from different instruments and at different length scales. The investigation of niobium surface topography under incremental BCP and EP is introduced. Chapter 3 explores non-destructive depth profiling of surface oxides by using for the first time variable photon energy spectroscopy with synchrotron radiation. This is presented as an alternative to angle resolved x-ray photoelectron spectroscopy (ARXPS). In particular, the influence of different baking conditions on the surface oxide under is reported. The effect of the most commonly employed treatment, buffered chemical polishing (BCP) on polycrystalline niobium sheet, over a range of realistic solution flow rates has been examined through multiple surface characterization techniques. The result is reported in chapter 4. In chapter 5, detailed study of the effect of the area ratio of the anode and cathode, electrolyte temperature and HF concentration for niobium EP processes by using for the first time improved electrochemical techniques are presented. The mechanism of Nb electropolishing in the hydrofluoric and sulfuric acid electrolyte has been identified by electrochemical impedance spectroscopy (EIS) studies and the results are reported.

1.3. References

1. C. M. Lyneis, M. McAshan, and N. T. Viet, "Proceedings of the 1972 Proton Linear Accelerator Conference", Sante Fe, NM (1972), pp. 98.
2. L. Palumbo, S. Tazzari, and V.G. Vaccaro, "Proceedings of the Capri Workshop on Linear Colliders", INFN Frascati (1989).
3. C. E. Reece, "Proceeding of the 3rd Workshop on RF Superconductivity", Argonne, IL (1999), pp. 545.
4. P. Bernard, G. Cavallari, E. Chiaveri, E. Haebel, H. Heinrichs, H. Lengeler, E. Picasso, and V. Picciarelli, "Proceeding of the 11th International Conference on High-Energy Accelerators", Geneva, Switzerland (1980), pp. 878.
5. J.R. Delayen, and K. W. Shepard, Appl. Phys. Lett. 57(1990), pp. 51.
6. <http://www.lns.cornell.edu/public/CESR/SRF/BasicSRF/SRFBas1.html>
7. J.Knobloch, Ph.D thesis, Cornell Univ., (1997)
8. H. Padamsee, J. Knobloch, and T. Hays, "*RF Superconductivity for Accelerators*", Wiley, New York (1998).
9. J. Bardeen, L.N. Cooper, and J.R. Schrieffer, Phys. Rev., 108 (1957), pp. 1175.
10. D.C. Mattis and J. Bardeen, Phys. Rev., 111, (1958), pp. 412.
11. R. Ballantini, and R. Parodi, "Proceeding of the 9th Workshop on RF Superconductivity", Sante Fe, NM (1999), pp.211.
12. P. Kneisel, "Proceeding of the 9th Workshop on RF Superconductivity", Sante Fe, NM (1999), pp. 328.
13. H. Padamsee, Supercond. Sci. Techol. 14 (2001), pp. 28.

14. R.L. Geng, J. Knobloch, and H. Padamsee, "Proceeding of the 9th Workshop on RF Superconductivity", Sante Fe, NM (1999), TUP 021.
15. J. Knobloch, R.L. Geng, M. Liepe, and H. Padamsee, "Proceeding of the 9th Workshop on RF Superconductivity", Sante Fe, NM (1999), TUP 004.
16. H. Tian, C. Reece, and M. Kelley. Appl. Surf. Sci., 253(3)2006, pp.1236.
17. F. Eozénou, A. Aspart, C. Antoine and B. Maliki. CARE Report 06-10-SRF, EU contract number RII3-CT-2003-506395 (2006).
18. International Linear Collider (ILC) Reference Design Report (2007), <http://www.linearcollider.org/cms>.
19. H. Tian, G. Ribeill, M. J. Kelley, and C. E. Reece, "Proceeding of the 13th Workshop on RF Superconductivity", Beijing, China (2007), <http://www.pku.edu.cn/academic/srf2007/proceeding.html>.
20. B. R. King, H. C. Patel, D. A. Culino, and B. J. Tatarchuk, Thin Solid Film, 192(1990), pp. 351.
21. B. R. King, and B. J. Tatarchuk, Thin Solid Film, 192(1990), pp. 371.
22. Q. Ma, and R.A. Rosenberg, Appl. Surf. Sci., 206(1-4) (2003), pp. 209.
23. Q. Ma, and R.A. Rosenberg, "Proceedings of the 2001 Particle Accelerator Conference", Piscataway, NJ, 2 (2001), pp.1050.
24. A. Dacca, G. Gemme, L. Mattera, and R. Parodi, Appl. Surf. Sci., 126(3-4) (1998), pp. 219.
25. J. Halbritter, Surf. Interf. Anal., 12(1-12) (1988), pp.354.
26. J. Halbritter, Appl. Phys. A- Solids & Surfaces. A 43(1) (1987), pp. 1.

27. J. Halbritter, Solid State Communications. 34(8) (1980), pp. 675.
28. M. Grundner, and J. Halbritter, J. Appl. Phys. 51(1) (1980), pp. 397.
29. A. Darlinski, and J. Halbritter, J. Vac. Sci. Technolog. A, 5(4) (1987), pp.1235.
30. A. Dacca, G. Gemme, L. Mattera , and R. Parodi, Surf. Sci. Spec., 5(4) (1998), pp. 332.
31. H. Hahn, and H. J. Halama, I. Appl. Phys., 47(1976), pp. 4629.
32. P. Kneisel, K. Saito, R. Parodi, "Proceeding of the 8th Workshop on RF Superconductivity", Abano Terme, Italy (1997), pp. 463.
33. E. Kako, "Proceeding of the 8th Workshop on RF Superconductivity", Abano Terme, Italy (1997), pp. 491.
34. P. Kneisel, "Proceeding of the 9th Workshop on RF Superconductivity", Santa Fe NM (1999), pp. 328.
35. B. Visentin, J. P. Charrier, and B. Coadou , "Proceeding of the 9th Workshop on RF Superconductivity", Santa Fe NM (1999), pp. 1885.
36. G. Ciovati, Physica C, 441, (2006), pp. 57
37. G. Ciovati, Ph.D thesis, Old Dominion Univ., (2005)
38. H. Padamsee, Superconductor Science & Technology, 14(4) (2001), pp. 28.
39. H. Padamsee, J. Knobloch, and T. Hays, "*RF Superconductivity for Accelerators*", Wiley, New York (1998).

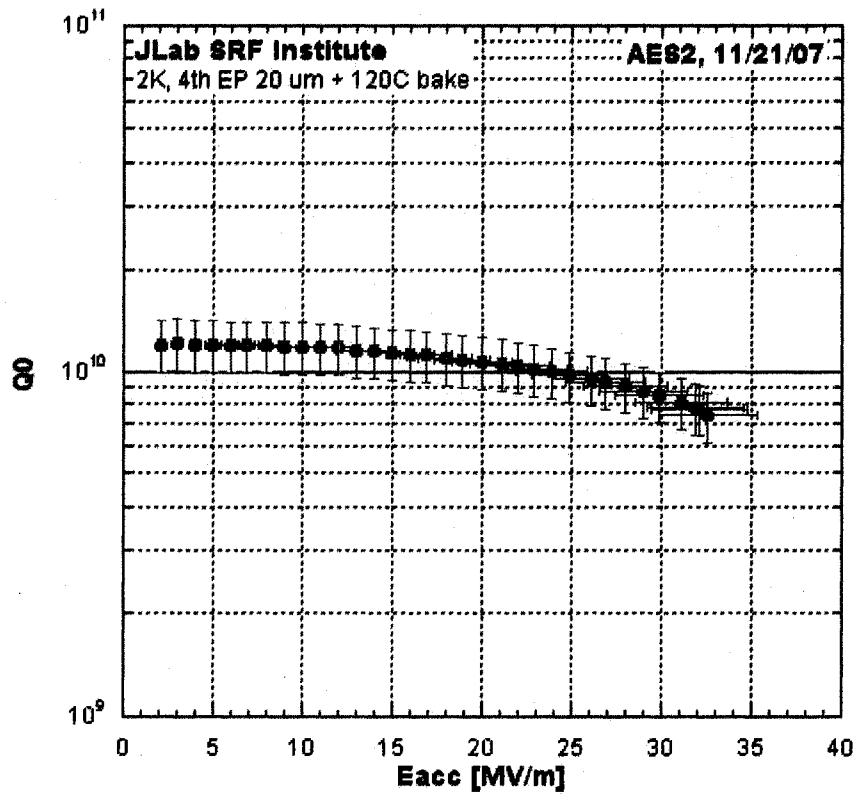


Figure 1-1: Q vs. E_{acc} for an electropolished niobium 9-cell cavity. The acceleration gradient reaches $32 \text{ MV} / \text{m}$. Courtesy of Jefferson lab.

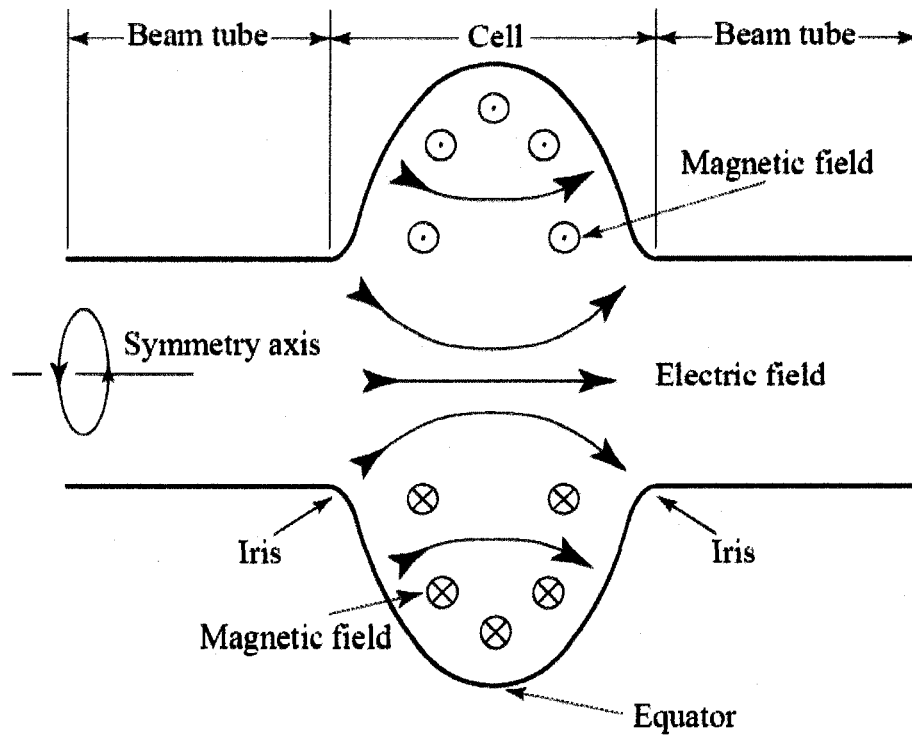


Figure 1-2: A schematic illustration of electric and magnetic field distributions in a typical single-cell SRF cavity for a typical SRF accelerating cavity cell (From <http://www.lns.cornell.edu/public/CESR/SRF>, reprinted with permission of Cornell University).

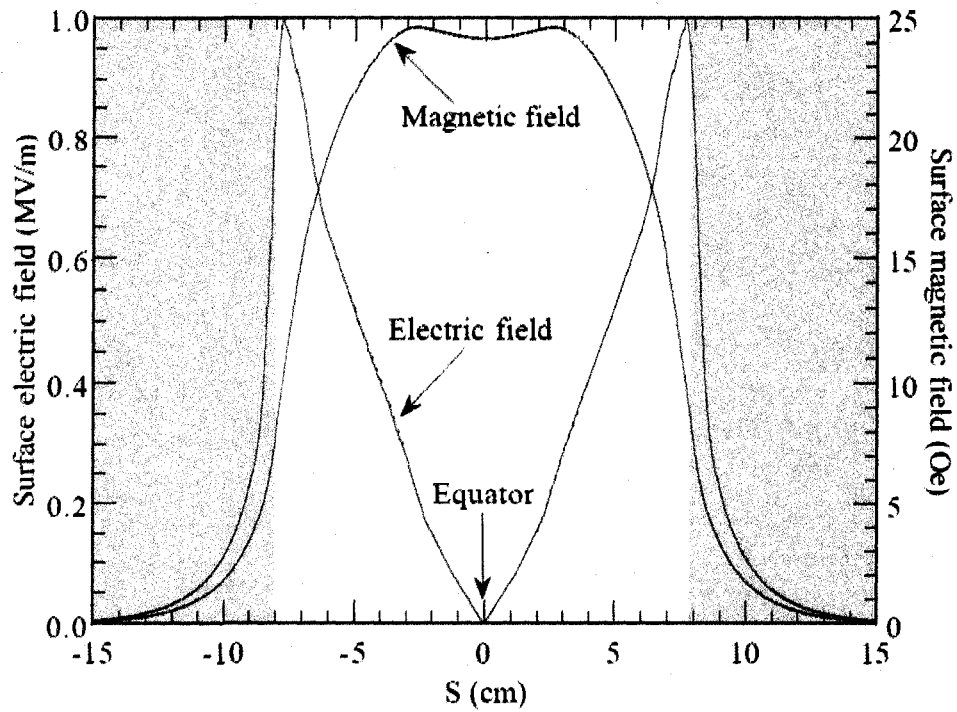


Figure 1-3: Surface electric field and magnetic field as a function of distance from equator ($E_{pk} = 1 \text{ MV/m}$) (From J. Knobloch, PhD thesis, 1997. Reprinted with permission of Cornell University)

CHAPTER 2

Surface Topography Studies of Niobium

2.1. Introduction

Surface roughness has proven to be a critical factor in determining the efficiency and maximum accelerating gradient that SRF cavities can achieve [1]. Experimental results on cavity radio frequency (RF) tests indicate that the onset field of the Q -drop is increased in cavities with the smoother surfaces [2]. Further low temperature bake-outs seem to be more effective in reducing the Q -drop on smoother surface, such as EP polycrystalline cavities, or in cavities with large grains [3]. Temperature mapping of Q -slope-afflicted polycrystalline niobium cavities etched with buffered chemical polishing (BCP) reveals that the breakdown frequently occurs in the equator area, where the magnetic field is highest in the TM_{010} mode, causing an increase in the surface resistance [11]. The losses do not appear to be uniformly distributed along the cavity equator, but there are a number of “hot-spots” which increase with increasing RF field. One of models to explain the Q -drop, proposed by J. Knobloch et. al [4], explained the breakdown caused by magnetic field enhancement at sharp edges, such

as grain boundaries and electron-beam-weld (EBW) regions [5], where the magnetic field locally exceeds the RF critical field (H_c) [4-5]. However, this mechanism has been recently brought into question by results of RF tests of BCP treated single crystal niobium cavities [6-10] having a much smoother surface ($R_q < 0.1 \mu m$ [9]). The measurements show that severe degradation of quality factor (Q_0) at high field is still present and significant reduction of Q -drop is achieved by baking cavities *in situ* at 120°C [6-7, 9-10]. In addition to Q -drop, electron multipacting has been shown to be directly affected by the quality of the niobium surfaces resulting from different chemical treatment [12].

It is unknown at what scale roughness is important to SRF performance. Therefore the roughness of niobium surfaces has been characterized with different diagnostic instruments in order to provide systematic characterization. When different types of measurements are made on the same sample area, they are converted to a common quantity, such as root mean square (RMS) roughness, for comparison. The results are generally different because of the spatial-frequency bandwidth limits [13]. A method of combining the measurements from different diagnostic instruments is therefore needed. Studies have shown that the power spectral density (PSD) based description of surfaces is less dependent on instrumental effects when one measures parameters such as surface roughness and correlation length [14]. From PSD, one can directly obtain the characteristic length of surface features as well as the fractal dimension of the surface [13].

Prior to electropolishing of niobium SRF cavity, various methods have been used to remove the surface damage layer. Examples include 20 μm removal by BCP for TESLA Test Facility (TTF) cavities [15], 45 μm removal by EP for the X-ray free-electron laser (XFEL) in Europe and international linear collider (ILC) cavities [15], and 80 μm removal by BCP only for Jefferson lab [16] or followed by 25~200 μm removal by centrifugal barrel polishing (CBP) for High Energy Accelerator Research Organization (KEK) cavities [16, 17]. However, understanding the effect of the starting surface condition before electropolishing has not been investigated. As a result, a study of surface variation with different treatments would be very helpful in the overall improvement surface finishing and the practical processing costs [18].

In this chapter, a set of polycrystalline and single crystal niobium samples were subjected to buffered chemical polishing and electropolishing under conditions for SRF cavity production. The systematic surface topography characterization was conducted through stylus profilometry and atomic force microscopy (AFM). In order to combine data to these diagnostic instruments, the power spectral density (PSD) analysis technique was explored. The variation of the surface topography and PSD as a function of applied etching and polishing steps are discussed.

2.2. Experimental Studies

2.2.1. Sample Preparations

Niobium single crystal disk samples of 12 mm diameter were saw cut from 3.175 mm thick Nb large-grain sheet used for fabricating large grain cavities—the technology recently developed at Jefferson Lab [19]. The same diameter polycrystalline Nb disk samples with 3 mm thickness were cut from the high-RRR-grade fine grain Nb sheet stock used to make standard SRF cavities, having purity of 99.9999% according to the manufacture-Wah Chang. After ultrasonic degreasing for 20 minutes, one set of samples (BCP) was treated in a fresh 1:1:2 BCP solution - mixture of HNO₃ (69%), HF (49%) and H₃PO₄ (85%) by volume for 100 minutes at room temperature, removing a weight equivalent to about 200 μm of material, a second set of samples (EP) was etched with a fresh 1:9 mixture of HF (49%) and H₂SO₄ (96%) with a 40~45 mA/cm² operational current density at temperature about 35°C and same amount of removal achieved. To remove acid residue and particles from samples introduced during handing, the samples were ultrasonically rinsed in deionized water immediately following BCP/EP for 20 minutes. After rinsing, the samples were air dried and material removal was confirmed by weight loss.

A third set of samples for the study of surface topographic variation under different steps of BCP and EP treatment was polycrystalline Nb slabs with dimensions of 22mm x 22 mm x 4 mm. All were mechanically ground using 1 μm Al₂O₃ grit prior to any chemical treatment, as is done in cavity production. The as-ground samples used as a reference for an “untreated” state were etched in a fresh BCP (1:1:2) bath at room temperature for 5 minutes to remove any residual surface contamination from previous mechanical work. In this study, “Light BCP” refers to

the samples which were etched in a fresh BCP (1:1:2) bath at room temperature for 20 minutes. As measured by weight loss, 30 μm removal was achieved. Those samples referred to as "Heavy BCP" were placed in a fresh BCP (1:1:2) at room temperature for 90 minutes which resulted in a 150 μm removal. Samples having undergone "no" BCP (untreated) treatment, as well as those having undergone light and heavy BCP treatment were subjected to an incremental 30 minutes of EP at 6V relative to a saturated mercury-mercurous reference electrode (MSE) with electrolyte temperatures of 33 ~34°C.

2.2.2. Surface Topography Measurements

2.2.2.1. Stylus Profilometry

The stylus profilometry is a surface profiling system capable of measuring small surface variations in vertical stylus displacement as a function of position. A stylus is moved vertically to contact with a sample and then moved laterally across the sample for a specified distance and contact force. The height information measured by the probe is transformed into a digital signal by an electrical sensor resulting in 2D (profile line) or 3D (area measurement) surface height data. The typical radius of the diamond stylus is 5~25 μm , but, a very sharp stylus (~0.1 μm) is available [20]. The lateral resolution of the instrument depends mainly on the radius of the stylus. The sampling interval and measurement line length or measurement area also affects the lateral resolution [20-21]. The vertical resolution depends on the mechanical noise and the type of the transducer which detects the movements of the probe [21]. The stylus profilometry is not sensitive to surface reflectance or color. Also, contacting

the surface is often an advantage in dirty environments where non-contact methods can end up measuring surface contaminants instead of the surface itself. However, it is not well suited for soft surfaces such as semiconductor materials or coated and precision optics, since a heavy preload on the stylus will scratch the surface and a light preload may not be sufficient to register all the surface features [21]. The maximum lateral resolution (i.e. smallest surface spatial frequency) depends on the sharpness of the stylus tip. In addition, the mechanical scanning over the surface is a slow measurement technique compared to non-contact optical profilometry [20].

Stylus profilometry measurements were obtained by using a KLA-Tencor: P-15 with a 2 μm radius stylus. The samples were scanned in three different regions with a scan size of 200 μm \times 200 μm and 1000 μm \times 1000 μm . Each 200 μm \times 200 μm scan was taken as an array of 101 traces with 401 points in each trace, and each 1000 μm \times 1000 μm scan was taken as an array of 251 traces with 2501 points.

2.2 2. 2. Atomic Force Microscopy (AFM)

Atomic Force Microscopy is a widely used technique for investigating surface topography at the nanometer scale. It is one of the families of scanning probe microscopies that were generated by the invention of the scanning-tunneling microscope. The pioneering research was done by Young et al. in 1972[22], and the first modern instrument was built by Binnig, Rohrer and co-workers in 1981[23-24]. The AFM was proposed by Binnig et al. in 1986[25] and rapidly developed into several commercial instruments. The basic principle for this technique is the measurement of different forces between a sharp tip and a specimen surface. When a

probe tip is raster scanning the specimen surface, the interaction force is measured by the deflection of a soft cantilever and used for imaging. It is the short range of the repulsive force that enables high resolution imaging of surfaces. The advantage of the AFM includes ambient condition operation, easy sample preparation, direct depth information availability, atomic resolution over a large area ($100\mu\text{m}\times 100\mu\text{m}$), and the capability of *in-situ* measurement in liquid or air.

The AFM instruments usually comprise: a sharp tip mounted on a soft cantilever, a detection system for measuring the deflection of the cantilever, a piezoelectric translator to move the probe, a feedback system to keep the deflection constant and an imaging system to convert the signal into image. There are two different modes for AFM operation. In contacting mode, the tip is physically in contact with the sample surface; while in tapping mode, the cantilever with the tip is driven close to its resonance frequency and the topographic information is obtained from the amplitude signal of the oscillating cantilever. Since there is only intermittent contact with the sample surface, one can avoid scratching the sample surface or removing loosely bounded features. Detailed information about the principle and operation of AFM can be found in references [26-27].

The AFM used for this work was a Digital Instrument Dimension Nanoscope IV operated in the Tapping Mode with an ultrasharp silicon tip of a diameter of 10 nm. The instrument peak-to-valley height range was approximately $6.344\ \mu\text{m}$, the rms noise in the vertical dimension was $< 0.05\ \text{nm}$, and the lateral accuracy was typically 1%. The image drift between successive scans of the same area was small and could

be neglected. The samples were scanned in five different regions with scan sizes of $20 \mu\text{m} \times 20 \mu\text{m}$, $30 \mu\text{m} \times 30 \mu\text{m}$, $40 \mu\text{m} \times 40 \mu\text{m}$, $50 \mu\text{m} \times 50 \mu\text{m}$, and $100 \mu\text{m} \times 100 \mu\text{m}$. The AFM images were captured as arrays of height values with 256×256 points and 512×512 points.

2.2.3. Power spectral density (PSD)

Power spectral density (PSD) has been used as a tool to combine measurements from different scales associated with different diagnostic instruments [28-29]. It represents the spatial-frequency spectrum of surface roughness measured in inverse-length units. The one-dimensional (1-D) PSD is the square of the Fourier transform of a linear surface profile, whereas the two-dimensional (2-D) is the so-called surface factor of ARS function and can be calculated through the following equation[30-31].

$$PSD(f_x, f_y) = \lim_{L \rightarrow \infty} \frac{1}{L^2} \left| \int_{-L/2}^{L/2} \int_{-L/2}^{L/2} h(x, y) e^{-2\pi i(f_x x + f_y y)} dx dy \right|^2 \quad 2-1$$

where the surface topography data are $h(x, y)$ and the PSD variable f_x and f_y are the spatial frequencies of the surface roughness and are related to the lateral dimensions of the surface features. From equation 2-1, we know that the PSD gives information about the relative contributions of all the possible surface spatial frequencies for an ideal measurement of an infinite surface in the limiting case from 0 frequency (an infinite surface) to an infinite frequency (infinitely small structure) [13]. Or, in the case of discrete data consisting of N points separated by Δx , it can be computed as in equation 2-2.

$$PSD(f_x)_N(m) = \left| \left(\frac{\Delta x}{N} \right) \sum_{n=0}^{N-1} h(x)_n \exp(-i2\pi nm / N) \right|^2 K(m) \quad 2-2$$

where $-N/2 \leq m \leq N/2 - 1$, equation 2-2 gives an expression for the m th term in the PSD calculated from a profile of N points. There are non discrete values of $f_x = m/L$, where L is the measurement length and x in the function $h(x)_n$ takes on discrete values: $x = (L/N)_n$. Also, Δx is the spacing between data points in the profile, $h(x)_n$ are the height values of the profile data points, and $K(m)$ is a book-keeping factor that equals 1 except that $K(\pm N/2) = 1/2$ at the ends of the power spectrum. A more complete mathematical description can be found in ref [13-14, 28, 32-33]. The PSD not only represents the squared amplitude of surface features plotted against the spatial frequency of those features, but also provides information about both the lateral and vertical size of features. The range of spatial frequencies over which the PSD is valid for a certain scan size is determined by the Nyquist limits- $\left[\frac{1}{2N\Delta x}, \frac{1}{2\Delta x} \right]$ [13, 35-36]. In this study, the power spectral densities for all traces in the fast scan direction were averaged to approximate the true 2D PSD. This assumption is valid in the case of a surface with isotropic roughness [13]. In order to eliminate the measurement errors and increase the goodness of statistic representation of the whole surface, the PSD profiles measured at different locations under the same scan condition were averaged together; the PSD profiles from the profilometry data

were filtered using a 4-sample moving average in order to eliminate spurious high-frequency noise [34].

2.3. Results and Discussion

2.3.1. Surface Topography of BCP/EP Single Crystal and Polycrystalline Niobium

Figure 2.1 presents the optical images of the single crystal and polycrystalline niobium surface after BCP/EP polishing treatments with 200 μm removal, which were taken with HIROX KH-3000VD high resolution digital video microscopy system. Important features to notice are: compared with EP-treated polycrystalline niobium, the BCP-treated polycrystalline niobium surface grain boundaries and other features are heavily etched and evolved into micro-steps with sharp edges. Surfaces of BCP treated single crystal samples appear more undulating than that of an EP single crystal, Our results show that EP treated single crystal Nb samples give the best finish, however across a 40 μm \times 40 μm scanning area, 100 nm scale roughness remained as shown in Figure 2.2.

The typical measurement of surface roughness is expressed as the root mean square (RMS) roughness, defined by equation (1).

$$R_q = RMS = \sqrt{\frac{1}{n} \sum_{i,j} (z_{i,j} - \bar{z})^2} \quad 2-3$$

measuring surface roughness for 30 BCP-treated polycrystalline samples gave an average RMS value of $1.6 \pm 0.42 \mu\text{m}$ (standard deviation) in a 50 μm \times 50 μm scan

area by AFM. The electropolishing results in smoother surfaces than BCP. Under the same measurement conditions, the average RMS value of 30 EP treated polycrystalline niobium is $0.34 \pm 0.11 \mu\text{m}$. Comparing single crystal material with the polycrystalline material after BCP, the RMS roughness is reduced from $1.6 \mu\text{m}$ to $0.3 \mu\text{m}$. In the same scan area, the EP single crystal surface gave less $0.1 \mu\text{m}$ RMS values.

2.3.2. Surface Topography with Incremental BCP/EP Treatment

RMS roughness is a useful and widely employed measurement for Nb surface roughness. However, it is dependent on the scan size and the particularities of the area being scanned. Figure 2.3 shows a plot of different RMS values computed from the data at all of the scan sizes after different polishing (BCP/EP). The RMS values varied dramatically with different scanning areas which were done through different instruments. It is, therefore, difficult to compare roughness values taken using different instruments, especially considering that the range of spatial frequencies which any instrument can resolve is necessarily limited and unique [13-14, 28]. Furthermore, this roughness measurement considers only vertical information; it does not give any information about the lateral morphology of surface features.

To overcome these limitations, power spectral density (PSD) has been used as a tool to combine measurements from different scales and different instruments [13, 28]. Figure 2.4 shows the combined AFM and profilometry data from the sample with 5 minutes of BCP treatment at different scanning areas (profilometry : $200 \mu\text{m} \times 200 \mu\text{m}$ and $1000 \mu\text{m} \times 1000 \mu\text{m}$; AFM : $20 \mu\text{m} \times 20 \mu\text{m}$, $50 \mu\text{m} \times 50 \mu\text{m}$, and $100 \mu\text{m} \times$

100 μm). The spatial frequency ranges corresponding to the different measurements largely overlap and the PSD functions using the two techniques agree very closely over the range of frequencies that are common to both instruments. This shows that the PSD method can combine surface profile information from different instruments in a consistent and useful manner. At the high-frequency end of the spectra, the slope of all the graphs show a remarkable decrease and begins to level off. This is likely an effect of limited resolution for the AFM and the finite tip size for the profilometry [34]. Of particular interest in this figure is the change of slope that occurs at a spatial frequency approximates $0.04 \mu\text{m}^{-1}$. Changes in slope of the PSD are related to the inverse of the correlation length of the sample. The correlation length sets the scale at which surface features are similar [30, 35]. For this data, the correlation length is approximately $25 \mu\text{m}$, which is on the order of the size of niobium grains in the polycrystalline material studied.

A topography and PSD comparison of the ground samples after receiving different polishing (“untreated”, light BCP, heavy BCP and 30 minutes EP) can be found in Figure 2.5 and Figure 2.6. The AFM images were measured at $50 \mu\text{m} \times 50 \mu\text{m}$ scan area with 6000 nm data scale in vertical direction for “untreated”, light BCP and heavy BCP samples, $100 \mu\text{m} \times 100 \mu\text{m}$ scan area with 3000 nm data scale in vertical direction for 30 minutes EP sample. The power spectra were calculated from the $1000 \mu\text{m} \times 1000 \mu\text{m}$ profilometry scans and the $20 \mu\text{m} \times 20 \mu\text{m}$ AFM scans. From those figures, one observes that the light BCP helps smooth out the sharp edges caused by mechanical grinding and they are totally removed after 90 minutes BCP

~150 μm . Interestingly, the light BCP treatment seems to produce a smaller PSD amplitude at low frequencies than that of heavy BCP treatment, but the situation is reversed at high frequencies-which could be caused by the residual mechanical damaged layer. This effect would be impossible to analyze using only RMS as a measure of surface roughness; it indicates that a longer BCP treatment produces a better micropolish, but a rougher macropolish. It may be due to the differential etching by BCP for grains with different crystallographic orientations. As more material is etched, even though the damage caused by the mechanical polish is removed, material from different grains is removed at different rates, leaving a rougher surface. The smaller amplitude of the PSD for the ground sample, with 30 minutes EP shows that electropolishing produces the smoothest surface, also consistent with the results of RMS measurement (see Figure 2.2). For an electropolished sample, the slope change at $0.04 \mu\text{m}^{-1}$ is no longer visible, indicating that differences between grains have been greatly reduced as indicated from Figure 2.5d. Furthermore, the greater slope of the PSD from the middle to high frequency region as compared to the other polishing techniques further indicates that EP provides the best polish in the micro-range [37]. The PSD profile of the electropolished sample also shows a change in slope at the smallest frequency, corresponding to a surface with the longest correlation length. However, those differences of surface topography caused by different pre-treatment were largely reduced by a longer EP. The “untreated” sample-without any removal of damage layer by BCP, achieves almost same polishing as comparing with different duration

BCP-treated samples (light BCP, $\sim 30 \mu\text{m}$ removal; heavy BCP, $\sim 150 \mu\text{m}$ removal) as shown in Figure 2.7a, b and c.

Figures 2.8a and 2.8b present the power spectra of a ground sample calculated from the $1000 \mu\text{m} \times 1000 \mu\text{m}$ profilometry and $100 \mu\text{m} \times 100 \mu\text{m}$ AFM scans after an incremental series of electropolishing treatments. The amplitude of the PSD is observed to decrease dramatically after 30 minutes EP and continually to decrease less rapidly thereafter. It indicates that the surface protrusions caused by mechanical grinding were quickly leveled out by a short period of EP, the edges of grain boundaries and recessed parts of the surface are continually smoothed with duration of electropolishing. Furthermore, the overlap of the plots in the high-frequency region indicates that there is no significant difference in the quality of the electropolishing at the small scales. The increased correlation length of the ground sample subjected to longer EP suggests that the rougher surface at large scale has gradually been smoothed out. However, more EP might be needed for surface brightening, as indicated from topography measurements (see Figure 2-9 and 2-10).

Topography data from the ground sample EP treated at two different electrolyte temperatures was also examined by using the power spectral density method. As shown in Figure 2.11, the spectra calculated from the $1000 \mu\text{m} \times 1000 \mu\text{m}$ profilometry scans and the $20 \mu\text{m} \times 20 \mu\text{m}$ AFM scans have a different shape at the low frequency region, even though it well overlaps at the high-frequency region. The longer correlation length of the sample electropolished with 24°C electrolyte suggests that the lower temperature may help maintain the stable polishing condition and

produce a uniform surface finishing, considering the strong dependence of current density for electrolyte temperature during EP [37-38]. Such a conclusion is also supported by the RMS roughness values: 84 *nm* for the 24°C niobium sample and 94 *nm* for the 30°C sample at a scan size of 20 μm x 20 μm . This is consistent with the observation that the etching rate increases with local temperature, which might be due to increasing diffusion of F ion [37]. However, further systematical study of surface topography resulting from different electrolyte temperature with electrochemical study is needed.

2.4. Conclusion

The first use power spectral density in quantitatively characterizing the surface topography of niobium has been demonstrated. PSD measurements allow for the combination of data taken from different instruments and at different length scales. They also allow for a detailed analysis of the surface properties of niobium in both the vertical and lateral dimensions, information otherwise inaccessible to classical methods of quantifying roughness. The power spectral density provides the most information about the surface from the most sources and so should be the preferred diagnostic when analyzing surface roughness. This tool will therefore allow for improved characterization and analysis in the production of SRF cavities. The PSD of BCP and EP treated surfaces have been directly compared. The niobium surface topographic differences after different treatments were noted to be the scale-dependent. The variation in niobium surface after different duration BCP and EP

shows that longer BCP leaves a rougher surface at a few microns-scales, which might be due to differential etching from different grains. The following electropolishing (~90 mins) almost levels the surface variations caused by different pre-treatments. Our data also suggests that a lower temperature electrolyte promotes a smoother surface at larger scales. The most important future work, however, will be to determine at what length scales roughness is most important to cavity performance. Such information will allow for the development of a polishing process that optimizes the performance of SRF cavities and thereby accelerator systems.

2.5. References

1. H. Padamsee, J. Knobloch, and T. Hays, "*RF Superconductivity for Accelerators*", Wiley, New York (1998).
2. G. Ciovati, *Physica C*, 441, (2006), pp. 57
3. M. Ono, Proceedings of the 8th Workshop on RF Supercond., KEK, Japan (1998), pp. 472.
4. J. Knobloch, R. L. Geng, M. Liepe, and H. Padamsee, "Proceeding of the 9th Workshop on RF Superconductivity", Sante Fe, NM (1999), TUP 004.
5. R. L. Geng, J. Knobloch, and H. Padamsee, "Proceeding of the 9th Workshop on RF Superconductivity", Sante Fe, NM (1999), TUP 021.
6. G. Ciovati, *J. Appl. Phys.* 96 (2004), pp. 1591.
7. B. Visentin, Y. Gasser, and J. P. Charrier, *Physica C*, 441 (2006), pp. 66
8. G. Ciovati, *Appl. Phys. Lett.*, 89(2006), pp. 22507
9. G. Ciovati, P. Kneisel, and A. Gurevich, *PhysRevSTAB*, 10 (062002) (2007), pp.1.
10. G. Ciovati, Ph.D thesis, Old Dominion Univ., (2005)
11. G. Ciovati, P. Kneisel, J. Sekutowicz, and W. Singer, "Proceeding of the 2005 Particle Accelerator Conference", Knoxville, TN(2005), TPPT072
12. H. Padamsee, *Supercond. Sci. Technol.* 14 (2001), pp. 28.
13. A. Duparré, J. Ferre-Borrull, S. Gilech, G. Notni, J. Steinert, and J. Bennett *Appl. Optics.* 41(1) (2002), pp.154.

14. C. Walsh, A. J. Leistner, and B. F. Oreb, *Appl. Optics*. 38(22) (1999), pp. 4790.
15. A. Matheisen, B.v.d. Horst, B. Peterson, S. Sägebarth, and P. Schilling, "Proceeding of the 12th Workshop on RF Superconductivity", Ithaca, NY(2005), TUP 08.
16. K. Saito, H. Inoue, E. Kako, and T. Fujino, "Proceeding of the 8th Workshop on RF Superconductivity", Newport News, VA (1997), pp. 795.
17. K. Saito, "Proceeding of the 8th Workshop on RF Superconductivity", Beijing, China(2007), TU202, <http://www.pku.edu.cn/academic/srf2007/proceeding.html>.
18. "ILC Reference Design Report", (2007), <http://www.linearcollider.org/cms/>.
19. P. Kneisel, Proceeding of the 2005 Particle Accelerator Conference, Knoxville, TN (2005), TPPT08.
20. C.Y. Poo, and B. Bhushan, *Wear* 190(1) (1995), pp. 76
21. H. Zahouani, R. Vargiolu, P. H. Kapsa, J. L Loubet, and T.G. Mathia , *Wear* 219(1) (1998), pp. 214.
22. R. Young, J. Ward, and F. Scire, *Rev. Sci. Instrum.*, 43(1972), pp. 999.
23. G. Binnig, and H. Rohrer, *Helv. Phys. Acta.*, 55(1982), pp. 726.
24. G. Binnig, C. F. Quate , Ch. Gerber, and E. Weibel, *Phys. Rev. Lett.*, 49(1982), pp. 57.
25. G. Binnig, C. F. Quate, and Ch. Gerber, *Phys. Rev. Lett.*, 56(1986), pp. 930.
26. D. Sarid, "*Scanning Force Microscopy with Application to Eclectic, Magnetic and Atomic Forces*", Oxford U. Press, New York (1991).

27. S. N. Magonov, and M. H. Whangbo, "*Surface Analysis with STM and SFM*", VCH, Weinheim, Germany (1995).
28. J. Ferré-Borrull, A. Duparré, and E. Quesnel, *Appl. Optics.* 40(13) (2001), pp. 2190.
29. O. Vatel, *Jpn. J. Appl. Phys.* Vol. 23(1993), pp. 5671.
30. J. M. Elson, J. M. Bennett, *Appl. Optics.* 34(1) (1995), pp. 201.
31. E. L. Church, *Appl. Optics.* 27 (1988), pp. 1518.
32. "Optics and Optical Instruments-indication in optical drawing", in Draft International Standard ISO 10110 Part 8: Surface Texture, ISO/TC 173/SC 1/WG2 (Inter-national Organisation for Standardisation, Geneva, Switzerland)
33. J. M. Bennett, "Surface Roughness Measuremen- in Optical Measurement Techniques and Applications", Chap 12, pp. 341.
34. F. Biscarini, *Phys. Rev. Lett.* 78(12) (1997), pp. 2389.
35. K. Westra, D. Thomson, *J. Vac. Sci. Technol. B.* 13(2) (1995), pp.344.
36. H. Tian, C. Reece, and M. Kelley. *Appl. Surf. Sci.*, 253(3),2006, pp.1236
37. H. Tian, M. J. Kelley, S. C. Cocoran, and C. E. Reece, "Proc. of 13th SRF workshop", Beijing, China (2007), WE104,
<http://www.pku.edu.cn/academic/srf2007/proceeding.html>.
38. F. Eozénou, A. Aspart, C. Antoine, and B. Maliki. CARE Report 06-10-SRF. EU contract number RII3-CT-2003-506395. (2006).

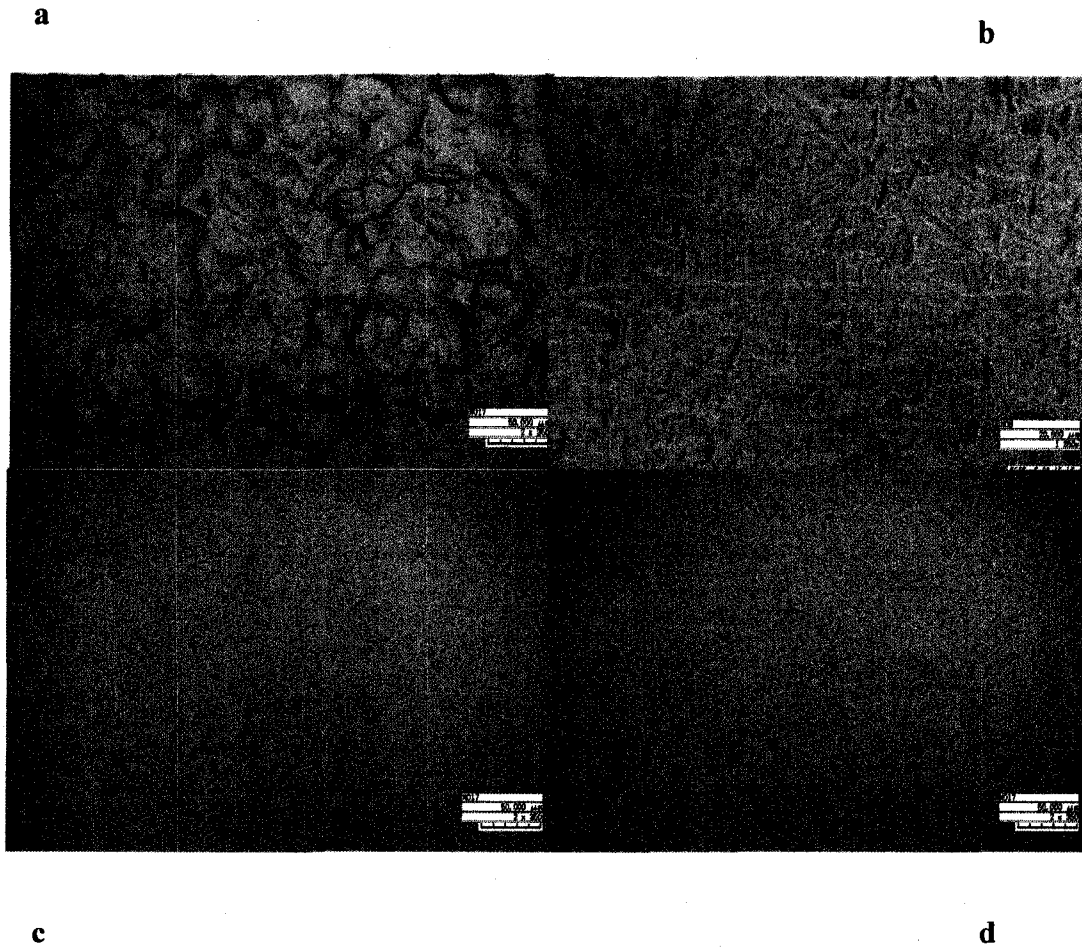


Figure 2.1: Optical images of the polycrystal niobium surface after a) BCP and c) EP etch, and single crystal niobium surface after b) BCP and d) EP etch. (Bar in the lower right of Figures 2.1b represents 20 μm ; bar in the lower right of Figures 2.1a, c and d represents 50 μm).

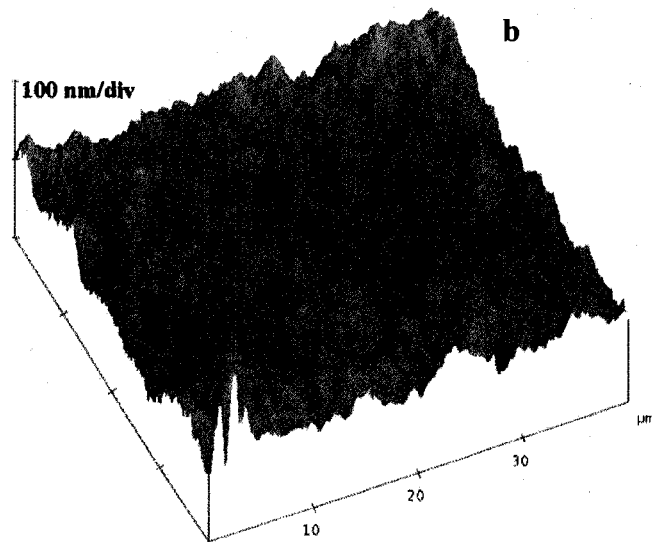
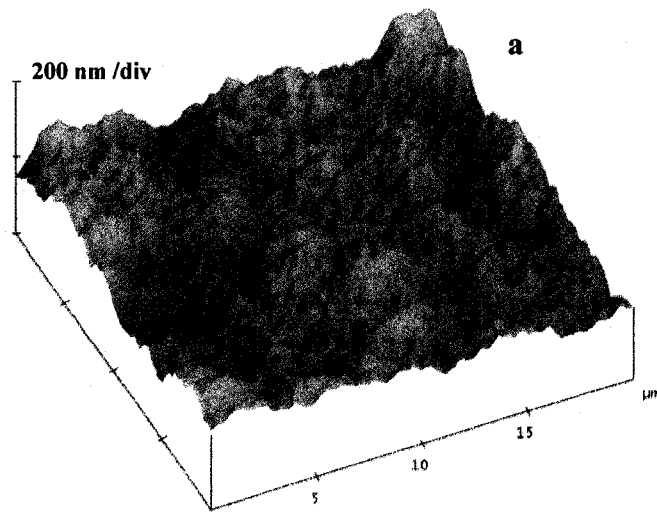


Figure 2.2: AFM images of a) BCP treated single crystal niobium ($20 \mu\text{m} \times 20 \mu\text{m}$), and b) EP treated single crystal niobium ($40 \mu\text{m} \times 40 \mu\text{m}$)

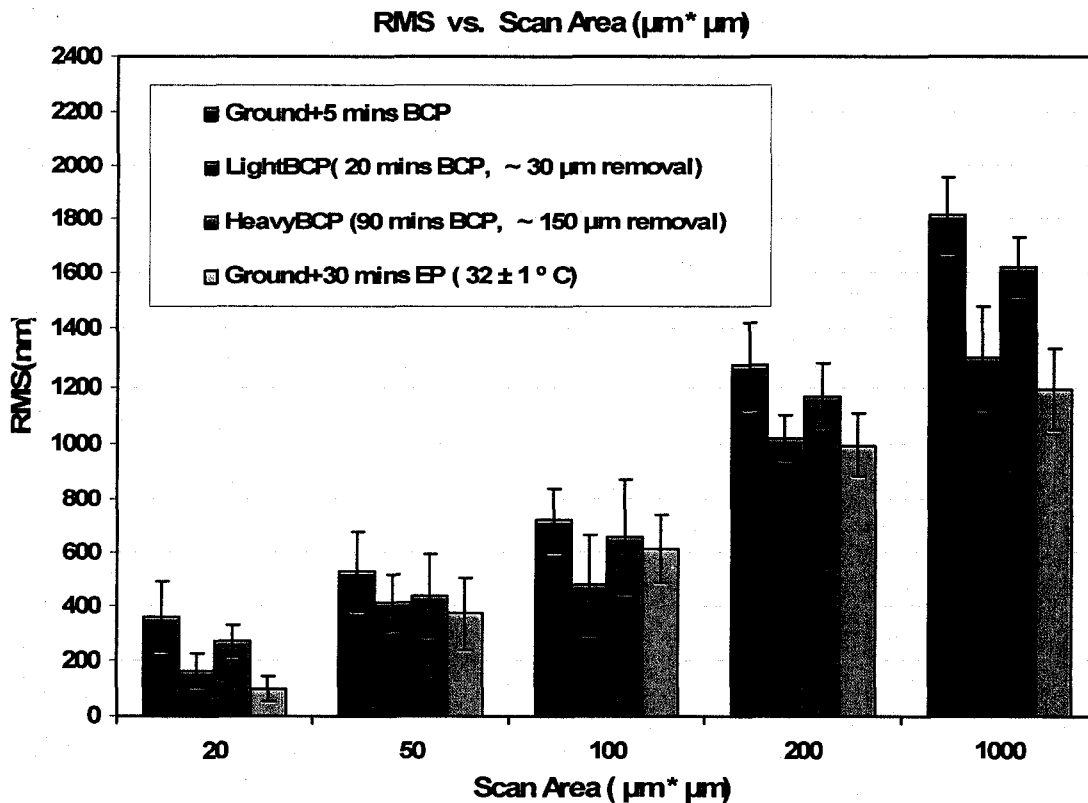


Figure 2.3: RMS roughness values computed from AFM and profilometer data taken at different scan lengths ($20 \mu\text{m} \times 20 \mu\text{m}$, $50 \mu\text{m} \times 50 \mu\text{m}$, and $100 \mu\text{m} \times 100 \mu\text{m}$ by AFM; $200 \mu\text{m} \times 200 \mu\text{m}$ and $1000 \mu\text{m} \times 1000 \mu\text{m}$ by stylus profilometry) for different treatments (blue: ground + 5 mins BCP; dark purple: light BCP; green: heavy BCP; light purple: ground + 30 mins EP).

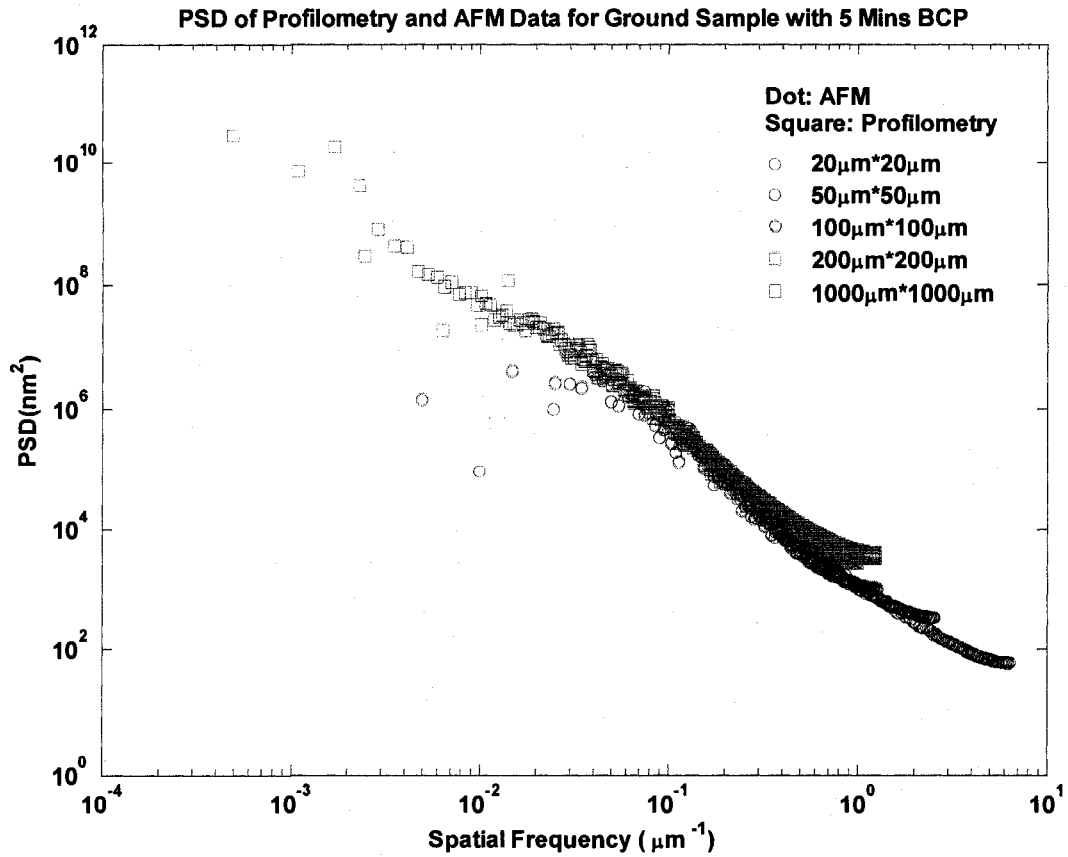


Figure 2.4: Combined AFM and profilometer power spectral densities from all scan sizes (red: 20 $\mu\text{m} \times 20 \mu\text{m}$; magenta :50 $\mu\text{m} \times 50 \mu\text{m}$; green: 100 $\mu\text{m} \times 100 \mu\text{m}$ - by AFM; light blue: 200 $\mu\text{m} \times 200 \mu\text{m}$; blue: 1000 $\mu\text{m} \times 1000 \mu\text{m}$ -by stylus profilometry) from the sample having undergone 5 minutes of BCP treatment.

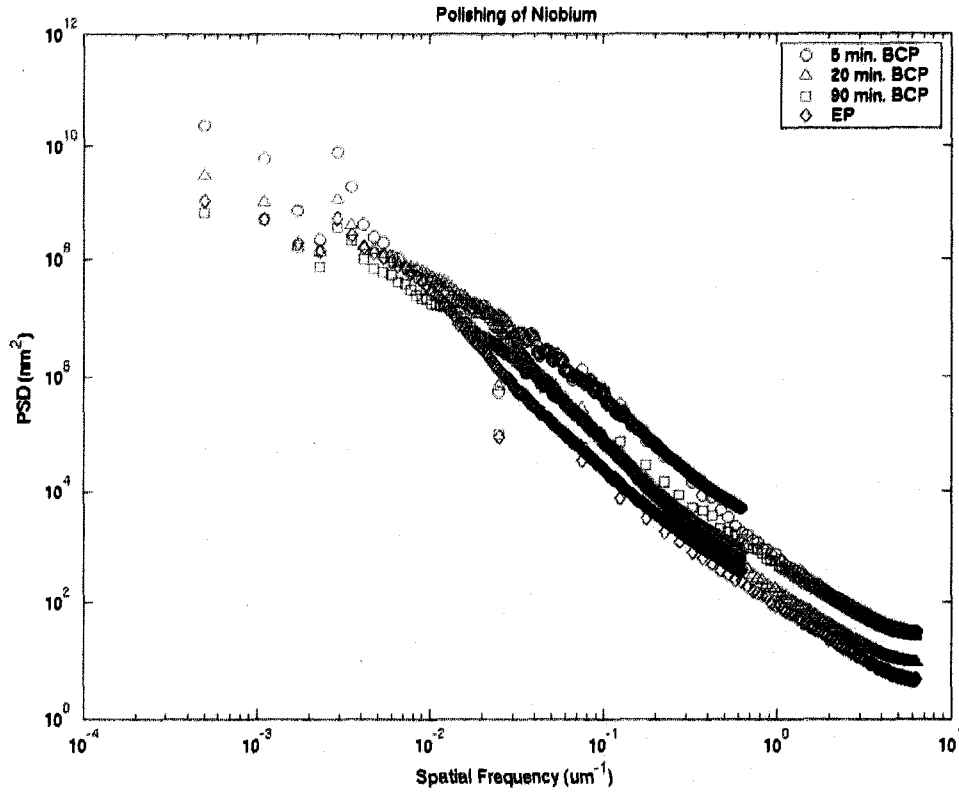


Figure 2.5: PSD spectra from scan sizes ($20 \mu\text{m} \times 20 \mu\text{m}$ by AFM and $1000 \mu\text{m} \times 1000 \mu\text{m}$ by stylus profilometry) for the different polishing methods (blue: 5mins BCP; red: light BCP; green: heavy BCP; black: 30 mins EP performed on a mechanically ground sample. (Adapt from H. Tian, M. J. Kelley, S. C. Cocoran, and C. E. Reece, "Proc. of 13th SRF workshop", Beijing, China, 2007, WE104, <http://www.pku.edu.cn/academic/srf2007/proceeding.html>).

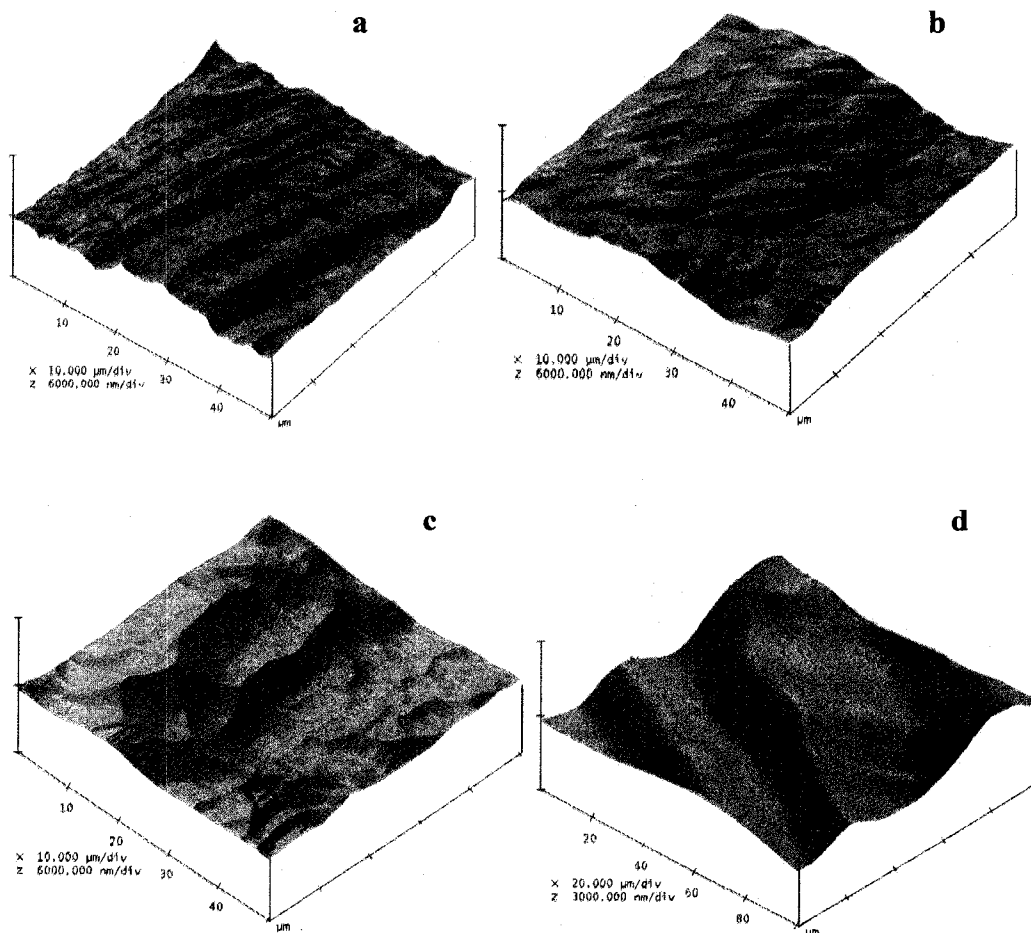


Figure 2.6: The corresponding AFM images for Figure 2.5 were measured at $50 \mu\text{m} \times 50 \mu\text{m}$ scan area with 6000 nm data scale in vertical direction for “untreated” (a), light BCP (b) and heavy BCP samples (c), $100 \mu\text{m} \times 1000 \mu\text{m}$ scan area with 3000 nm data scale in vertical direction for 30 minutes EP sample (d).

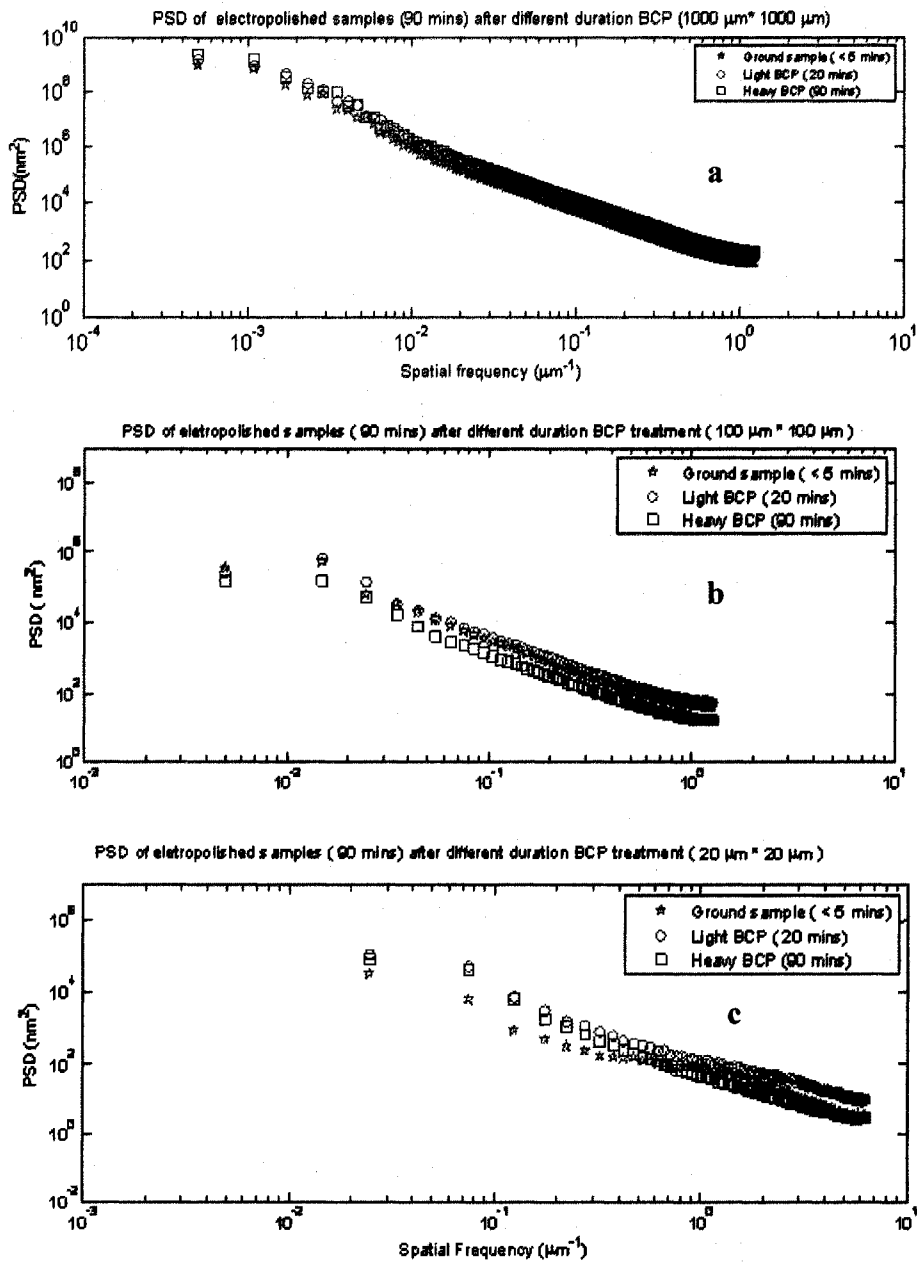


Figure 2.7: Power spectral density plots (a: 1000 $\mu\text{m} \times 1000 \mu\text{m}$ by stylus profilometry, b: 100 $\mu\text{m} \times 100 \mu\text{m}$ by AFM, c: 20 $\mu\text{m} \times 20 \mu\text{m}$ by AFM) of 90 mins electropolished samples that have undergone different duration BCP etch (green: ground sample; red: light BCP; blue: heavy BCP)

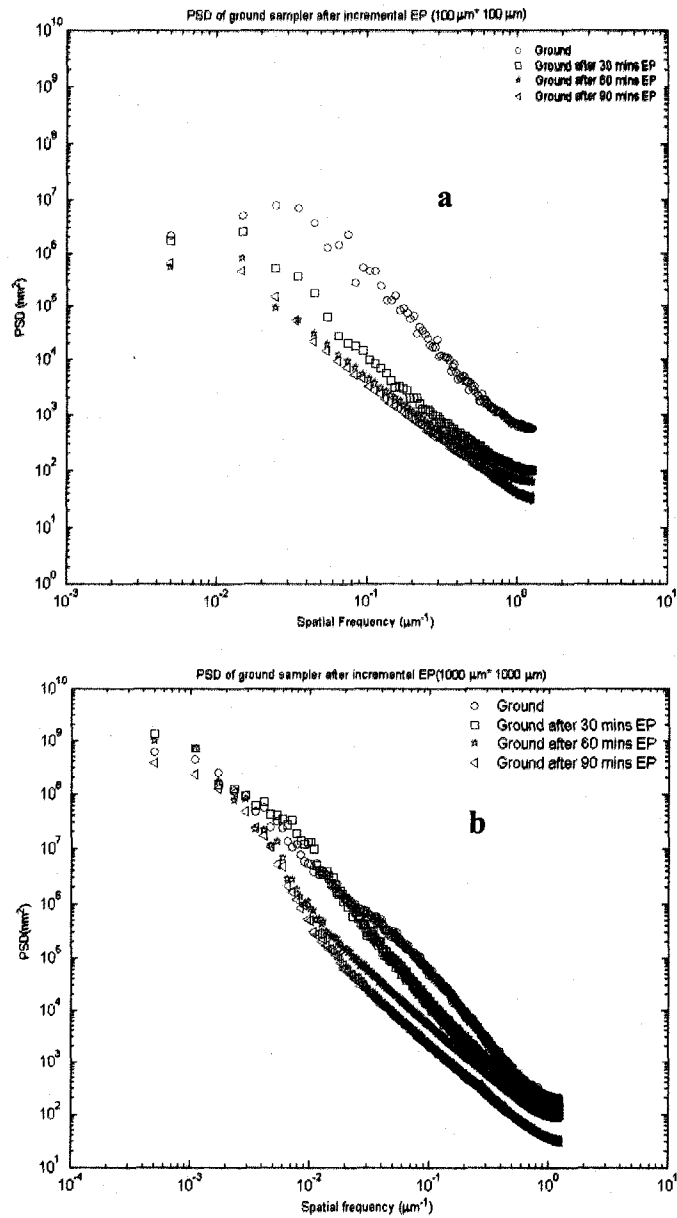


Figure 2.8: Power spectral density plots (a: $100 \mu\text{m} \times 100 \mu\text{m}$ by AFM; $1000 \mu\text{m} \times 1000 \mu\text{m}$ by stylus profilometry) for incremental electropolished ground niobium sample (red: ground sample; purple: 30 mins EP; green: 60 mins EP; magenta: 90 mins EP)

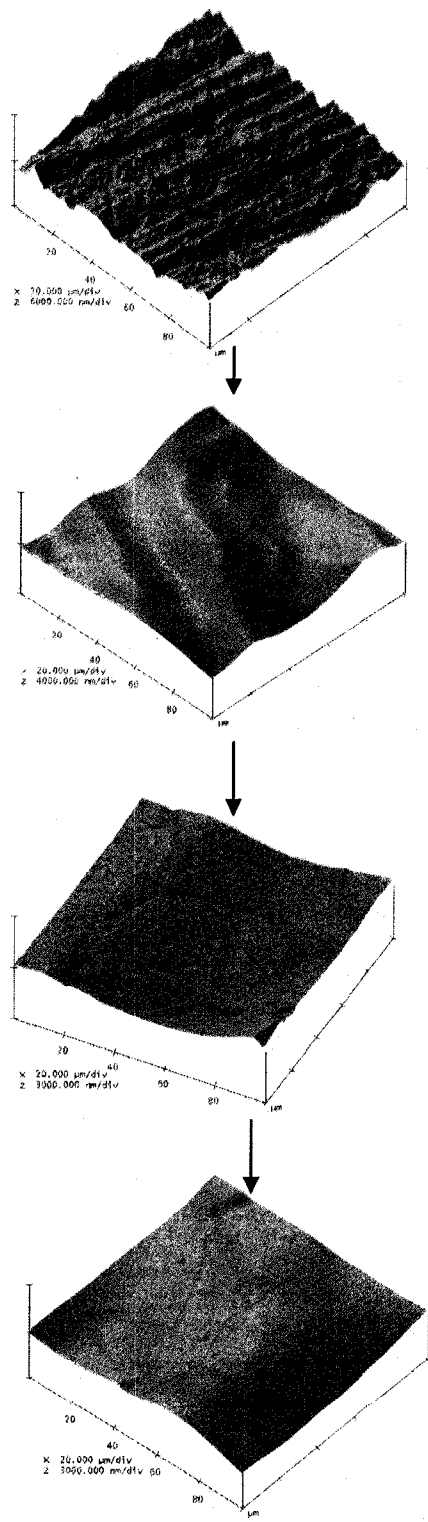


Figure 2.9: The corresponding AFM images ($100 \mu\text{m} \times 100 \mu\text{m}$) for Figure 2.8.

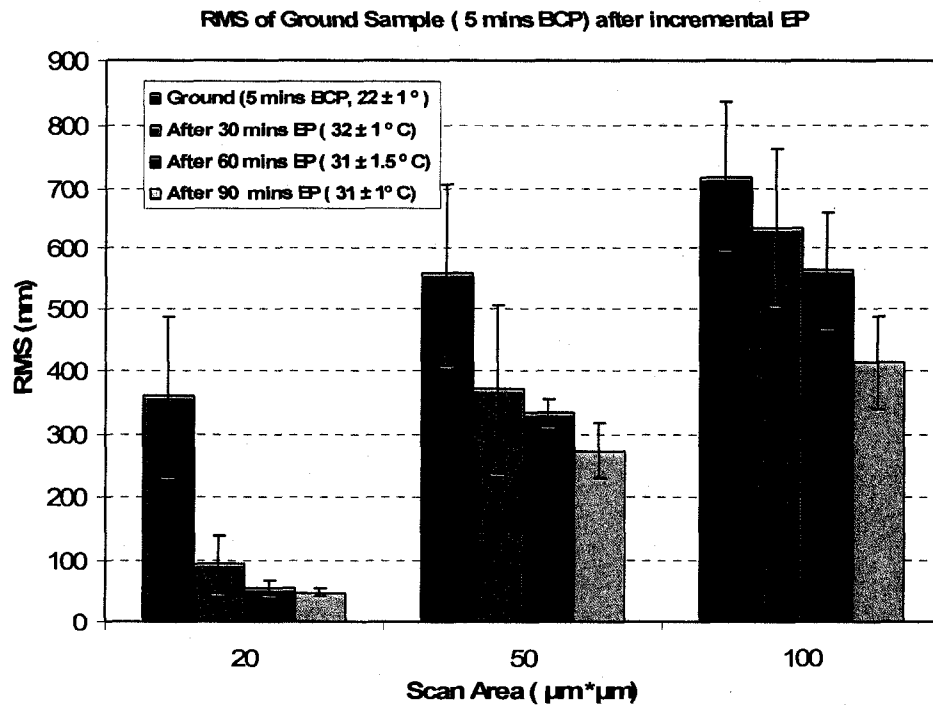


Figure 2.10: RMS roughness values computed from AFM data taken at different scan lengths ($20 \mu\text{m} \times 20 \mu\text{m}$, $50 \mu\text{m} \times 50 \mu\text{m}$, and $100 \mu\text{m} \times 100 \mu\text{m}$) for ground sample after different step EP etch.

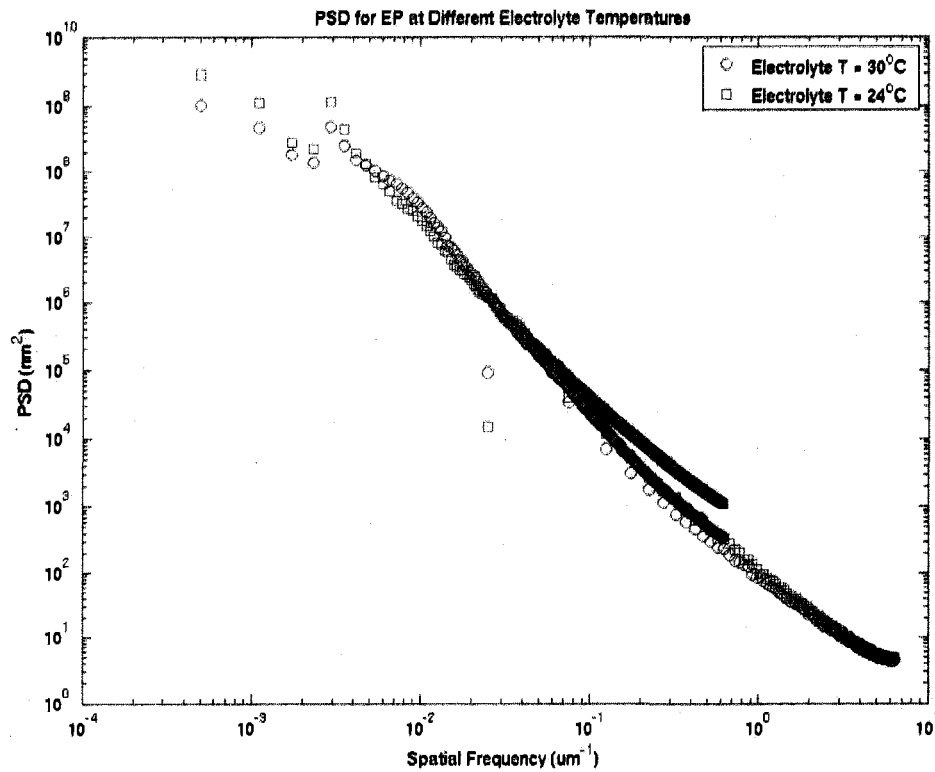


Figure 2.11: Power spectral density plots (dot : $100 \mu\text{m} \times 100 \mu\text{m}$ by AFM; square: $1000 \mu\text{m} \times 1000 \mu\text{m}$ by stylus profilometry) for ground sample after different temperature (red: $T=24^\circ\text{C}$, blue: $T=30^\circ\text{C}$) EP etch , (Adapt from H. Tian, M. J. Kelley, S. C. Cocoran, and C. E. Reece, “Proc. of 13th SRF workshop”, Beijing, China ,2007, WE104, <http://www.pku.edu.cn/academic/srf2007/proceeding.html>.)

CHAPTER 3

XPS Studies of Niobium Surface Oxide

3.1. Introduction

The surface chemistry of niobium under the conditions of cavity production has been largely studied through x-ray photoelectron spectroscopy (XPS). All the works agree that the outer most oxide on the all niobium samples, irrespective of sample preparation, is Nb_2O_5 [1-20]. Between Nb_2O_5 and the underlying metal, sub-oxides (NbO_x where $0 < x < 5$) have been proposed as a product of a gradual transition of the structure for strain relief [1-2, 4, 8-13], however experimental evidence for an explicit layer structure or discrete phases is still lacking. As it is related to the influence on superconducting radio frequency (SRF) performance, generally oxygen in niobium metal decreases the critical temperature, increases the Ginzburg Landau parameter, κ [22], reduces the superconducting energy gap [23] and the electron mean free path, and weakens the surface superconductivity B_c , [24]. Among oxides present on the niobium surface, Nb_2O_5 is an insulator, but NbO is a metallic

compound with a strongly reduced critical temperature ($T_c = 1.6K$) [22, 25] and may seriously impair SRF performance at typical operating temperatures ($\sim 2 K$) by increasing surface residual loss. Furthermore, if the oxides have a morphology of spikes down into the bulk [5, 7-10], residual losses would also arise from the resulting “weak link” in the niobium[26]. The reported binding energies of various oxidation states of niobium are summarized in Table 3.1[1-5, 11-13, 28-32].

Researchers seeking to understand how surface composition varies with depth turned to angle-resolved x-ray photoelectrons spectroscopy (ARXPS) [1, 4, 8, 11, 33-39]. For fixed attenuation length (AL) (called inelastic mean free path in most early work), the cosine dependence reduces the sampling depth. Further, ARXPS is a damage-free method to analyze variation with depth, in contrast to unavoidable damage with sputter depth profiling [11, 19]. In these studies, the oxidized *Nb* surface was identified as a sequence of stoichiometries corresponding to different depths and distributions by measuring the photoelectron spectra at different take-off angles, but large discrepancies about the thickness of Nb_2O_5 and suboxides were found, perhaps due to the oxides serrated into the metal surface on an nm scale [1-3, 5, 18] or surface roughness [33, 35-36].

Conventional XPS analyses employ characteristic sources such as *Al K α* (1486.6 eV) or *Mg K α* (1253.6 eV), but the consequent large information depth (~ 9 nm for Al anode, ~ 8.1 nm for Mg anode in Nb_2O_5) restricts the surface sensitivity in the analyses of the photoelectrons with low binding energy [40]. Variable photon

energy spectroscopy with synchrotron radiation not only eliminates this restriction, but also enables non-destructive XPS depth profiling by changing the photoelectron attenuation length. Compared with ARXPS, the variable photon energy spectroscopy always views the same column of material without regard to local topography, in contrast to the effect of tilting the sample for ARXPS, which inherently views different columns. While the difference is real, the impact is certainly insignificant for perfectly flat surfaces with planar structure, but may not be so for the topography resulting from BCP etching polycrystalline niobium with micro-scale roughness. Further, the error in calculated thickness of uniform overlayer on rough substrate strongly depends on the analyzing angle [33, 36-37].

The technology of cavity production and processing continues to mature [25, 41]. Problems encountered during RF cavity development, such as electron multipacting and field emission, have largely been solved and accelerating gradients as high as 40 MV/m are now achievable [42]. However, the high field “ Q -drop” significantly limits the achievement of cavity ultimate performance. In spite of lacking full understanding of the origin of “ Q -drop”, low temperature *in-situ* baking under high vacuum for 24~48 hrs, typically at $110\sim 140^\circ \text{ C}$, has been successfully applied for reducing high field “ Q -drop” over the last few years [43-47]. The improvement persists even after the cavity is exposed to air again. Consequently, low temperature bake has now become a final preparation step of Nb SRF cavities in several laboratories. Cavity studies show that baking niobium cavities for 48 hrs at temperature higher than 100° C decreases the BCS surface resistance and increase the

cavity quality factor [48]. But, the quench field decreases as the baking temperature is increased [87] and higher baking temperature (>180 °C) severely degrades cavity performance. It might be due to that the annealing at higher temperature results in a surface oxide layer consisting primarily of metallic suboxide [1, 4, 17] and high concentration of interstitial oxygen at the niobium/oxide interface [49], which may reduce the surface superconductivity (B_{c1}) and therefore yields enhanced *rf* losses [46-47, 49]. Non *in-situ* baking studies also show that baking a post-purified polycrystal niobium cavity in the air at atmospheric pressure at 110 °C for 60 hrs [45] or at 165 °C for 3 hrs yields a comparable benefit [45]. Recent studies of low T *in-situ* baking (120°C for 3 hrs) conducted on a large-grain single cell cavity was sufficient to reduce most of the hot spots up to a quench field [46].

A number of models have been proposed to explain the high field “*Q*-drop” and the baking effect [47]. Among them, J. Halbritter proposed the high field “*Q*-drop” as triggered by interface tunnel exchange (ITE) between conduction electrons in the niobium and localized states in the niobium pentoxide [50]. However, recent experimental results, including temperature maps, TE₀₁₁ test results, and high field cavity test results, all support that *Q*-drop is caused by high magnetic fields[47]. The magnetic field enhancement (MFE) model proposed by J. Knobloch assumes the *Q*-drop is caused by geometric magnetic field enhancement at sharp edges on the cavity surface [51]. However, high field losses are found still present in cavities with much smoother surfaces, such as single crystal cavities and electropolished cavities [46]. As indicated in chapter 2, exactly what constitutes “smooth” in this context has yet to be

resolved. Further, the beneficial effect of low temperature baking must be considered, since modification of surface topography cannot be foreseen [47]. High field “ Q -drop” has been observed on a cavity made of a single crystal, which indicates that the “ Q -drop” is not caused by weakly linked grain boundaries having normal conduction at high field strength [47]. Recently, G. Ciovati at the Jefferson lab suggests a oxygen diffusion model [49], similar to one proposed by Safa [52], where the on-set field of “ Q -drop” corresponds to the onset field for fluxoids penetrating the niobium surface. The field value of penetration is determined by the surface barrier, which is reduced by the presence of a high oxygen concentration near the metal /oxide interface and rough surface. By taking into account both assumed contribution from interstitial oxygen initially presented at the niobium–oxide interface($\sim 10\%$ [53]) and from oxygen gradient of the natural niobium pentoxide layer, the estimation of oxygen concentration profile at fixed baking duration (~ 48 hrs) has been done by solving the diffusion equation for oxygen as a function of temperature. The result shows that the oxygen concentration at the metal/oxide interface is reduced by baking at an optimal temperature range of $120^{\circ}\text{C}\sim 150^{\circ}\text{C}$, which seem to agree with the studies done for cavities [54-55]. However, to further validate this proposed model, it would be very useful to have a quantitative measurement of the surface oxide layer as a function of depth, before and after baking, and a systematic study of surface chemistry changes from the baking process conducted on SRF cavities.

3.2. Experimental Studies

3.2.1. Sample Preparations

Single crystal disk samples of 12 mm diameter were saw cut from 3.175 mm thick Nb large-grain niobium sheet used for cavity production. The RRR value was approximately 330 and the *Ta* content was less than 150 wppm, as specified by the manufacture-Comphahia Brasileira de Metalurgia e Mineração (CBMM) in Brazil. Electron backscatter diffraction (EBSD) indicates that crystalline orientation was (111). The BCP treated samples were etched in a fresh mixture of HNO₃ (69%), HF (49%) and H₃PO₄ (85%) 1:1:2 by volume, for 100 minutes at room temperature. Weight removal was equivalent to about 200 μm of material, an amount found to eliminate any trace of mechanical machining from the surface[56-57]. The EP treated samples were etched with a fresh mixture of HF (49%) and H₂SO₄ (96%) 1:9 by volume with a 35~50 mA/cm² operational current density at temperature around 35 °C for 500 minutes totally, resulting in the same amount of removal. Samples were ultrasonically rinsed in deionized water immediately following BCP/EP to remove chemical residues. After rinsing, the samples were air dried and material removal was confirmed by weight loss. The detailed surface topography of BCP/EP single crystal has been introduced in the previous chapter (see Figures 2. 2a and 2.2 b).

3.2.2. Surface Chemistry

3.2.2.1. X-ray Photoelectron Spectroscopy (XPS)

X-ray photoelectron spectroscopy (XPS), measures the energy distribution of electrons ejected from inner-shell orbital under x-ray irradiation. It was developed in the mid 1960s by K. Siegbahn and his research group [58]. K. Siegbahn was awarded

the Nobel Prize for physics in 1981 for his work in XPS [59-64]. The phenomenon is based on the photoelectric effect outlined by Einstein in 1905 where the concept of the photon was used to describe the ejection of electrons from a surface when photons impinge upon it [65].

The kinetic energy (E_{kin}) of a photoelectron is given by the photoelectric equation:

$$E_{kin} = h\nu - E_F^b - \phi_s \quad 3-1$$

where $h\nu$ represents the energy of the incoming photon, E_F^b is the binding energy with respect to the Fermi level and ϕ_s is the work function of the material[58, 66-67].

Since no two elements have the same set of electronic binding energy, measurement of emitted electron kinetic energies provides unique composition information for each element examined, therefore elemental identification of any material can be achieved.

In practice, all elements except hydrogen can be detected [67]. Figure 3.1 displays a wide range spectrum of a BCP treated single crystal niobium collected at 45° take off angle relative to the surface normal by using a monochromated Al anode, the chemical elements identified on the niobium surface were Nb, O and C (this work was done by using *PHI Quantera XPS*).

In addition, small differences are observed for the same element in different chemical environment in which an atom is found. Electrons ejected from the same element emerges with kinetic energy characteristic of the chemical state, manifesting

as a chemical shift in the XPS spectrum [58, 67]. Recording these changes provides a means of observing changes in the chemical environment of an atom.

3.2.2.2. Depth profiling–ARXPS and Variable Energy XPS

XPS is a surface sensitive technique, over 90% of the detected photoelectrons arise from the first few layers[67] because emitted electrons with a certain kinetic energy (E_{kin}) lose part of or all of their energy when they move through a solid material as a result of inelastic collisions. Hence, non-destructive depth profiling analysis is not only performed by changing take-off angle (θ) of the photoelectron (ARXPS) [68-70] but also by changing the inelastic mean free path (λ) through using an energy-variable excitation source from synchrotron radiation [71].

Basically, these two techniques are based upon a model that assumes the XPS signal is exponentially attenuated as it passes through a material [68, 72-75]. For a thin film layer with a certain thickness (d) on a substrate, the substrate signal (I_{sub}) attenuates as

$$I_{sub} = I_0 e^{-d/\lambda(E)\cos(\theta)} \quad 3-2$$

while the photoelectron intensity of the layer varies as

$$I = I^\infty [1 - e^{-d/\lambda(E)\cos(\theta)}] \quad 3-3$$

where $I = I^\infty$, when $d \gg \lambda(E)$, where $\lambda(E)$ is the inelastic mean free path (IMFP) as a function of electron energy [76].

In reality, it is more practical to measure I_{sub} and I , then calculate their ratio as

$$\frac{I}{I_{sub}} = \frac{I^\infty}{I_0} [e^{-d/\lambda(E)\cos(\theta)} - 1] \quad 3-4$$

For a double layer system (A/B/substrate), it is straight forward to deduce the following expression as

$$\frac{I_A}{I_{sub}} = \frac{I_A^\infty}{I_0} [e^{d_A/\lambda_A(E)\cos(\theta)} - 1] e^{d_B/\lambda_B(E)\cos(\theta)} \quad 3-5$$

and

$$\frac{I_B}{I_{sub}} = \frac{I_B^\infty}{I_0} (e^{d_B/\lambda_B(E)\cos(\theta)} - 1) \quad 3-6$$

In order to determine the film thickness, I^∞/I_0 does not have to be known practically if I/I_{sub} is normalized by that measured at $\theta = 0$. Through these equations, by choosing certain take-off angles or selecting different photon energies [68,72], the non-destructive layer by layer analysis of the chemical composition can be achieved through XPS. However, surface topography may present significant complications.

For many materials, the value of inelastic mean free path (IMFP), now termed attenuation length (AL), can be found in literature [28]. Alternatively it can be calculated using the TPP-2M equation of Tanuma et al [71-72] as,

$$\lambda = \frac{E}{\{E_p^2 [\beta_m \ln(\gamma E) - C/E + D/E^2]\}} \quad 3-7$$

where λ is the attenuation length (in \AA), E is the electron energy (in eV), and

E_p is free electron plasmon energy (in eV) and defined as

$$E_p = 28.8 / (N_v \rho / M)^{1/2} \quad 3-8$$

where ρ is the density (g/cm^3), N_v is the number of valence electrons per atom (for elements) or for molecules (for compounds) and M is the atomic or molecular mass number. β_m, γ, C, D are parameters and given as

$$\beta_m = -0.10 + 0.069\rho^{0.1} + 0.944 / [(E_p^2 + E_g^2)]^{1/2} \quad 3-9$$

$$\gamma = -0.191 / \rho \quad 3-10$$

$$C = 1.97 - 0.91\nu \quad 3-11$$

$$D = 53.4 - 20.8U \quad 3-12$$

where $U = E_p^2 / 829.4$, E_g is the band gap energy (in eV) for non-conductors. Table 3.2 lists the corresponding parameters of Nb_2O_5 used for the calculation.

3.2.2.3 Variable Photon Energy XPS with Synchrotron Radiation

Variable photon energy XPS was performed at the X1B undulator beamline at the National Synchrotron Light Source (NSLS), Brookhaven National Laboratory (BNL). Bending magnets, wigglers and undulators are three types of radiation source present in modern synchrotrons. The undulator is a periodic magnet array which leads to a nearly sinusoidal motion of an electron in its reference frame [80]. Interference between the radiation emitted at each point in the trajectory leads to an emission spectrum that is strongly peaked at a fundamental frequency, with lower intensity peaks at higher odd harmonic due to deviations from purely sinusoidal electron motion [80]. The photon energy at which the fundamental and harmonic peaks occur may be modified by adjusting either the strength of the magnetic field or the vertical

spacing between the alternating magnetic structures. The peak wavelengths λ_n , of the emitted radiation, are given by:

$$\lambda_n = \frac{\lambda_u}{2n\gamma^2} \left(1 + \frac{K^2}{2} + \gamma^2 \theta^2 \right) \quad 3-13$$

where λ_u is the undulator period length (in m), $n = 1, 3, 5, \dots$, θ is the angle relative to the forward direction, and $K = eB_0 \lambda_u / 2\pi m_e c = 93.4 \lambda_u B_0$, where B_0 is the peak magnetic field. Since the undulator effectively concentrates the output power into a small spectral range, it is a nearly ideal source for many spectroscopic techniques which require a very narrow bandwidth (high resolution) photon beam [80].

A schematic diagram of the arrangement of the components used at the X1B beamline is shown in Figure 3.2. The X1 undulator (U) provides a high brightness soft x-ray beam in the energy range of 100 ~ 1600 eV. The beam is focused onto the monochromator entrance slit (S1) by a pair of spherical mirrors (M1, M2). The light is diffracted by one of several interchangeable spherical gratings (G) and the photon energy of interest is selected by the exit slit (S2). The diverging monochromatic beam is focused onto the sample by another pair of spherical mirrors (M3, M4). The ejected photoelectrons are detected by a hemispherical analyzer with up to 0.1eV overall energy resolution.

The beam spot size of X1B is $100 \mu\text{m} \times 30 \mu\text{m}$ and the illuminated area remains constant as photon energy is changed. In order to keep constant energy resolution, the entrance and exit slits must be adjusted for different energies. The entrance and exit

slits were set at $100\ \mu\text{m} \times 100\ \mu\text{m}$ for $300\ \text{eV}$, $100\ \mu\text{m} \times 100\ \mu\text{m}$ for $550\ \text{eV}$, $70\ \mu\text{m} \times 70\ \mu\text{m}$ for $750\ \text{eV}$ and $50\ \mu\text{m} \times 50\ \mu\text{m}$ for $930\ \text{eV}$ photons respectively. The monochromator grating was $300\ \frac{1}{\text{mm}}$ for $300\ \text{eV}$ photons and $1200\ \frac{1}{\text{mm}}$ for the rest. The total instrumental energy resolution was $610\ \text{meV}$, determined using the *Au* $4f$ line measured on a *Au* foil when the analyzer pass energy was set to $20\ \text{eV}$. Samples were freshly rinsed with reagent-grade isopropanol before being introduced to the beam line vacuum chamber and pumped to a base pressure low value of 10^{-10} Torr [81].

3.2.2.4. Peak Fitting in XPS

As introduced previously, changes in the chemical environment of an atom can be monitored by measuring the kinetic energy changes characteristic of the chemical state [66, 68]. In terms of XPS spectra, this phenomenon is reflected as an ensemble of peaks for an element rather than a single peak. Figure 3.3 presents *Nb3d* spectra measured from a BCP treated single crystal sample by using $930\ \text{eV}$ photon energy at different take-off angles with contribution identified as Nb^{5+} and Nb^0 through the value of the chemical shift ($\sim 5.64\ \text{eV}$ [1-2]). Further more subtle contributions to these peaks expected from Nb suboxides [1-2, 5, 12], may be identified through peak fitting.

For peak fitting in XPS, a basic knowledge of the chemistry involved suggests the number of chemical states. It is very important to introduce parameter constraints to force the peak modeling to obey the basic chemistry and physics of the studied

surface. For example, the restriction of the relative intensities of doublet pairs ($2j+1$, where $j = l \pm 1/2$, quantum number), are characterized by $2(l - 1/2) + 1 : 2(l + 1/2) + 1$. Thus, for d electrons, the doublet pairs (for example: $Nb3d_{3/2}$ and $Nb3d_{5/2}$) intensity are in the proportion 2/3 [65].

The shape of the spectrum background may be affected by inelastic energy loss processes, secondary electrons and nearby peaks [68, 81]. An effective description of the background is critical for modeling XPS spectra, especially for a spectrum containing both doublet pairs coupled with a variety of chemical shifts [82-85]. Four spectral background choices may be considered. (1) The linear background may be reasonably applied for spectra exhibiting small intensity differences between low energy and high energy sides of the peaks. (2) The Shirley background [86] has in many cases turned out to be an successful approximation for the inelastic background of core level peaks of buried species, which are affected by inelastic losses of the emitted photoelectron [48-49]. (3) The Tougaard [87-88] background was originally developed as an alternative to the Shirley background for transition metals, which includes a model shape of the energy loss function. The Tougaard background has been recommended for a spectrum with a large energy window towards lower kinetic energies or larger energy losses. It is therefore especially suited for asymmetrical signals like metal $4f$ lines [89]. (4) An additional model for the background consisting of a third order polynomial combined with the Shirley [90-93]. The polynomial function allows the description of the contribution of secondary electrons

at low kinetic energies. In order to obtain detailed chemical and physical parameters, it is absolutely necessary to include the background function in the iterative peak fitting procedures [93]; more detailed information can be found in references [90-93].

A combination of the physics involved in the ionization process and the distortions caused by the measurement mechanism results in the core level electrons ejected by x-rays to have spectra with a variety of shapes. An idealization of these influences for the observed peak can be specified as a convolution of Gaussian and Lorentzian functions [90, 92]. Due to a more complex photoexcitation process, most metal signals exhibit inherently asymmetric peak shapes [69-73]. For these reasons, fitting XPS spectra with synthetic line shapes requires a variety of functional forms. Typically, a class of functional form based on the Gaussian and Lorentzian functions is used for routine analysis of XPS spectra [93-96].

Both the height-normalized Lorentzian function $L(E)$

$$L(E) = [1 + (E - E_0) / \beta]^2]^{-1} \quad 3-14$$

and the Gaussian function $G(E)$

$$G(E) = \exp\{-\ln 2[(E - E_0) / \beta]^2\} \quad 3-15$$

are completely characterized by the peak parameters β , corresponding to $1/2$ of the full width at half maximum (FWHM) and E_0 , the peak position. Usually a product of Gaussian and Lorentzian functions with the same width [81]

$$f(E) = h \left\{ 1 + M \left[\frac{E - E_0}{\beta + \alpha(E - E_0)} \right]^2 \right\}^{-1} \times \exp \left\{ (-1 - M) \ln 2 \left[\frac{E - E_0}{\beta + \alpha(E - E_0)} \right]^2 \right\} \quad 3-16$$

where h is the peak height, α is the asymmetry index and M is the Lorentzian-Gaussian mixing ratio, or a convolution of independent Gaussian and Lorentzian (or Doniach-Sunjic type [82]), also called Voigt profile [91],

$$f(E) = f(L * G) = \int_{-\infty}^{\infty} L(E')G(E - E')dE' \quad 3-17$$

is used to describe XPS core level line shapes.

In order to extract the different components in the $Nb 3d$ spectra, a curve fitting procedure was applied and preceded by using a commercial XPS analysis software-Unifit 2006 [89] with certain parameter constraints. The background was modeled by adding a Shirley background to an exponential during the peak fitting [83-93]. A Doniac-Sunjic line shape was used with a Lorentzian width of 180 meV [94]. The Gaussian width of the oxide peaks was found by fitting the width of the Nb^{5+} component, since it is the most prominent one. The widths of the other oxide peaks were locked, but kept to a value close to the previous fitted width of the Nb^{5+} component. The spin split was set to 2.74 eV [11, 94] and the branching ratio was kept at $2/3$ [94]. The determination of peak position and intensities was iteratively carried out by a least square fitting routine and the Marquardt-Levenberg algorithm has been chosen to minimize the square error (χ^2) [91-93].

3.3. Results and Discussion

3.3.1. Surface Depth Profiling-ARXPS and Variable Energy XPS

In this study, variable photon energy XPS is used to gain an alternative view of how composition varies with depth. Angle-resolved data at fixed photon energy was also collected to better understand the relationship between the two approaches. Figure 3.3 presents the effect of varying takeoff angle at $h\nu=930\text{eV}$ for a BCP treated single Nb crystal. The $Nb3d$ spectra were collected at take off angles with respect to the surface normal of 0° , 41° and 60° , resulting in a factor of two variation in the probing depth. We found that even at 60° take off angle, there is evidently a trace of Nb metal signal, although some noise interferes. Spectra spanning the $Nb3d$ manifold were also collected at photon energies of 300eV , 550eV and 750eV as shown in Figure 3.4. Attenuation lengths calculated according to the modified TPP-2M equation [66, 74-76] was 0.94 nm , 1.39 nm , 1.75 nm for the same photon energies as above, and 2.69 nm for the 1253.6 eV Mg anode, 2.99 nm for the 1486.7 eV Al anode in Nb_2O_5 . This is a factor of three variation in depth sensitivity compared to the factor of two obtained by angle variation. Further, the two can be combined, compatible with the topography to obtain a factor of six. Note that for the single crystal niobium studied, the contribution from Nb metal is evident in datasets collected at 750eV and cannot be ignored at 550eV , but is not at all evident at 300eV . Comparing $Nb3d$ spectra (Figures 3.4 and 3.5) measured at varying angle and photon energy, we find the intensity from metal Nb changes more quickly with the latter. Evidently variable photon energy is more surface sensitive.

Figure 3.4 presents the results of curve fitting. The full line indicates the simulation and the dots represent various components. Given the high surface sensitivity, the $Nb3d$ spectrum obtained at the 0° take-off angle and using 300 eV (Figure 3.4a) can be accounted for almost entirely by the doublets associated with Nb_2O_5 at the binding energy 5.64 eV higher than that of metal. Figure 3.4b shows a $Nb3d$ spectrum collected at photon energies of 550 eV ; the metal Nb as well as some other oxides are evident. At the same take off angle, the use of 750 eV photons increases probing depth, the spectrum obtained (Figure 3.4c) shows further enhanced signals from the material below the Nb_2O_5 layer. The chemical identities of various oxides were identified by curve fitting are assigned according to reported binding energies and interpolated from Nb^{5+} and Nb^0 [1, 17, 19, 21, 28-32]. The binding energy associated with NbO_2 appears to be 1.4 eV below that of Nb_2O_5 , the NbO peaks appear to be 1.4 eV above that of the Nb metal (203 eV for $Nb3d_{5/2}$), and the Nb_2O peak is located at 0.8 eV above that of metal Nb , these values are in agreement with the values previously reported respectively [1, 17, 21, 51]. Taking the information depth as three times the attenuation length and assuming that the Nb oxide layer of single crystal niobium is only composed of Nb_2O_5 , suggests that the thickness of oxide layer on the single crystal Nb (111) oxide layer lies between 2.9 nm and 4.0 nm . This can be viewed as pure Nb_2O_5 approximately 3 nm thick, and between it and underlying metal is a structural transition zone of suboxides with a thickness not larger than one nanometer. Whether an explicit layer structure and

discrete phases of suboxide actually exist could not be well determined through XPS measurement itself. Previous workers have reported an oxide layer thickness of 4 ± 0.2 nm for polycrystalline *Nb* [1] and 3.3 nm for single crystal *Nb* (100) [17]. Others [4, 11] indicate that the thickness of the Nb_2O_5 layer is about 6 nm .

Observations of the effect of thermal processing on silicon field effect transistors motivated detailed exploration of the interface between silicon and thin (0.5~3 nm) amorphous surface oxides [95-96]. The availability of atomically-flat silicon wafers and the optical transparency of SiO_2 made possible the incisive application of several characterization tools, combined with computational modeling based on the bond constraint theory of network solids. The results indicate a 1~2 monolayer equivalent suboxide interfacial layer with an average composition equivalent to SiO . A strained zone is present in the *Si* adjacent to the interface. The dominant factor controlling the interface structure and composition is bond strain. Though there are many differences from the situation of niobium oxide on niobium, it is an intriguing possibility that bond strain may drive the formation of a suboxide accommodation zone at the interface, including strain effects in the adjacent metal.

3.3.2. Surface Oxide Before and After Low T Baking

As discussed above, it has been widely observed that baking a cavity at low temperature (110~140°C) can achieve a strong reduction of the Q-drop and an improvement of maximum accelerating field of about 10% ~20% [43-44]. Since the penetration depth of the RF current is only about 40 nm [25, 41], it is experimentally important to investigate the changes in the niobium surface due to different baking

practice in parallel to RF tests on cavities. In this study, samples were annealed at temperature of 120°C and 165°C in UHV (10^{-9} torr) using a tungsten filament located on the back of the samples or air-baking at 120 °C or 165 °C in a class (100) clean room using a closed heating stage.

Figures 3.5a and 3.5b show a typical picture of BCP/EP treated $Nb\ 3d$ spectra before and after 120°C, 48 hrs *in-situ* baking -the typical post-treatment used for SRF cavity processing. The results show that at this temperature the top Nb_2O_5 layer is partially transformed to suboxides, with evident decreased Nb^{5+} associated doublet intensity and increased of suboxides-associated peaks. The increase of metal doublet intensity is interpreted as a thinning of the total oxide layer. Since the surface oxide of EP niobium seems to be affected by EP processing parameters [96], the present XPS measurements were conducted on BCP treated single crystal niobium in parallel with performance studies done for large grain cavities.

3.3.2.1. Effect of Baking Temperature

Measurements of low field superconducting parameters suggest that oxygen diffusion was involved in the effect of low-temperature baking [46, 49, 54-55, 97-99]. A model based on reduced lower critical field due to interstitial oxygen near the interface of surface oxide and underlying metal has been refined to provide an explanation for “Q-drop” and the baking effects [49]. A recent study has shown that 3 hrs, 160°C *in situ* baking for post-purified polycrystal cavities achieved the same effect as that of 120°C for over 48 hrs baking [98].

In order to investigate the effect of baking temperature on the niobium surfaces, especially as expected to give experimental evidence consistent with oxygen diffusion under different kinetic conditions, the samples were baked at 120°C for 12 hrs, at 160°C for 3 hrs and 12 hrs respectively at low value of 10^{-9} torr. Our results show that 160°C, 3hrs baking causes almost the same amount of Nb_2O_5 to transform to suboxides as that of 120°C, 12 hrs and a long baking duration for higher temperature produces more Nb_2O_5 transformation. The corresponding $Nb3d$ spectra before/after 120°C, 12 hrs and 160°C, 3 hrs baking; before/after 120°C, 12 hrs and 160°C, 12 hrs baking are shown in Figures 3.6 and 3.7.

3.3.2.2. Effect of Baking Duration

As introduced previously, *in-situ* baking for shorter duration (120 °C, 3 hrs) was surprisingly found to be sufficient to reduce most of the hot spots up to a quench field for a large grain single cell cavity [46]. To explore this, the Nb samples were baked at 120°C for 3 hrs, 6 hrs, 12 hrs, or 24 hrs. The results show that longer baking leads to more extensive disappearance of Nb_2O_5 as shown in Figure 3.8. In contrast to previous studies [17], the results suggest the average oxide layer thickness keeps decreasing with the baking time as shown in Figure 3.9-the intensity ratio of

$\frac{I_{Nb^{(0<rs>)}}}{\sum I_{Nb}}$ decreases with the baking duration following a linear relationship.

A number of cavity studies have shown that the improvement achieved through low temperature baking is maintained for more than a few months' air exposure [43-44]. However, the results of this work show that after a few hours air-exposure, the

change of oxide layer associated with Nb_2O_5 transformation disappeared and the spectra cannot be distinguished from those obtained prior to baking (Figure 3.10). For clarity, after air exposure, only $Nb 3d$ spectra of 3 hrs and 12 hrs baking are shown in Figure 3.10 together with that of non-baked. These results show no change of surface niobium oxide for samples subjected to longer duration of baking once they were exposed to air. The results give strong evidence that the change of suboxides created by *in situ* baking is not responsible for the improved SRF cavity performance.

3.3.2.3. Effect of Air Baking

Recent studies proposed that baking in air at atmospheric pressure could be carried out with the same benefit as UHV baking [98]. Different temperature air-baking was also conducted on large grain single cell cavities to investigate the validity of the oxygen diffusion model [46]. It was found that baking the cavity in air at 120°C for 3 hrs achieved an improvement similar to that of *in-situ* baking [46]. However, baking at 180°C for 12 hrs caused uniformly distributed “anomalous” losses which could not be recovered by subsequent HF rinse and 120 °C *in-situ* baking [46]. XPS measurement have been motivated to investigate the change of surface oxide created by air baking for BCP treated single crystal samples. Instead of the dissociation of Nb_2O_5 observed from vacuum baking, air baking at 120°C produces a thicker Nb_2O_5 layer (4~4.5 nm) than that of *in-situ* baking as shown in Figure 3.11. The higher baking temperature in air is expected to promote more oxygen diffusion through the oxide into the niobium. For air baking at 165°C, our results show that $Nb 3d$ spectrum measured with $h\nu = 930 eV$ consists exclusively

of the doublet of Nb^{5+} . It was barely possible to detect Nb metal by using 1486.6 eV Al anode (this work was done by using *PHI Quantera XPS*), suggesting that the thickness of Nb_2O_5 layer increases to 9 nm.

3.4. Conclusion

Variable photon energy XPS probes the near-surface composition more incisively and provides better depth analysis than does angle-resolved XPS. The surface oxide layer of single crystal *Nb* (111) is composed of 3 nm Nb_2O_5 and underlain by nanometer suboxides. XPS studies show that after baking, Nb_2O_5 is partially transformed into suboxides, and the total oxide layer becomes thinner. Upon subsequent air exposure, the change of oxide layer observed after baking almost disappears. Evidently, suboxides created by *in situ* baking are not responsible for improved SRF cavity performance, since cavities still keep good performance after subsequent air-exposure eliminates the created change of suboxides. Compared with 120°C baking, higher baking temperature (165°C) transforms more oxide. 3 hrs, 160°C baking makes almost the same amount of oxide transformation as that of 12 hrs, 120°C baking. Air baking produces a thicker oxide layer. Longer baking time at 120°C (3hrs ~12hrs) increases Nb_2O_5 reduction and transformation. From these XPS studies, it has not yet been possible to identify a relationship between the changes in the niobium oxide layer caused by low T baking and the observed performance improvement of niobium cavities.

3.5. References

1. Q. Ma, and R.A. Rosenberg, *Appl. Surf. Sci.*, 206(1-4) (2003), pp. 209-17.
2. Q. Ma, and R.A. Rosenberg, "Proceedings of the 2001 Particle Accelerator Conference", Piscataway, NJ, 2 (2001), pp.1050.
3. J. Halbritter and A. Darlinski. *IEEE Transactions on Magnetics*, MAG-23(2) (1987), pp.1381.
4. A. Dacca, G. Gemme, L. Mattera, and R. Parodi, *Appl. Surf. Sci.* 126(3-4) (1998), pp. 219.
5. A. Darlinski, and J. Halbritter, *Surf. Interf. Anal.* 10(5) (1987), pp. 223.
6. J. Halbritter, *IEEE Transactions on Magnetics*, MAG-21(2) (1985), pp.858.
7. J. Halbritter, *J. the Less-Common Metals*, 139(1) (1988), pp.133.
8. J. Halbritter, *Surf. Interf. Anal.*, 12(1-12) (1988), pp.354.
9. J. Halbritter, *Appl. Phys. A- Solids & Surfaces. A* 43(1) (1987), pp. 1.
10. J. Halbritter, *Solid State Communications*. 34(8) (1980), pp. 675.
11. M. Grundner, and J. Halbritter, *J. Appl. Phys.*, 51(1) (1980), pp. 397.
12. A. Darlinski, and J. Halbritter. *J. Vac. Sci. Technol., A*. 5(4) (1987), pp.1235.
13. A. Dacca, G. Gemme, L. Mattera , and R. Parodi, *Surf. Sci. Spec.*, 5(4) (1998), pp. 332.
14. C. Z. Antoine, et al., *Proceeding of the 9th Workshop on RF Superconductivity*, Santa Fe, NM, (1999) p.109

15. C. Z. Antoine, et al., Proceeding of the 9th Workshop on RF Superconductivity, Santa Fe, NM, (1999), pp.295.
16. C. Z. Antoine, J. Appl. Phys., 81(4) (1997), pp. 1677.
17. Q. Ma, and R.A. Rosenberg, J. Appl. Phys., 96(2004), pp. 7675.
18. J. Halbritter, Electro. Acta., 34 (8) (1989), pp. 1153
19. B. R. King, H. C. Patel, D. A. Culino, and B. J. Tatarчук, Thin Solid Film, 192(1990), pp. 351.
20. B. R. King, and B. J. Tatarчук, Thin Solid Film, 192(1990), pp. 371.
21. M. Grundner, and J. Halbritter, Surf. Sci., 136(1984), pp. 44,
22. A. Septier , Proceeding of the 2nd Workshop on RF Superconductivity, KfK, 3019, (1980), pp.53.
23. J. Halbritter, Appl. Phys., A 43(1987), pp. 1.
24. A. Das Gupta, W. Gey, H. Kupfer, J. Halbritter, J. A. Yasaitis, J. Appl. Phys., 47(1976), pp. 2146.
25. H. Padamsee, Superconductor Science & Technology, 14(4) (2001), pp. 28.
26. J. Halbritter, Proceeding of the 38th Eloisatron Workshop, Elice (1990), pp.9.
27. R. Ballantini, and R. Parodi., Proceeding of the 9th Workshop on RF Superconductivity, Santa Fe, NM (1999), pp.211.
28. P. C. Karulkar, and J. E. Nordman, J. Vac. Sci. Technol., A. 7(1) (1980), pp. 462
29. J. M. Sanz, and Hofmann, J. Less-Common Met., 92(1983), pp. 317.
30. M. K. Bakl, J. Phys. Chem. Solids, 36(1975), pp. 485.

31. R. Fontaine, R. Caillat, L. Feve, and M. Guittet, *J. Electron Spectrosc Relat. Phenom.*, 10, (1977), pp. 349.
32. W. S. Lo, H. H. Chen, T. S. Chien, C. C. Tsan. B. S. Fang, *Surf. Rev. Lett.*, 4(1997), pp. 651
33. P.L.J.Gunter, and J. W. Niemantsverdriet, *J. Vac. Sci. Technol., A*. 13(3) (1995), pp. 1290.
34. W. S. Werner, and I. S. Tilinin, *J. Vac. Sci. Technol., A*. 12(4) (1994), pp. 2337.
35. P.L.J.Gunter, and J. W. Niemantsverdriet, *Appl. Surf. Sci.*, 89 (1995), pp. 69.
36. P.L.J.Gunter, and J. W. Niemantsverdriet, *Appl. Surf. Sci.*, 105(1997), pp. 342.
37. P. Mark, R. G. White, J. Wolstenholme, and T. Conard, *Appl. Surf. Sci.*, 252(2006), pp. 8270.
38. H.C. Poon, and S. Y. Tong, *Phys., Rev. B* , 30(10) (1984), pp. 6211
39. M. Sreemany, and T. B. Ghosh, *Appl. Surf. Sci.*, 90(1995), pp. 241
40. J. F. Moulder, W. F. Stickle, P. E. Sobol, and K. D. Bomben, "*Handbook of X-ray Photoelectron Spectroscopy*", Physical Electronic, Inc., Eden Prairie, MN(1995).
41. H. Padamsee, J. Knobloch, and T. Hays, "*RF Superconductivity for Accelerators*", Wiley, New York (1998).
42. <http://srf.jlab.org/>

43. P. Kneisel, et al., Proceeding of the 9th Workshop on RF Superconductivity, Santa Fe, NM, (1999), pp. 328.
44. B. Visentin, J. P. Charrier, B. Coadou, Proceeding of the 1998 European Particle Accelerator Conference, Stockholm, Sweden (1998), pp. 1885.
45. G. Ciovati, P. Kneisel, and A. Gurevich, PhysRevSTAB, 10 (062002) (2007), pp.1.
46. G. Ciovati, Ph.D thesis, Old Dominion Univ., (2005)
47. G. Ciovati, J. Appl. Phys, 96(2004), pp. 1591.
48. G. Ciovati, Appl. Phys. Lett., 89(2006), pp. 22507
49. J. Halbritter, Proceeding of the 10th Workshop on RF Superconductivity, Tsukuba, Japan (2001), pp. 291.
50. J. Knobloch, R. L.Geng, M.Liepe, and H. Padamsee, "Proceeding of the 9th Workshop on RF Superconductivity", Sante Fe, NM (1999), TUP 004.
51. H. Safa, Proceeding of the 10th Workshop on RF Superconductivity, Tsukuba, Japan (2001), pp. 279.
52. I. Arfaoui, C. Cuillot, J. Cousty, and C. Antoine, J. Appl. Phys., 91(2002), pp. 9319
53. A. Romanenko , Proc. of 13th SRF workshop, Beijing, China (2007), TU103, <http://www.pku.edu.cn/academic/srf2007/proceeding.html>
54. G. Ciovati, Physica C, 441, (2006), pp. 57
55. T. Wang, C. Reece, R. M. Sundelin, J. Vac. Sci. Technol. B, 21(4) (2003), pp. 1230.

56. H. Tian, C. Reece, M. Kelley, Proceedings of the 11th Workshop on RF Superconductivity, Travemünde, Germany (2003), MOP 15.
57. K. Siegbahn, C. Nordling, A. Fahlman, R. Nordberg, K. Hamrin, J. Hedman, G. Johansson, T. Bergmark, S-E. Karlsson, I. Lindgren, and B. Lindberg, "*ESCA: Atomic, Molecular and Solid State Structure Studied by Means of Electron Spectroscopy*", Almqvist & Wiksells Boktryckeri AB, Uppsala, (1967).
58. H. Siegbahn and K. Siegbahn, J. Electron. Spectrosc. Relat. Phenom., 2(1973), pp. 319.
59. H. Siegbahn, L. Asplund, P. Kelfve, K. Hamrin, L. Karlsson, and K. Siegbahn, J. Electron. Spectrosc. Relat. Phenom., 5 (1974), pp. 1059.
60. H. Siegbahn, L. Asplund, P. Kelfve, and K. Siegbahn, J. Electron. Spectrosc. Relat. Phenom., 7 (1975), pp. 411.
61. H. Fellner-Felldge, H. Siegbahn, L. Asplund, P. Kelfve, and K. Siegbahn, J. Electron. Spectrosc. Relat. Phenom., 7(1975), pp. 421.
62. B. Lindberg, L. Asplund, H. Fellner-Felldge, P. Kelfve, H. Siegbahn, and K. Siegbahn, Chem. Phys., let., 39 (1976), pp. 8.
63. H. Siegbahn, S. Svensson, and M. Lundholm, J. Electron. Spectrosc. Relat. Phenom. 24 (1981), pp. 205.
64. P. K. Ghosh, "*Introduction to Photoelectron Spectroscopy*", John Wiley & Sons, New York (1983)
65. J. C. Wickerman, "*Surface Analysis-The Principle Techniques*", John Wiley & Sons, New York (2000).

66. C. R. Brundle, J. C. A. Evans, and S. Wilson, "*Encyclopedia of Material Characterization: Surface, Interface, Thin Films*", Butterworth-Heinemann, Boston (1992).
67. M. P. Seah, and D. Briggs, "*Practical Surface Analysis*" Vol. 1, John Wiley & Sons, New York (1990).
68. M.P. Seah, Surf. Interf. Anal., 2 (1980), p. 222.
69. M.P. Seah, I. S. Gilmore, and S. J. Spencer, J Electron Spectrosc Relat Phenom., 120 (2001), pp. 93.
70. H. Shimada, N. Matsubayashi, M. Imamura, T. Sato, and A. Nishijima, Appl. Surf. Sci., 100/101 (1996), pp.56.
71. S. Tougaard, Surf. Interf. Anal., 11 (1988), pp. 453.
72. S. Tougaard, and H.S. Hansen, Surf. Interf. Anal., 14 (1989), pp. 730.
73. S. Tougaard, J. Electron Spectrosc., 52 (1990), pp. 243.
74. S. Tougaard, J. Vac. Sci. Technol., A(8) (1990), pp. 2197.
75. S. Tougaard, "QUASES: Software Package for Quantitative XPS/AES of Surface Nano-Structures by Inelastic Peak Shape Analysis" (1994).
76. S. Tanuma, C.J. Powell, D.R. Penn, Surf. Interf. Anal., 17(1991), pp. 911.
77. S. Tanuma, C.J. Powell, D.R. Penn, Surf. Interf. Anal., 17(1991), pp. 927.
78. W. H. Gries, Surf. Interf. Anal., 24(1996), pp. 38.
79. J. A. Samson, and D. L. Ederer, "Vacuum Ultraviolet Spectroscopy, Experimental Methods in the Physics Science", Academic Press (2000).

80. C. D. Wagner, "*Handbook of X-ray Photoelectron Spectroscopy*", Physical Electronic, Inc., Eden Prairie, MN(1976)
81. Doniach and Sunjic, J. Phys. C: Solid State Phys., 3 (1970), pp. 285.
82. P.M. van Attekum and G.K. Wertheim, Phys. Rev. Lett., 43 (1979), pp. 1896.
83. D.R. Penn, Phys. Rev. Lett., 40 (1978), pp. 568.
84. S. Tougaard, Phys. Rev., B 34 (1986), pp. 6779
85. D. R. Shiley, Phys. Rev., B 5 (1973), pp. 4709.
86. S. Tougaard, Solid State Comm., 61(1987), pp. 547.
87. S. Tougaard, J. Vac. Sci. Technol., A (5) (1987), pp. 1275.
88. M.P. Seah, and I. S. Gilmore, Phys. Rev., B 73 (2006), pp. 174113.
89. R. Hesse, T. Chasse, P. Streubel, and R. Szargan, Surf. Interf. Anal., 36 (2004), pp. 1373.
90. R. Hesse, P. Streubel, and R. Szargan, Surf. Interf. Anal., 39 (2007), pp. 381.
91. R. Hesse, P. Streubel, and R. Szargan, Surf. Interf. Anal., 37 (2005), pp. 589.
92. R. Hesse, T. Chasse, and R. Szargan, Fresenius J. Anal. Chem., 365(1999), pp. 48.
93. F. Strisland, A. Ramstad, C. Berg and S. Raaen, Philosophical Magazine Lett. 78(3) (1998), pp. 271
94. G. Lucovsky, and J.C. Phillips, J. Vac. Sci. Technol. B22 (4) (2004), pp. 2087.
95. M. D. Ufich, J.E. Dowe, J.W. Keister. H. Niimi, L. Fleming, and G. Lucovsky, J. Vac. Sci. Technol. B24 (4) (2006), pp. 2132.

96. I. Sieber, H.Hildebrand, A. Friedrich and P.Schmuki, *Electrochem. Comm.* 7, (2005), pp. 97,
97. B.Visentin, Y. Gasser, and J. P. Charrier, *Physica C*, 441 (2006), pp. 66
98. P. Kneisel, *Proceedings of the 1st SRF Workshop, Karlsruhe (1980)*, pp. 27

Nb ³⁺ (Nb ₂ O ₅)		Nb ⁴⁺ (NbO ₂)		Nb ⁴⁺ (NbO)		Nb ⁵⁺ (Nb ₂ O)		Nb ⁰ (metal)		Ref
3d _{3/2}	3d _{5/2}	3d _{3/2}	3d _{5/2}	3d _{3/2}	3d _{5/2}	3d _{3/2}	3d _{5/2}	3d _{3/2}	3d _{5/2}	
—	207.6	—	206.3 ± 0.1	—	203.6	—	203 ± 0.3	—	202.2	1, 32
—	207.8	—	206.6	—	—	—	—	—	202.3	2
—	207.6	—	206.1	—	203.2	—	—	—	202.3	13
—	207.5	—	205.9	—	203.0	—	—	—	202.2	3-5 11-12
210.0	207.2	208.8	206.0	206.8	204.0	—	—	205.2	202.2	28
209.9	207.2	208.6	205.9	206.6	203.9	—	—	204.7	202.0	29
—	207.5	—	205.9	—	203.0	—	—	—	202.2	30
210.2	207.4	208.8	206.0	207.0	204.2	—	—	205.1	202.3	31

Table 3.1: Reported binding energy positions of the Nb3d_{3/2-5/2} doublets (unit: eV).

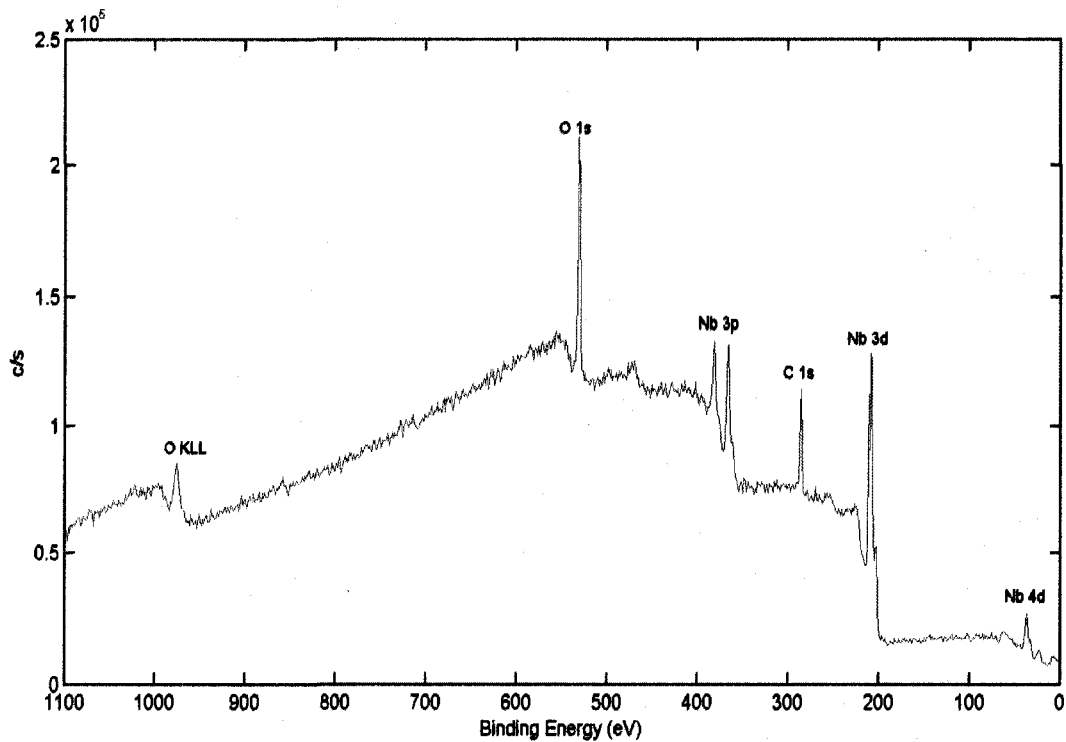


Figure 3-1: A wide range spectrum of a buffed chemical polishing BCP treated single crystal niobium collected at 45° take off angle relative to the surface normal with monochromated Al anode.

Parameters	Nb_2O_5
$\rho(g/cm^3)$	4.60
M	265.8
β_m	0.009
γ	0.041
C	1.21
D	36.09
ν	1.29
$E_g (eV)$	3.3~3.4 [28]
N_v	40
$E_p (eV)$	34.61
$E_F^b (eV)$	207.9

Table 3.2: The parameters in TPP-2M equation used for calculating the inelastic mean free path (IMFP) for Nb_2O_5 at the different photon energy (Courtesy of S. Tanuma, C. J. Powell, D. R. Penn, Surf. Interf. Anal., 17, 1991, pp. 911, S. Tanuma, C. J. Powell, D. R. Penn, Surf. Interf. Anal., 17, 1991, pp. 927, and W. H. Gries, Surf. Interf. Anal., 24, 1996, pp. 38.)

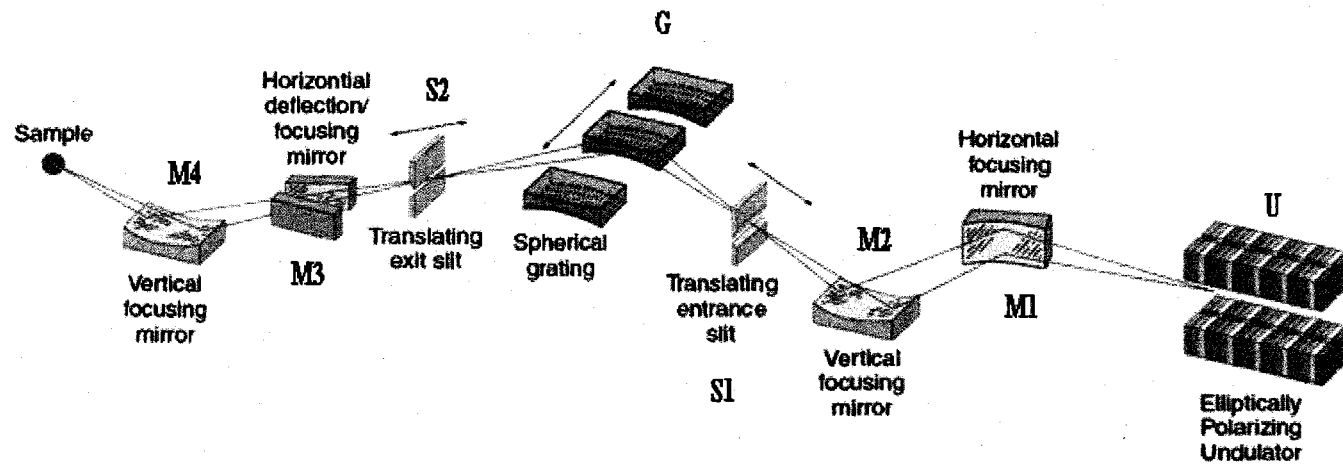


Figure 3.2: A schematic diagram of the arrangement of the components used at the beamline X1B, NSLS

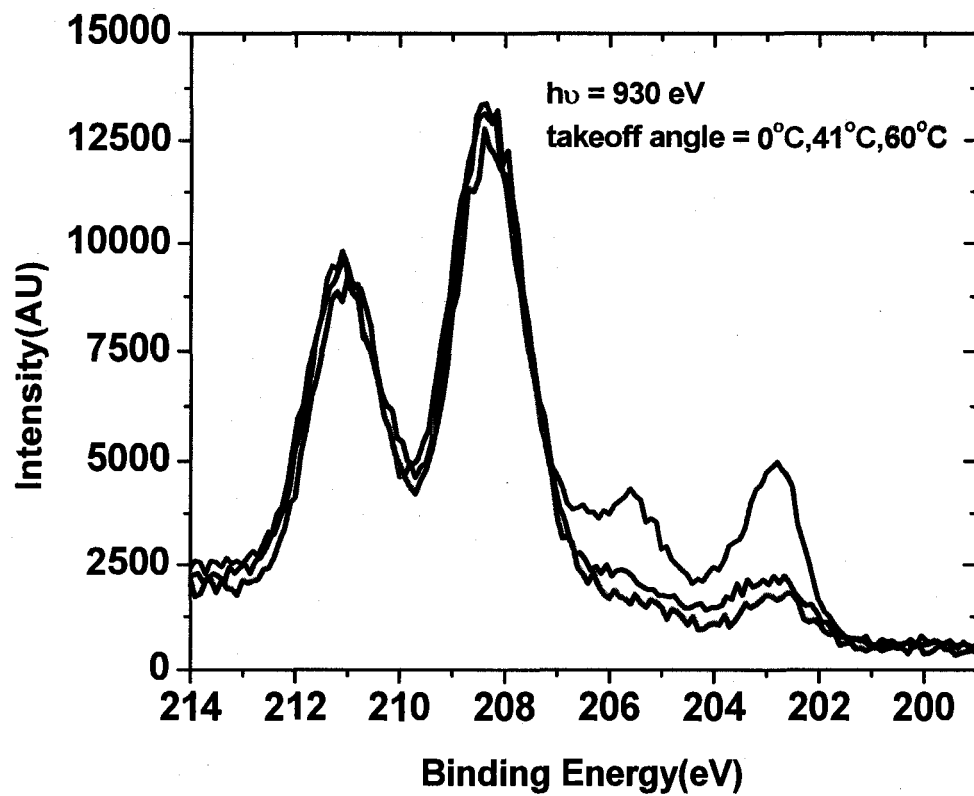


Figure 3.3: $Nb 3d$ spectra of BCP treated single crystal collected using 930 eV at take off angles 0°(red), 41°(blue) and 60°(olive) relative to the surface normal.

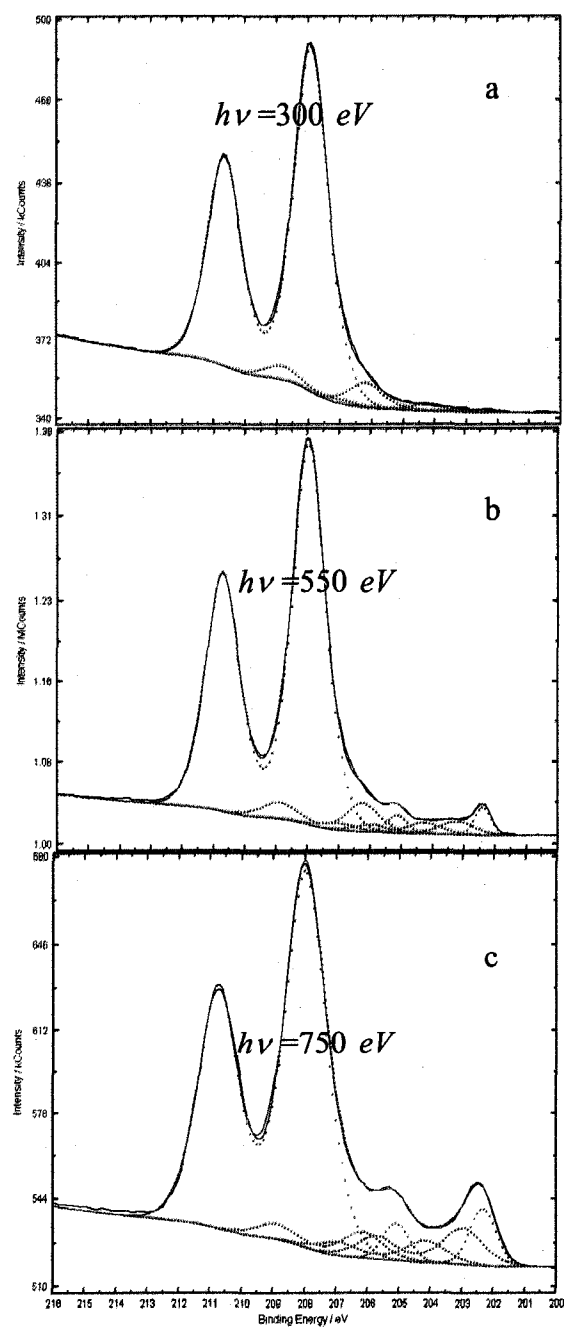


Figure 3.4: *Nb 3d* spectra of BCP treated single crystal collected at 0° take off angle relative to the surface normal using 300 eV (a), 550 eV (b) and 930 eV (c) photons. (The full line indicates the simulation and the dots represent various components)

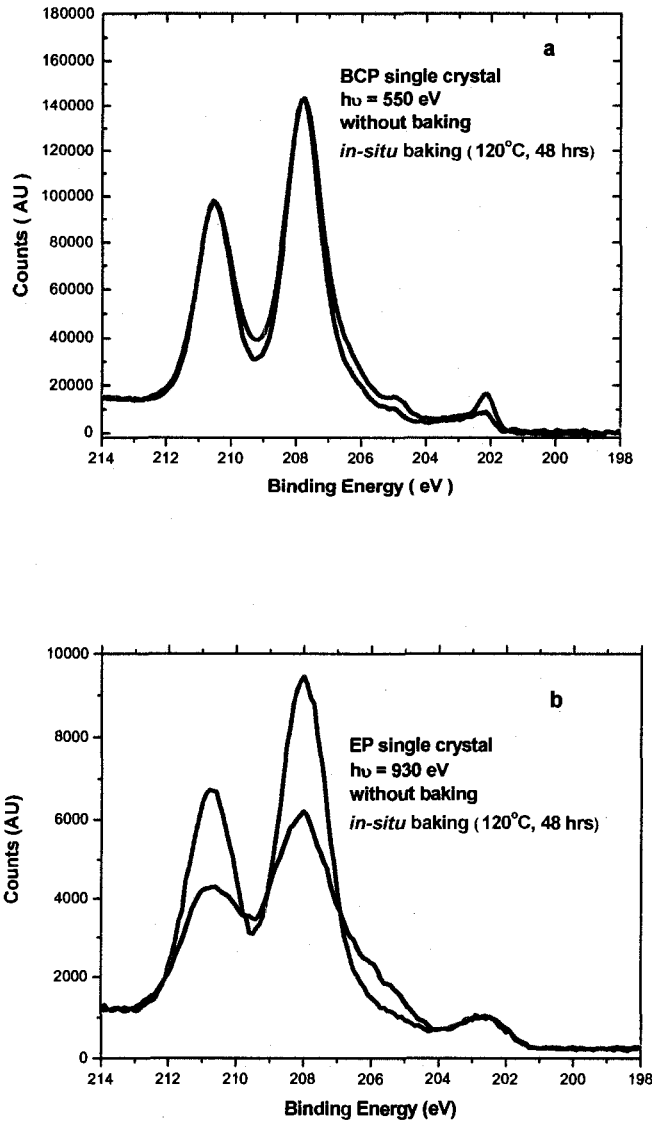


Figure 3.5: a) BCP and b) EP single crystal $Nb\ 3d$ spectra before (blue) and after (red) low T baking (120°C, 48 hrs, 10^{-9} torr). The top Nb_2O_5 layer is partially transformed to suboxides, evident decreased Nb^{5+} associated doublet intensity and increased of suboxides-associated peaks.

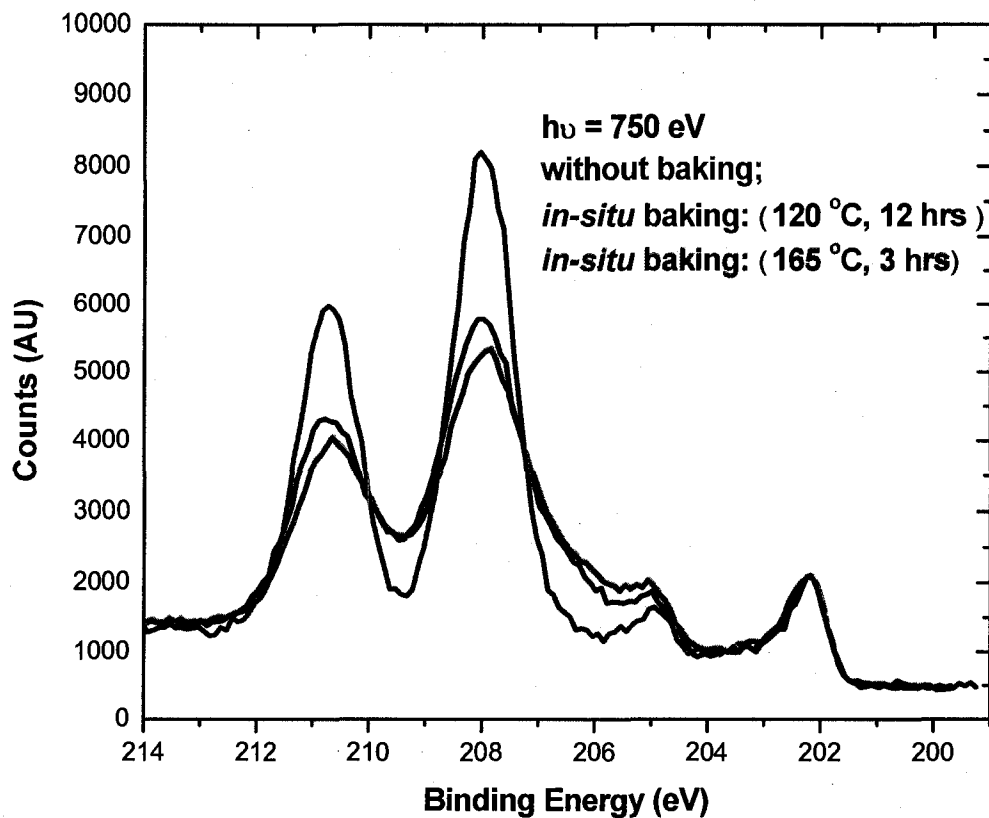


Figure 3.6: *Nb 3d* spectra before (red), after 120°C for 12 hrs (blue), and 165°C for 3 hrs (olive) *in-situ* baking. 160°C, 3hrs baking causes almost the same amount of Nb_2O_5 to transform to suboxides as that of 120°C, 12 hrs

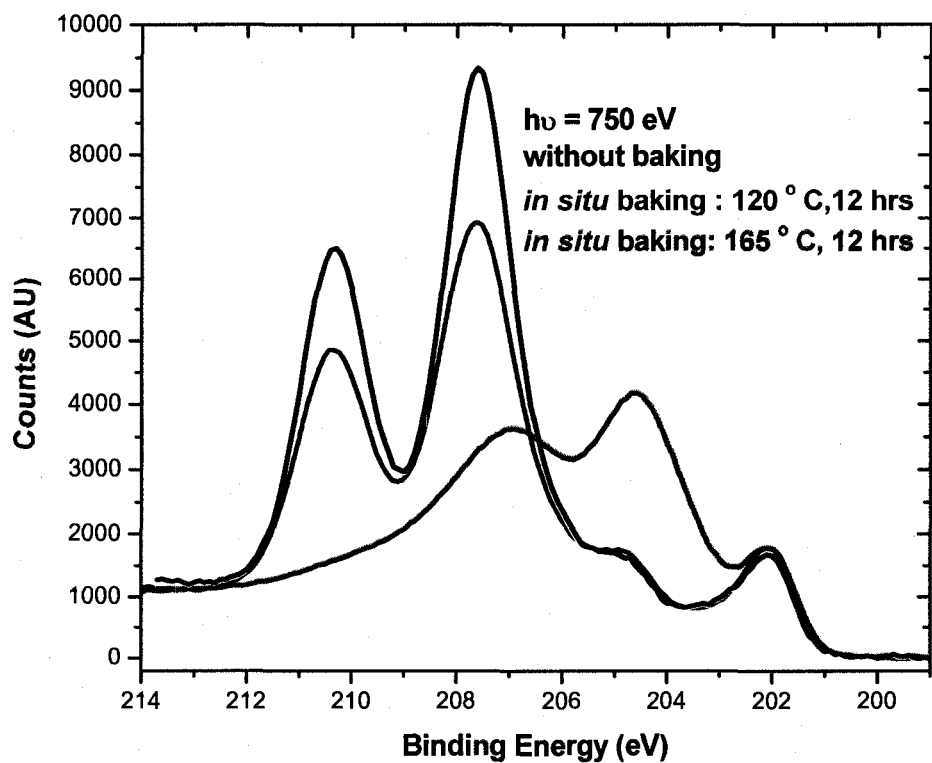


Figure 3.7: *Nb 3d* spectra before (black), after 120°C for 12 hrs (red), and 165°C for 12 hrs (olive) in-situ baking. A long baking duration for higher temperature produces more Nb_2O_5 transformation.

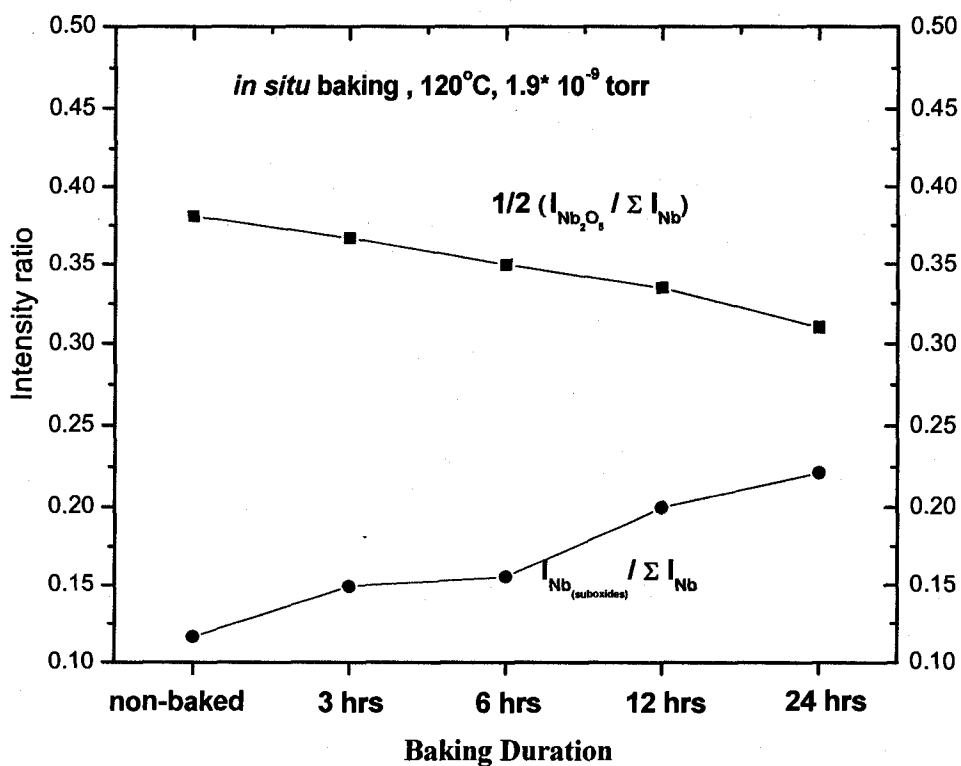


Figure 3.8: The intensity ratio of $\frac{I_{Nb_2O_5}}{\sum I_{Nb}}$ decreases with the baking duration, the

intensity ratio of $\frac{I_{Nb_{suboxides}}}{\sum I_{Nb}}$ increases with the baking duration.

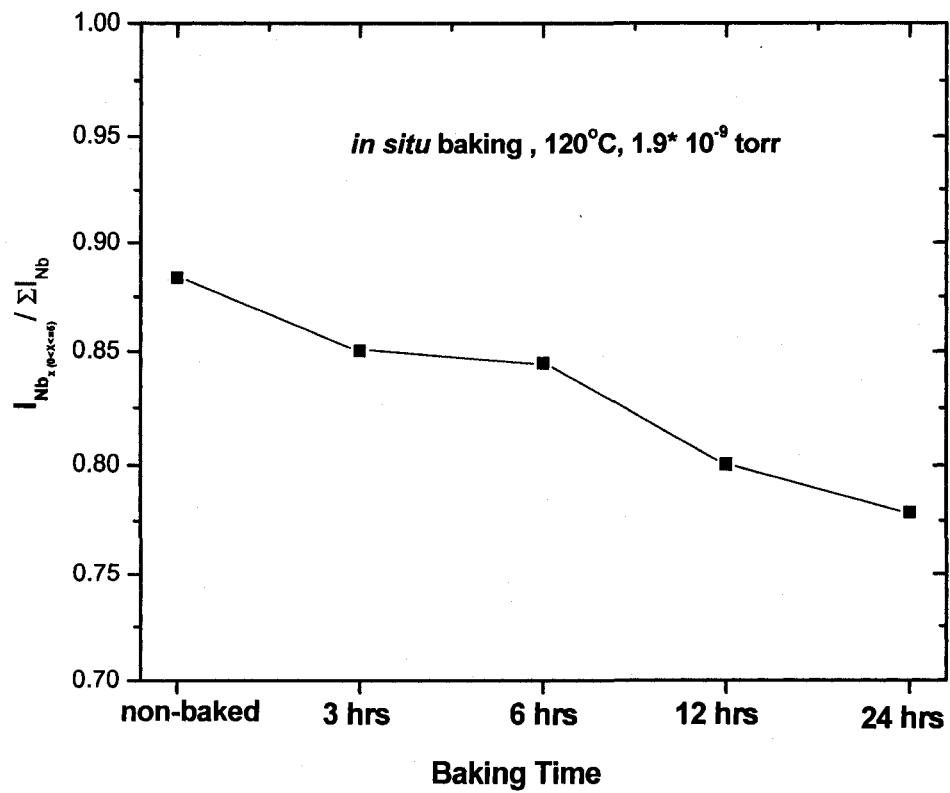


Figure 3.9: The intensity ratio of $I_{Nb_x(0 < x < 5)} / \sum I_{Nb}$ decreases with the baking duration.

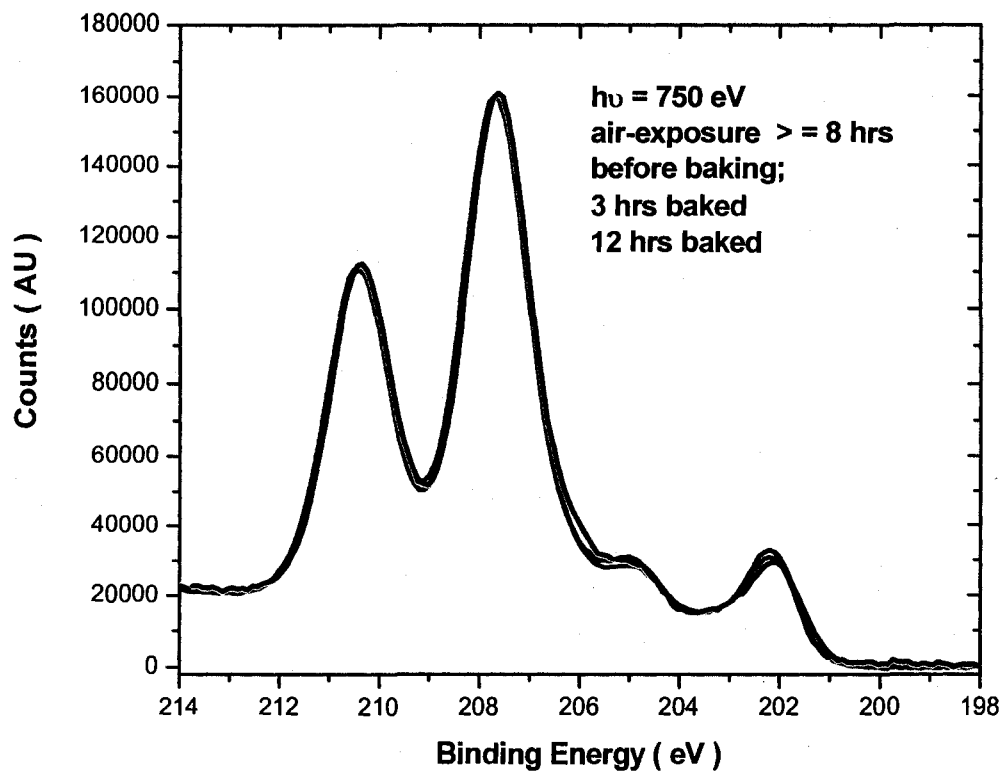


Figure 3.10: Nb 3d spectra after over 8 hrs air-exposure (*in situ* baked at different duration—black: before baking; red: 3hrs bake-out; blue: 12 hrs bake-out). The change of oxide layer associated with Nb_2O_5 transformation disappeared and the spectra cannot be distinguished from those obtained prior to baking

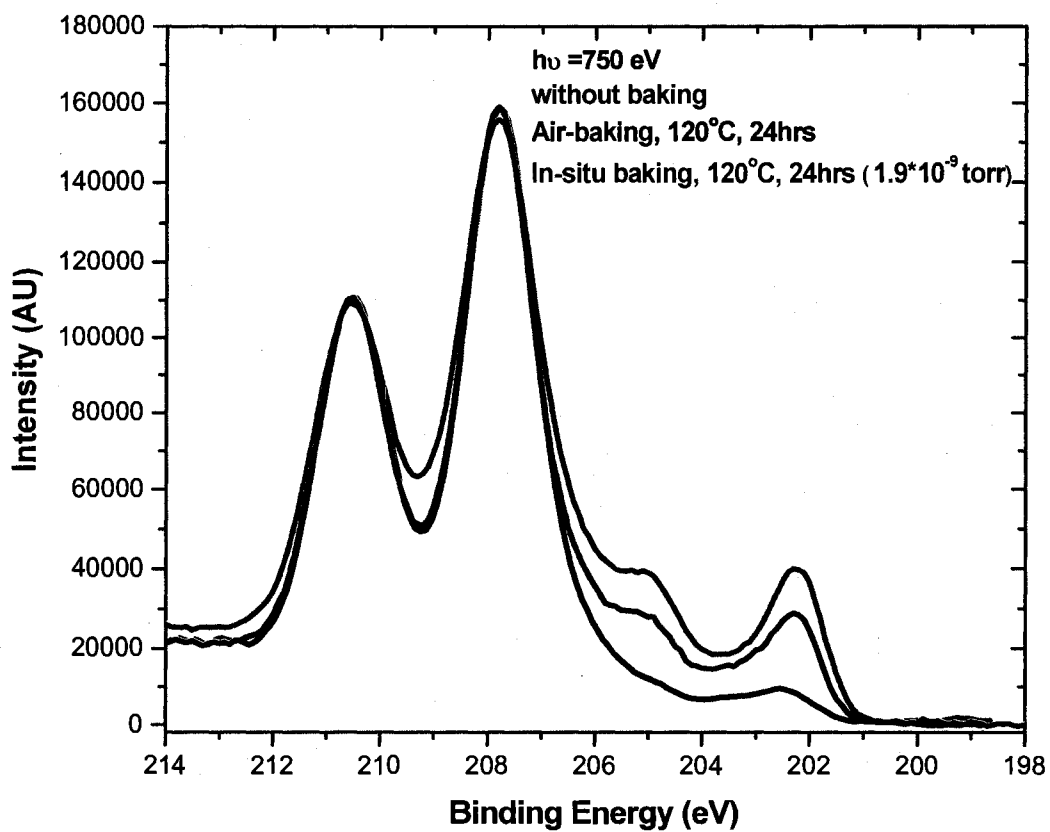


Figure 3.11: $Nb 3d$ spectra before (blue), after 120°, 24 hrs in situ baking (red) and air baking (black). Air baking at 120°C produces a thicker Nb_2O_5 layer (4~4.5 nm) than that of *in-situ* baking.

CHAPTER 4

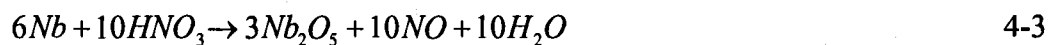
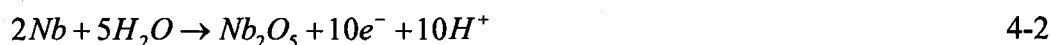
Surface Study of Niobium Buffered Chemical Polished (BCP) under Conditions for SRF Cavity Production*

4.1. Introduction

The performance of superconducting radio frequency (SRF) cavities used in modern accelerators is intimately related to the final surface treatments. In order to remove damaged and contaminated layers of material due to handling and machining, the cavities are chemically etched to obtain a smooth and polished surface. Buffered chemical polishing has been the most widely used etch technology since SRF began in the 1970's. Typically, a BCP solution consists of a 1:1:1 or 1:1:2 (volume) mixture of HNO₃ (69%), HF (49%) and H₃PO₄ (85%). During chemical polishing, phosphoric acid acts as a buffer, and nitric acid is an oxidizing agent of *Nb* which produces niobium pentoxide (Nb_2O_5). Hydrofluoric acid reacts with Nb_2O_5 and

(* This chapter has appeared as Applied Surface Science, Vol. 253(3), 2006, p.1236-1242)

produces soluble Nb-fluoride or Nb-oxifluoride. The chemistry possibly involved is summarized as follows:



At Jefferson lab, buffered chemical polishing is done in a closed cabinet where BCP solutions flows end-to-end through the cavity at approximately 10 °C for a time sufficient to remove the mechanically-damaged and contaminated layer. The cavity shapes used for accelerator applications result in considerably different surface flow rates during normal processing; a non-uniform surface finishing may be expected.

Typically, niobium surface topography was characterized using different instruments, with a range of sizes and resolutions, including profilometry and atomic force microscopy (AFM). Usually, root mean square (RMS) roughness is used to describe Nb surface roughness. The use of surface spectroscopy, predominantly XPS, to examine the surface chemistry of niobium subsequent to cavity production began to be reported more than 25 years ago and continues to the present day [2, 4-21]. The

surface chemistry of niobium is dominated by high reactivity toward oxygen [4, 22]. The outermost layers are always found to be dielectric Nb_2O_5 . In the work reported here, we examined the reproducibility of surface topography and chemistry in detail, since this appears not to have been done previously. The effect of post-fabrication BCP etching, under conditions typical of SRF cavity production, on surface chemistry and topography of bulk polycrystalline niobium has also been systematically studied. In this chapter, Section 2 describes the experimental studies. The results and discussion are presented in section 3. Section 4 concludes the study.

4.2. Experimental Studies

4.2.1. Sample Preparation

Conical buttons, 10 mm diameter base, 5 mm diameter top and 3 mm thick Nb were cut from the same polycrystalline *Nb* sheet used to make SRF cavities, having purity of 99.9999% and a RRR (residual resistivity ratio) ~ 452 according to the vendor-Wah Chang. Details of the conversion of purified *Nb* ingot to sheet are not disclosed, but it is generally understood to employ successive stages of cross-rolling with intermediate heat treatment. To obtain well-defined, uniform surface flow rates during etching, we constructed a “Teflon” disc 10 mm thick and 50 mm in diameter. Slots were cut to hold the conical samples, small face outward, protruding slightly from the disc rim (see Figure 4.1). Rotating the disc immersed in solution with its axis vertical afforded constant surface velocity. Moreover, all samples in a set entered and were removed from the BCP solution simultaneously. Materials treated with no

disc rotation are called “static” below; others are identified by their surface flow rates. This treatment at room temperature for 100 min removes a weight equivalent to about 200 μm of material, which has been found to eliminate any trace of mechanical damages from the surface [23]. To remove acid residue and particles on samples introduced during handling, the samples were ultrasonically rinsed in deionized water immediately following BCP. After rinsing, the samples were air dried and material removal was confirmed by weight loss. Then all samples were further chemically polished in fresh BCP solution to remove an additional 20 μm , rinsed, dried and confirmed by weight loss, as well.

4.2.2. Surface Orientation

The local crystallographic orientation of the polycrystalline niobium surface was investigated by electron backscatter diffraction (EBSD). Experimentally EBSD is conducted using a scanning electron microscope (SEM) equipped with a backscatter diffraction camera. Briefly, the electron beam is positioned at a particular point and a diffraction pattern (also called a channeling pattern) is collected and indexed. Repeating the process raster-fashion across a field produces an orientation map [24].

The advantages for using this technique are not only the micron-scale lateral resolution of EBSD, which reveals the orientation of individual grains in the niobium surface, but also the probing depth of this technique is about the same as the penetration depth of the RF field. The data were collected at EDAX/TSL using an OIM4 EBSD system mounted on a FEI XL-30 field emission scanning electron

microscope and analyzed using the Delphi2 software. A 1.5 x 1.5 mm field was examined in each case.

4.2.3. Surface Profilometry

Surface topography was characterized by stylus profilometry and by atomic force microscopy (AFM), the stylus profilometry was done with a Veeco Dektak 3ST profilometer, using a 2.5 μm stylus with 30 mg stylus force in “hill and valley” profile mode. For each sample, at least four 2 X 2 mm fields were scanned at medium speed and medium resolution along three parallel lines separated by 0.5 mm, rotated 90° and scanned similarly again. A Digital Instruments Nanoscope IV AFM was used in intermittent contact mode (“tapping mode”). We measured a series of 20 $\mu\text{m} \times 20 \mu\text{m}$ square fields with 0.5 Hz scan rate.

4.2.4. Laboratory X-ray Photoelectron Spectroscopy

Samples for laboratory XPS analysis were rinsed with isopropanol (Fisher, HPLC grade) prior to insertion. The analyses were carried out with a VG ESCA Lab II system, using an Mg anode (1253.6 eV) operated at 10 kV and 200 W. The electron energy analyzer operates in the constant energy mode with pass energy of 50 eV for low resolution survey scans and of 20 eV for high resolution scans. The acceptance angle is +/- 7° for XPS measurement. The energy resolution of the system was ~ 1 eV at the C1s peak. A 16 eV wide energy region for Nb 3d was scanned by a step size 0.1 eV with dwell time 500 ms at a 0° take off angle relative to the surface normal; this was repeated 20 times and summed to optimize the signal/noise ratio.

4.2.5. Synchrotron X-ray Photoelectron Spectroscopy

Synchrotron X-ray Photoelectron Spectroscopy experiments reported here were undertaken on the soft x-ray undulator beamline X1B at National Synchrotron Light Source (NSLS) at Brookhaven National Laboratory (BNL). This beamline is equipped with a spherical grating monochromator and focusing mirrors to attain a spot size of about $100\ \mu\text{m} \times 30\ \mu\text{m}$. The location of the illuminated area remains constant as photon energy is changed. The photon energy ranges from $100\ \text{eV}$ to $1600\ \text{eV}$; attainable energy resolution can be less than $0.1\ \text{eV}$. Samples were freshly rinsed with reagent-grade isopropanol, introduced to the beamline vacuum chamber and pumped to a base pressure below 10^{-10} Torr [25].

4.3. Results and Discussion

Figure 4.2 presents an optical image of the niobium surface after static BCP polishing treatment as a context for the later results. Important features to notice are: grain boundaries are significantly attacked, surfaces of individual grains appear undulating rather than faceted, and the microstructure is duplex (two different groups of grain sizes), the larger size being less than $200\ \mu\text{m}$.

4.3.1. Surface Orientation

A useful point of view is to examine the orientation of structurally significant directions for a large number of grains. Figure 4.3 presents pole figures [100], [110] and [111] directions; the assignment of rolling directions (RD, TD) is arbitrary,

since the material is believed to have been extensively cross-rolled. Evidently the dominant surface normal direction is [100]. However, the absence of large facets in the optical image does not support the notion that the ultimate surface-exposed planes have this orientation.

More detail is evident in the grain orientation map shown in Figure 4.4, which displays the orientation of each individual grain in the field relative to the inset stereographic triangle. While many grains are at or near [100], a significant number of others are not. There appears to be some extent of lines of similarly oriented grains from lower left to upper right, but more extensive data are needed. Whether any anisotropy of properties might result is yet to be studied.

AFM results from 20 x 20 μm fields within individual grains did not detect flat facets. The fields always showed general curvature and average roughness exceeding 100 nm, consistent with the optical image. Despite the [100] orientation indicated by the pole figures, the surfaces are thus not properly viewed simply as [100] planes; further study is needed.

4.3.2 Reproducibility of Topography and Surface Chemistry

Results

Many studies devoted to the BCP-treated *Nb* surface have been reported, but inconsistent results were observed, even though nominally the same measurements were used [2, 4-20]. In order to find out if this variability resulted from the technique used or the sample preparation or both, reproducibility studies were first carried out

for surface topography and composition on more than 40 samples treated and measured with the same experimental conditions.

Reproducibility studies have been carried out for two metal batches, samples within a batch, and positions within a sample. For batch-to-batch studies, seven samples each were cut from sheet seven (RRR~452) and from sheet eleven (RRR~347). For sample-to-sample studies, thirty Nb button samples were cut from the same sheet (#7). For position-to-position studies, two larger size (30mm×30mm) square samples were cut from sheet seven. All samples were chemically etched by BCP 1:1:2 at room temperature without stirring, with one exception. That sample was etched with stirring to achieve a flow rate of 1.0 inches/sec and used for position-to-position reproducibility studies. For each sample, the surface topography of four different 2x2 mm fields was determined by stylus profilometry and the roughness was quantified as the arithmetic average (R_a) of the vertical displacement from the mean. Measuring surface roughness for all samples gave an average R_a value of 1.66 ± 0.55 (standard deviation) for sheet seven and 1.61 ± 0.48 (standard deviation) for sheet eleven. Evidently the roughness is significantly variable, but is well-characterized by the average value of R_a of seven samples. The difference between batch averages was only a tenth of the variation within batches. However, all values exceed the few-nm escape depth of photoelectrons in XPS, so that the effectiveness of angle-resolved XPS for investigation of how composition varies with depth must be questioned [20, 26-30].

The characterization of the surface chemistry focused on the *Nb3d* region (see Figure 4.5). The prominent features correspond to Nb^{5+} and the spectra are discussed in terms of the intensity ratio of Nb^{5+} / Nb^{total} . Data acquired for all static samples gave average values of 0.64 +/- 0.026 (standard deviation) for sheet # 7 and 0.61 ± 0.018 (standard deviation) for sheet # 11. The variation for the intensity ratio at different positions within a sample is much smaller than sample-to-sample: the static solution sample-0.65 ± 0.005; the flowing solution sample-0.68 ± 0.007. These results suggest that it is reasonable to think that ratio differences greater than 0.05 (twice the largest standard deviation) may viewed as significant.

4.3.3. Effect of Solution Flow Rate.

In cavity processing, solution flows in one end and out the other. As noted earlier, the maximum flow rate occurs in the narrow “iris”, about 1.3 inches /sec for CEBAF cavities. Different surface chemistry and topography may result at different locations with whatever consequence might follow for SRF performance. Six different flow rates have been studied: 0 (static), 0.65 inches/sec, 1.0 inches/sec, 1.3 inches/sec, 1.65 inches/sec and 1.95 inches/sec. For each flow rate, seven samples were treated together at the same time in the “Teflon” plate fixture and then measured.

Figure 4.6 displays the effect of flow rate on the surface roughness; error bars correspond to one standard deviation. No significant effect on surface roughness at the different flow rate can be observed. Figure 4.7 compares the *Nb3d* manifold for samples etched at zero (“static”) and 1.0 inches/sec flow rate by using the synchrotron

based XPS (detailed information about the niobium surface chemistry studies by using synchrotron based XPS has been introduced in chapter 3). The systematic effect of solution surface speed on Nb^{5+} / Nb^{total} for the whole set obtained with the lab XPS is depicted in Figure 4.8; again the error bars indicate one standard deviation. In both, a significant effect on surface chemistry at the different flow rate can be observed, which is much larger than the difference associated with sample-to-sample variation. Based on the variable photon energy results, it may be inferred that the variation in ratio represents the variation in Nb_2O_5 layer thickness.

A simple model may help interpret the variation of Nb speciation with solution flow rate. Consider a Nb_2O_5 layer of thickness “ t ” on a Nb metal slab. The Nb metal signal intensity is that of Nb metal attenuated by passage through the oxide layer. The signal from the oxide layer is the difference between the intensity from an oxide slab and the signal from an oxide slab attenuated by passage through the layer:

$$I(Nb^0) = e^{-t/\lambda} I(Nb^0, slab) \quad 4-9$$

$$I(Nb^{5+}) = (1 - e^{-t/\lambda}) I(Nb^{5+}, slab) \quad 4-10$$

where λ is the attenuation length in the oxide layer. For a given thickness, the ratio of these intensities is:

$$R(t) = (e^{-t/\lambda} - 1) \frac{I(Nb^{5+}, slab)}{I(Nb^0, slab)} \quad 4-11$$

For the ratio of two thicknesses, the slab intensities cancel. Expressing the thickness for a flowing solution $t(f)$ in terms of the ratio a_f to the thickness under static conditions ($a_f \frac{t(s)}{\lambda}$) gives,

$$\frac{R(f)}{R(s)} = \frac{\{\exp[a_f \frac{t(s)}{\lambda}] - 1\}}{\{\exp[\frac{t(s)}{\lambda}] - 1\}} \quad 4-12$$

The variable photon energy measurements earlier indicate that $t(s)$ is between 3 and 4.4 nm and λ for the oxide was calculated as 2.9 nm for 1254 eV photons. Substituting the *Nb* species ratios for the 1.3 inch/sec flow rate gives estimated thickness ratios to static samples of 1.3 to 1.4. Actual thicknesses are thus estimated to lie between 3.9 nm and 6.2 nm. The attenuation length for 930 eV photons was calculated as 2.17 nm for Nb_2O_5 through TPP-2M equation [31-34], making the information depth (3λ) about 6.5 nm. The smallness of the *Nb* metal signal in the spectrum (Figure 4.8) suggests that the actual oxide layer thickness is toward the higher end of the range.

4.4. Conclusions

Polycrystalline *Nb* surfaces etched at different chemical solution flow rates have been studied morphologically and chemically by using electron backscatter diffraction, stylus profilometry, atomic force microscopy, and laboratory XPS and Synchrotron XPS. While EBSD indicates that the post-etching surface orientation is (100), no support is found for the notion that the exposed surface planes can be

simply described as (100) facets. The variability of roughness data (Ra) was about $\pm 30\%$, while that of surface chemistry (Nb^{5+} / Nb^{total}) was about $\pm 5\%$. The BCP surface treatment results in micron-scale (vertical) surface roughness, and the magnitude is insensitive to treatment details within our parameters range. At room temperature, increased BCP etchant flow rate over the range expected for SRF cavity processing results in an approximately 40% increase in the thickness of the Nb_2O_5 surface layer compared to static conditions.

4.5. References

1. H. Padamsee, J. Knobloch, and T. Hays, "*RF Superconductivity for Accelerators*", Wiley, New York, (1998).
2. R. Ballantini, and R. Parodi, "*Proceeding of the Ninth Workshop on RF Superconductivity*", Sante Fe, NM (1999), pp. 211.
3. P. Kneisel, "*Proceeding of the Ninth Workshop on RF Superconductivity*", Sante Fe, NM (1999), pp. 328.
4. Q. Ma, and R. A. Rosenberg, *Appl. Surf. Sci.* 206(1-4) (2003) pp. 209.
5. Q. Ma, and R.A. Rosenberg, "*Proceedings of the 2001 Particle Accelerator Conference*", Piscataway, NJ. 2 (2001), pp.1050
6. J. Halbritter, and A. Darlinski, *IEEE Transactions on Magnetics*. MAG-23(2)(1987), pp.1381.
7. A. Dacca, and J. Halbritter, *Appl. Surf. Sci.*, 126(3-4) (1998), pp. 219.
8. A, Darlinski, and J. Halbritter, *Surf. Interf. Anal.*, 10(5) (1987), pp. 223.
9. J. Halbritter, *IEEE Transactions on Magnetics*, MAG-21(2) (1985), pp.858.
10. J. Halbritter, *J. the Less-Common Metals*, 139(1) (1988), pp. 133.
11. J. Halbritter, *Surf. Interf. Anal.*, 12(1-12) (1988), pp. 354.
12. J. Halbritter, *Appl. Phys. A- Solids & Surfaces*, A 43(1) (1987), pp. 1.
13. J. Halbritter, *Solid State Communications*, 34(8) (1980), pp. 675.
14. M. Grundner, and J. Halbritter, *J. Appl. Phys.*, 51(1) (1980), pp. 397.
15. A. Darlinski, and J. Halbritter. *J. Vac. Sci. Technolog. A*. 5(4) (1987), pp.1235.

16. A. Dacca, and J. Halbritter , Surf. Sci. Spec., **5**(4) (1998), pp. 332.
17. C. Z. Antoine, "*Proceeding of the Ninth Workshop on RF Superconductivity*", Sante Fe, NM, (1999), pp.109.
18. C. Z. Antoine, "*Proceeding of the Ninth Workshop on RF Superconductivity*", Sante Fe, NM, (1999), pp.295.
19. C. Z. Antoine, J. Appl. Phys. **81**(4) (1997), pp. 1677.
20. Q. Ma, and R.A. Rosenberg, J. Appl. Phys., **96**(2004), pp. 7675.
21. J. Halbritter, Electro. Acta., **34**(8) (1989), pp. 1153.
22. H. Padamsee, Superconductor Science & Technology, **14**(4) (2001), pp. 28.
23. T. Wang, C. Reece, and R. M. Sundelin, J. Vac. Sci. Technol. B, **21**(4) (2003), pp.1230.
24. Adam J. Schwartz, Mukul Kumar, and Brent Adams, "*Electron Backscatter Diffraction in Materials Science*", Kluwer Academic/Plenum, 2000
25. H. Tian, C. Reece, and M. Kelley, "*Proceedings of the 11th Workshop on RF Superconductivity*", DESY, Germany (2003).
26. W. H .Gries, Surf. Interf. Anal., **24** (1996), pp. 38.
27. P.L.J.Gunter, Appl. Surf. Sci., **89** (1995), pp. 69.
28. P.L.J.Gunter, Appl. Surf. Sci., **105**(1997), pp. 342.
29. P.L.J.Gunter, J. Vac. Sci. Technol., A, **13**(3) (1995), pp. 1290.
30. P. H. Holloway, Surf. Interf. Anal., **18** ((1992), pp. 251.
31. S. Tanuma, C.J. Powell, and D.R. Penn, Surf. Sci., **192**(1) (1987), pp. L849
32. M. P. Seah, and W.A. Dench. Surf. Interf. Anal., **1**(1979), pp. 2.

33. S. Tanuma, C.J. Powell, and D.R. Penn, *Surf. Interf. Anal.*, 17(1991), pp. 927.

34. W. H. Gries, *Surf. Interf. Anal.* 24(1996), pp. 38

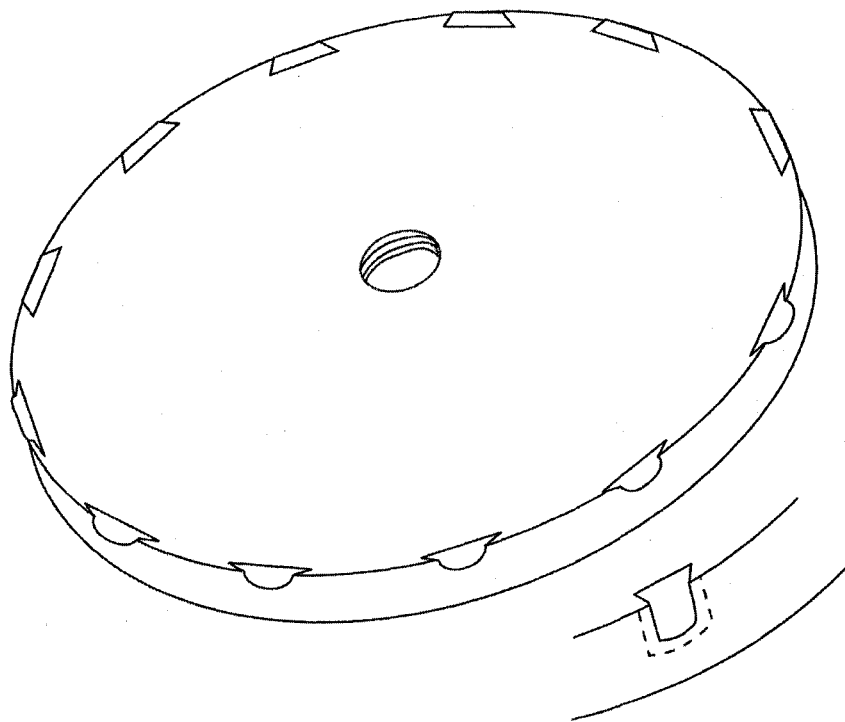


Figure 4.1: The rotating "Teflon" fixture to provide constant surface flow rate etching for multiple specimens

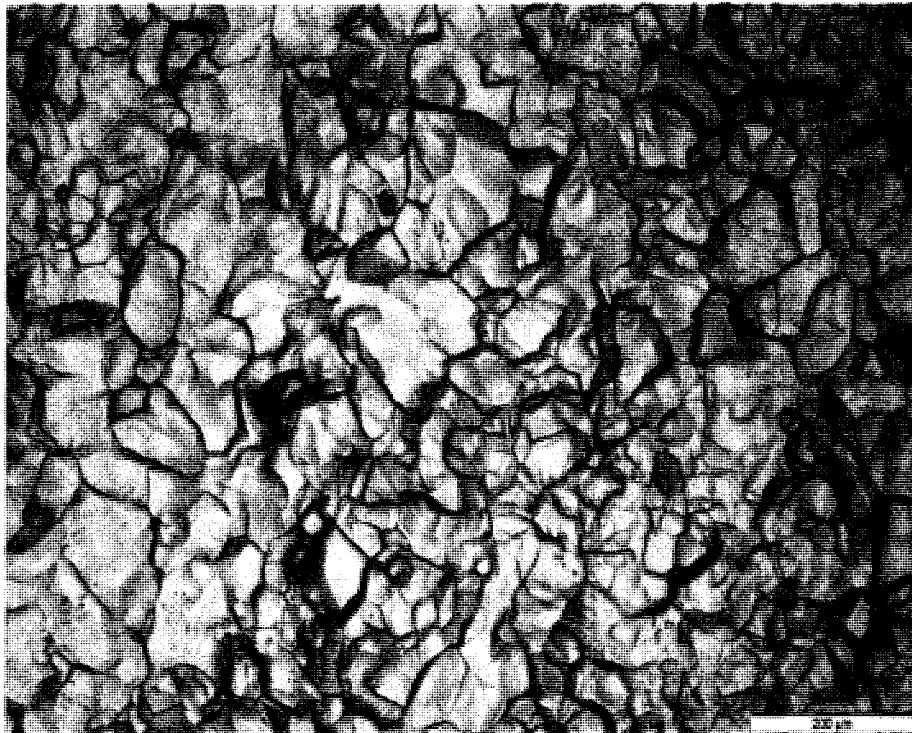


Figure 4.2: Optical image of the niobium surface after static BCP etch. Bar in the lower right represents 200 μm . (Optical microscopy was taken by Institute of Laser Technology, Aachen, Germany)

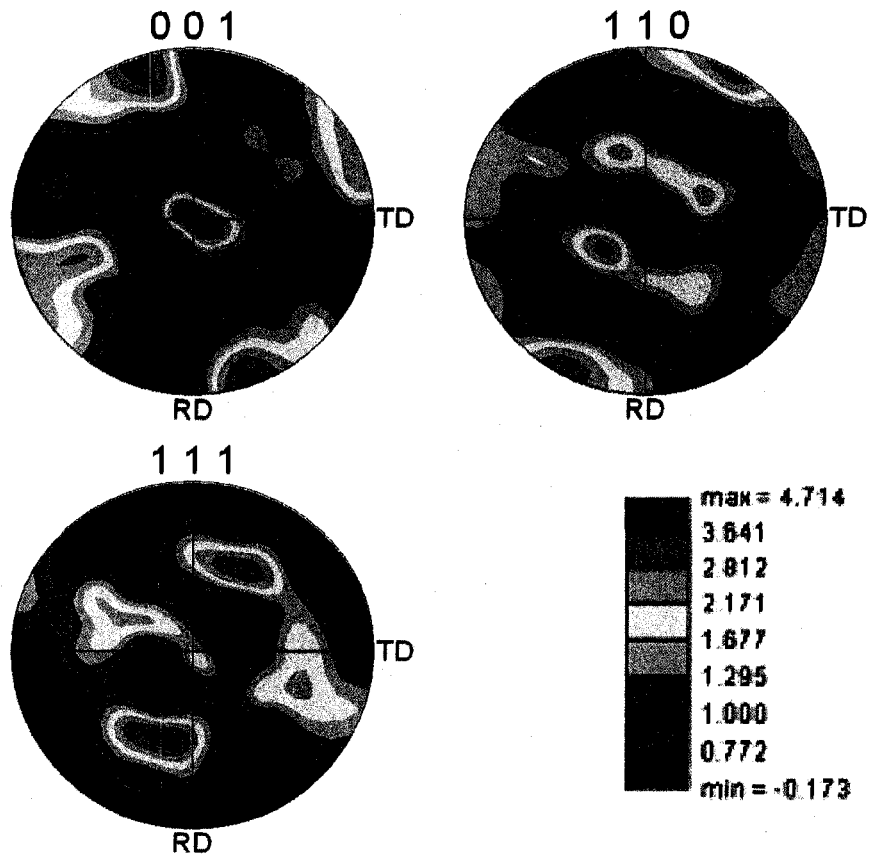


Figure 4.3: Pole figures obtained by EBSD from a 1.5 x 1.5 mm field after static BCP etching (The sample normal direction is located in the center of the pole figures. The RD and TD direction are arbitrary in this case. The scale value on the bar is in the units of times random)

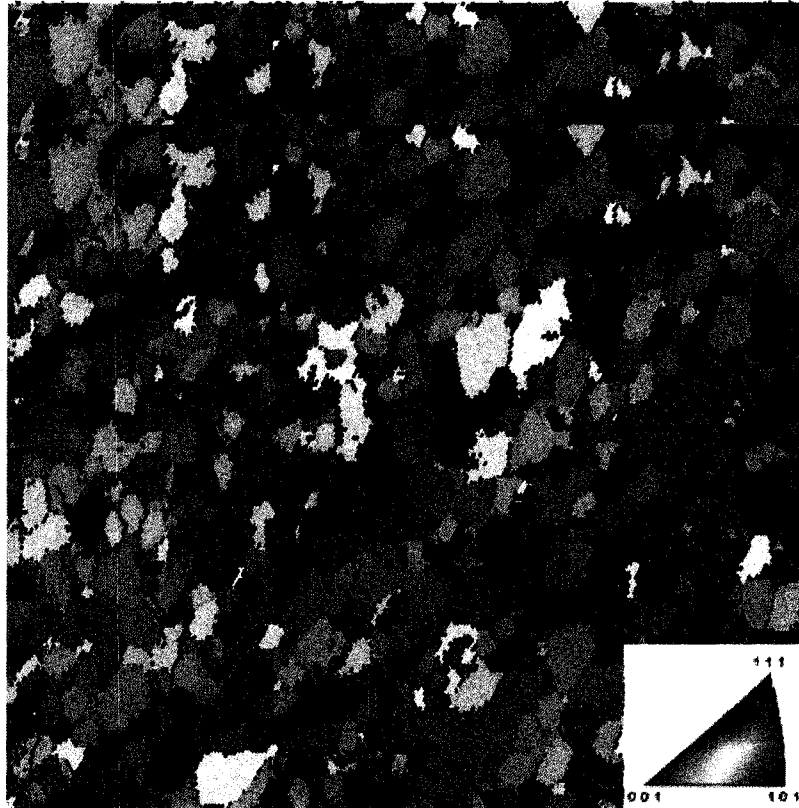


Figure 4.4: Map of grain orientations after static BCP etching from the same field as Figure 3.3. The grain maps show grains randomly colored to the highlight size and shape

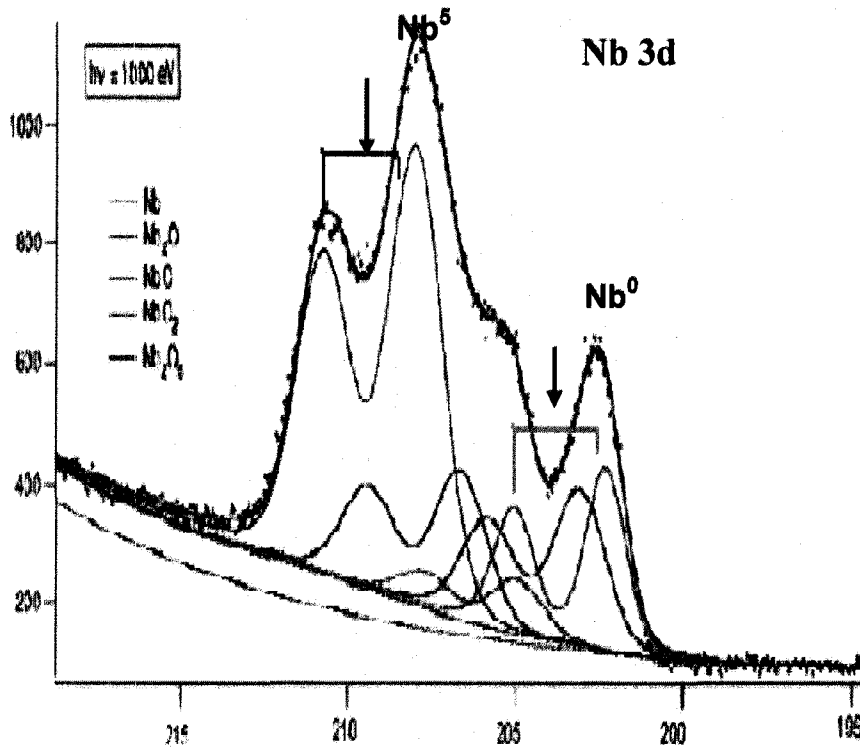


Figure 4.5: Components of Nb 3d manifold (The dot indicate the collected spectrum. The full line-black, indicates the simulation. The components of Nb 3d are: pink: Nb_2O_5 ; blue: NbO_2 ; light blue: NbO ; green: Nb_2O ; dark yellow: Nb), adapted from From H. Tian, C. Reece, and M. Kelley, *Proceedings of the 11th Workshop on RF Superconductivity* 2003. Reprint with permission of DESY, Germany)

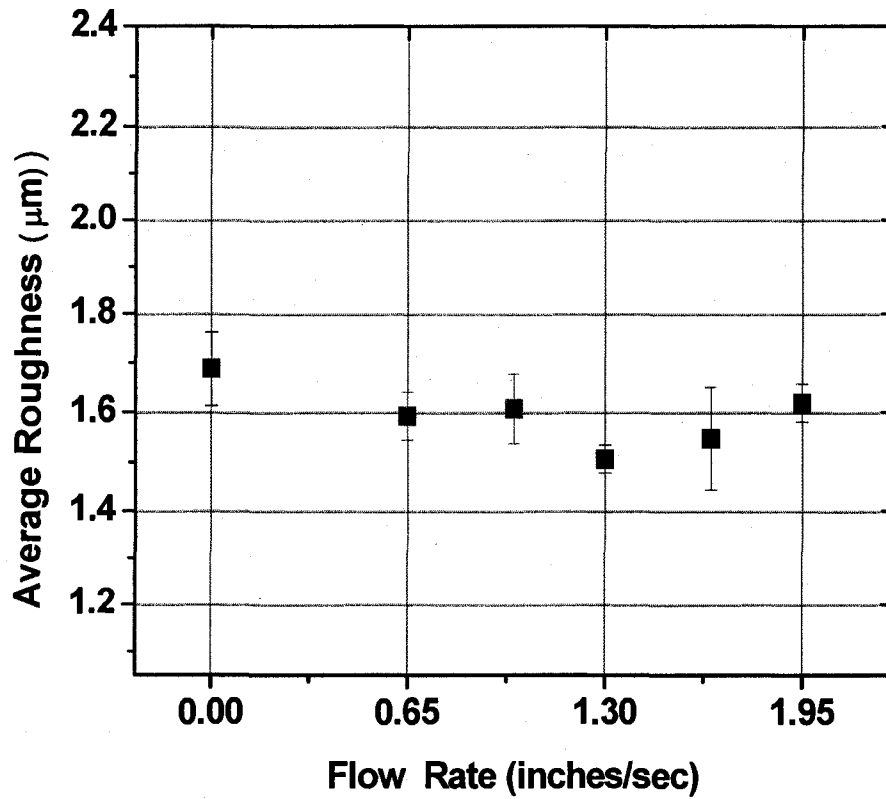


Figure 4.6: The effect of flow rate on the surface roughness (RMS: μm), error bars correspond to one standard deviation. No significant effect on surface roughness at the different flow rate can be observed.

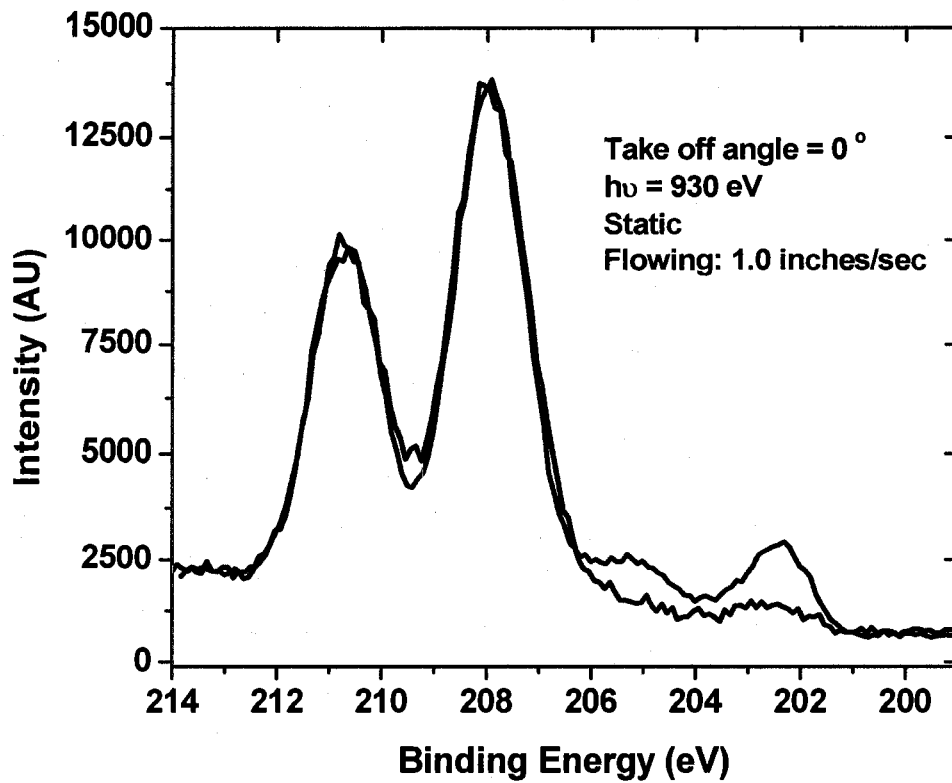


Figure 4.7: Comparison of Nb 3d region photoelectron spectra of static (red) vs. flowing BCP etching (blue) polycrystalline Nb (They were collected 0° takeoff angle relative to surface normal by using 930eV photon energy-X1B beamline, NSLS, BNL)

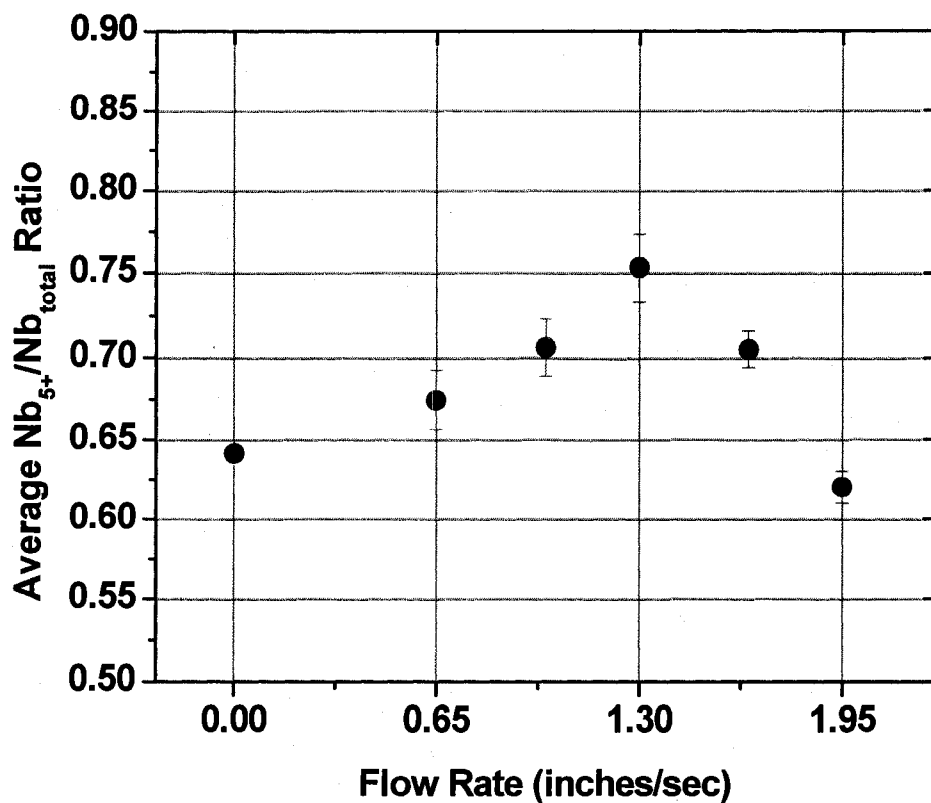


Figure 4.8: The effect of flow rate on the surface chemistry ($I^{Nb_{5+}} / I^{Nb_{Total}}$). A significant effect on surface chemistry at the different flow rate can be observed, which is much larger than the difference associated with sample-to-sample variation.

CHAPTER 5

Novel Characterization of the Electropolishing of Nb with a Hydrofluoric and Sulfuric Acid Electrolyte*

5.1. Introduction

Electropolishing is a surface finishing process based on anodic dissolution of a metal or alloy in an appropriately chosen electrolyte [1]. The history of electropolishing goes back to the beginning of the past century [2-4], but the first systematic investigations leading to practical application are due to Jacquet [5]. The electropolishing phenomenon is characterized by the elimination of micro-roughness (leveling) and the absence of crystallographic and grain boundary attack (brightening) and results in the production of smooth, bright surfaces [6-7]. Leveling results from the fact that protruding parts of a rough surface dissolve faster than recessed parts.

* This chapter has been submitted to the Journal of the Electrochemical Society

This can be achieved under either ohmic or mass transport control [8]. Brightening can only occur under mass transport control, which suppresses crystallographic etching [6, 8-10].

The typical EP process now applied to niobium cavities was inherited from Siemens Company in the 1970's [11] and was further developed by KEK in collaboration with Namura Plating [12]. In recent years, researchers at KEK in Japan have discovered improved SRF cavity performance by electropolishing over BCP, i.e. higher acceleration gradient is achieved on cavities [12]. Several other institutions have since formed collaboration with KEK to investigate the process and have confirmed the discovery with similar results [13]. Typically, a mixture of hydrofluoric (49%) and sulfuric acid (95~98 %) of volume ratio of 1 : 9 was used with a temperature range of 30 °C ~ 40 ° C, and a current density 30 ~ 100 mA/cm² with applied total cell voltage of 12~25 volts[13]. Surface area ratio of niobium cavity (anode) to high purity aluminum tube (cathode) of 10: 1 was used during practical cavity EP processing.

Previous cavity EP studies have shown that the best polishing condition occurs in the current-limited plateau of the polarization curves. Parameters such as electrolyte temperature, acid concentrations, viscosity and stirring have strong effects on the EP process [4]. Some studies conducted on either small samples or half cells tried to evaluate the influence of each parameter [14-15]. However, the application of electrochemical techniques is needed for the development of a clear picture of the exact role of each parameter involved during the EP process. Microscopic

understanding of the basic Nb EP mechanism is expected to provide an appropriate foundation with which to optimize the preparation of high-field niobium cavity surfaces.

In this study, we determine the separation of the power supply voltage into three components: (1) applied potential at the anode-Nb, (2) applied potential at the cathode-Al, and (3) potential drop in the electrolyte. These results are used to reveal the area ratio of anode and cathode, local effects of the temperature, solution concentration and flow condition on the mass-transport current-limited plateau during niobium electropolishing. The electrochemical impedance of the Nb EP process has been measured as a function of potential and flow rate and the mechanism of Nb electropolishing with hydrofluoric and sulfuric acid electrolyte is identified.

5.2. Electropolishing Fundamentals

5.2.1. Electrochemical Cell of Niobium Electropolishing

The electrochemical cell and data acquisition scheme for niobium electropolishing in hydrofluoric sulfuric acid electrolyte is illustrated in Figure 5.1. The redox processes during electropolishing are driven by an external power supply. The niobium electrode connected to the positive pole of the power supply is called the anode and set as a working electrode (WE) in this study. The aluminum electrode connected to the negative pole of the power supply is called the cathode and works as a counter electrode (CE). The corresponding voltage drop across the Nb and Al electrodes was determined with a parallel circuit using a reference electrode. Under

the electrical field, the positive ions (cations) move toward the cathode and the negative ions (anions) move toward the anode. The cations get electrons and are reduced to atoms at the cathode surface. Therefore, electron transfer between the two electrodes is carried out via the ion drift in the electrolyte and electron conduction in the metal wire [16].

5.2.2. Electrical Double Layer

The electrode-electrolyte interface has been shown to behave like a capacitor because of the electrical double layer formed as ions from the solution “stick on” the electrode surface [26]. It was introduced in the 1850's by Helmholtz and later modified by Gouy, Chapman and Stern [20-21]. This model assumed that no electron transfer reactions occur at the electrode and the solution is composed only of electrolyte. The interactions between the ions in the electrolyte and the electrode surface were assumed to be electrostatic in nature and resulted from the fact that the electrode holds a charge density which arises from either an excess or deficiency of electrons at the electrode surface. In order for the interface to remain neutral, the charge held on the electrode is balanced by the redistribution of ions close to the electrode surface. In the solution, water molecules, positive and negative ions drift around. The adsorbed layer of positive metal ions attracts nearby water dipoles in a preferential direction, which move toward the metal surface. This forms the first layer (hydration sheath), called the inner Helmholtz layer; while it is occupied largely by water dipoles, some negative ions can also be found in this layer. These adsorbed ions are said to be specifically adsorbed [16, 21]. The locus of the electrical centers of the

specifically adsorbed ions is called the inner Helmholtz plane (IHP, at X_1 as illustrated in Figure 6.2). Solvated ions can approach the metal only to a distance X_2 , the locus centers of these nearest solvates ions is called the outer Helmholtz plane (OHP) [16, 21]. The interaction of solvated ions with the charged metal surface involves only long-range electrostatic force, so that their interaction is essentially independent of the chemical properties of the ions. These ions are said to be nonspecifically adsorbed. Because of thermal agitation in solution, the nonspecifically adsorbed ions are distributed in a three dimensional region called the diffuse layer, which extends from OHP to the bulk of the solution. The double layer structure may significantly affect the electrode process [20-21]. The value of the double layer capacitance depends on the electrolyte composition, temperature, oxide layer, electrode roughness as well as the applied potential [20-21].

5.2.3. Anode Polarization Curve of Niobium Electropolishing

In the past few decades, cavity EP process empirically demonstrated that the best polishing condition occurred in the limited-current plateau of the polarization curves [5, 12-15]. Therefore, a practical search for optimum experimental conditions is best started with a determination of current-potential (I-V) curves under controlled mass transport conditions. The curve 1 in Figure 5.3 is a typical anode polarization curve for Nb electropolishing in a 1: 9 mixture of hydrofluoric and sulfuric acid.

In the AB region, the anode potential is relatively low, and the electrochemical process kinetics is dominant. The current, i is linearly proportional to electrode potential as described by the well known Butler-Volmer equation [21].

$$i = i_0 \left[\frac{C_{ox}(0,t)}{C_{ox}} e^{-\alpha f \eta} - \frac{C_{re}(0,t)}{C_{re}} e^{(1-\alpha) f \eta} \right] \quad 5-1$$

with $i_0 = FAK^0 C_{ox}^{(1-\alpha)} C_{re}^\alpha$, i_0 : the equilibrium current, and $f = \frac{F}{RT}$, where C_{ox} and C_{re} are bulk concentrations, $C_{ox}(0,t)$ and $C_{re}(0,t)$ are the concentration of ox and re at the electrode /electrolyte interface at time t, $F = 9.64853 \times 10^4 C$ is Faraday constant, α ($= 0 \sim 1$) is transfer coefficient, A is the surface area of the electrode, K^0 is standard rate constant, $R = 8.317 J mol^{-1} K^{-1}$ is the gas constant, and η is the over potential given by the Tafel equation.

$$\eta = E - E^0 = a + b \log i \quad 5-2$$

where E is the electrode potential and E^0 is the standard redox potential at which the interface is at equilibrium with a electrolyte (i.e, $C_{ox} = C_{re}$); a and b are constants.

Equation 5-2 gives a quantitative relation between current and overpotential. It reflects the dynamics of electrode reaction when the interfacial electrochemical reaction process is dominant and may be approximated to [17]

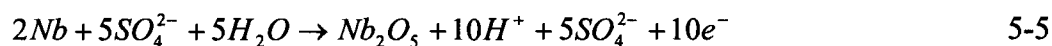
$$i = \frac{\eta}{R_p} \quad 5-3$$

with $R_p = \frac{RT}{nFi_0}$, R_p is termed as polarization resistance.

In this region, hydrogen formation may occur at the aluminum cathode [12, 14],



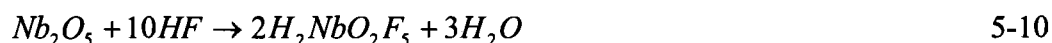
and oxidation may occur at the niobium anode[12, 14].



For an easier understanding, the oxido-reduction equation might be written:



In presence of *HF*, Nb_2O_5 might be then dissolved to soluble niobium fluoride, oxofluoride through following reactions [14]:



In this region, from the equation 5-3, we know that current increase with increasing overpotential $\eta = E - E^0$. Therefore, for a certain applied potential, the sites on the metal surface, such as defects and grain boundary, having different standard redox potential E^0 [21], different current (dissolution rate) will result. Such an anodic dissolution will not lead to polishing. Instead, crystallographic etching occurs

In the BC region of the polarization curves, current-potential deviates from linear relationship. As the potential continues to increase, the increase of the current slows down until it reaches a maximum and then decreases to a minimum point, and finally increases to the limiting current region. This is a transition from kinetics of charge

transfer/chemical reaction domain to mass transport domain. The oscillations are very likely related to the formation and breakdown of the anode film [22-23].

In the CD region of the polarization curve, the applied potential of the anode electrode is increased above a certain value; the equations 5-1 and 5-3 are no longer valid since the reaction rate is so high and the system becomes mass transport controlled. In this region, niobium ions (Nb^{5+}) would be kinetically produced on niobium anode faster than mass transport process can remove from the anode surface into the bulk solution.

Mass transport limitation for anodic dissolution is generally believed to be responsible for electropolishing and this view is supported by the observation in numerous experimental systems of polishing for anodic dissolution along a limiting current plateau [22-27]. Mass transport might occur by three mechanisms in an electrochemical cell [20].

(1) Migration, movement of ions driven by a gradient of electrical potential

$$\left(\frac{\partial\phi(x)}{\partial x}\right)$$

(2) Diffusion, movement of species (ions, molecules) driven by a gradient of chemical potential (i.e. a concentration gradient $\frac{\partial C_i(x)}{\partial x}$); and

(3) Convection, natural convection driven by density gradient and forced convection (stirring, vibration)

It is described by the Nernst-Planck equation [21], written for one-dimensional mass transfer along the x-axis as

$$J_i(x) = -D_i \frac{\partial C_i(x)}{\partial x} - \frac{z_i F}{RT} D_i C_i \frac{\partial \phi(x)}{\partial x} + C_i v(x) \quad 5-12$$

where $J_i(x)$ is the flux of species i ($\text{mol s}^{-1} \text{cm}^{-2}$) at distance x from the surface, D_i is the diffusion coefficient (cm^2 / s), $\frac{\partial C_i(x)}{\partial x}$ is the concentration gradient at distance x , $\frac{\partial \phi(x)}{\partial x}$ is the potential gradient, C_i and z_i are the concentration (mol cm^{-3}) and charge (dimensionless) of species i , respectively, and $v(x)$ is the velocity (cm / s) with which a volume element in solution moves along the axis.

In bulk solution (away from electrode), concentration gradient, $\frac{\partial C_i(x)}{\partial x}$ is generally small and the total current is mainly carried by migration. In a real electrochemical system of electropolishing, convection is usually introduced by methods such as stirring or other forced circulation strategies. In such a system, the velocity of solution flow is generally a constant in the bulk solution (far from the electrode surface) and decreases while approaching the solid surfaces due to the friction between the fluid and surface. Otherwise, for a static condition, as most of experiments of this study are conducted, convection is neglected.

In DE range of the polarization curve, current increases again almost linearly with increasing potential. This is likely due to the occurrence of reactions such as [14]



in addition to anode dissolution and hydrogen formation. All reactions contribute to charge transfer and therefore to increasing current, OH^- ions tend to move to anode,

O₂ is produced on the anode surface. These gas (oxygen or hydrogen) bubbles may block niobium ion transport, terminating the electrochemical dissolution process on the area inside the bubble. However, the residual solution on the surface area inside the bubbles may react with the anode, resulting chemical etching [8]. Depending on the chemical properties of the electrolyte solution and the value of current density at which the electrochemical dissolution is occurring, the etching speed can be higher than the rate of electrochemical dissolution. In this case, pits will be produced on the anode surface. In contrast, if etching does not occur inside the bubbles or if its speed is slower than that of electrochemical dissolution process, the area inside the bubbles will remain and appear as a protruding particle after the electrochemical process. In either case, a rough surface is produced [8].

5.2.4. Electrochemical Impedance Spectroscopy (EIS)

Traditional electrochemical measurements provide only current made of faradic and non-faradic components. Through them alone, the electrochemical reactions at the electrode-electrolyte interface cannot be fully understood [28]. A complete description requires impedance measurements made over a wide range of frequencies at various potentials and determination of all the electrical characteristics of the interface. Electrochemical impedance spectroscopy (EIS) is a method in which a small variable ac signal is applied to on top of a controlled dc potential the electrode, impedance as a function of frequency is recorded and used to characterize the electrode-electrolyte interface and electrochemical processes [29-30]. Typically, the cell elements and cell characteristics, including electrode double layer capacitance,

electrode kinetics, diffusion layer and solution resistance, contribute to the system's EIS spectrum [27].

The ac sinusoidal modulation usually used in EIS has a time-variant magnitude $V(t)$ given by

$$V(t) = V_0 \sin(\omega t) \quad 5-14$$

where angular frequency $\omega = 2\pi f$.

The most common method used to analyze EIS spectra is equivalent circuit modeling. In a simple case, the interface of electrode-electrolyte can be modeled as a circuit [19], made of a double layer capacitor (C_{dl}) in parallel with a polarization resistor (R_p) and a Warburg resistor (R_w) to model diffusion effect. When the above signal is applied, the resulting current flowing is

$$\begin{aligned} I(t) &= \frac{V}{R_1} + C \frac{dV}{dt} \\ &= \frac{V_0}{R_1} \sin(\omega t) + V_0 \omega C \cos(\omega t) \end{aligned} \quad 5-15$$

where $R_1 = R_p + R_w$.

Assuming $V_0 / R_1 = I_0 \cos(\phi)$ and $V_0 \omega C = I_0 \sin(\phi)$, then equation 5-15 can be written as

$$I(t) = I_0 [\sin(\omega t) \cos(\phi) + \cos(\omega t) \sin(\phi)] \quad 5-16$$

This indicates that the resulting current is a sine wave with same angular frequency (ω) as the applied voltage but shifted by an angle-phase angle (ϕ). The overall impedance Z is a function of frequency (ω) and is given as

$$\frac{1}{Z} = \frac{1}{Z_{R_1}} + \frac{1}{Z_C} \quad 5-17$$

Substituting $Z_{R_1} = R_1$ and $Z_C = 1/j\omega C$ into the this equation, gives

$$Z = \frac{R_1}{1 + \omega^2 C^2 R_1^2} - j \frac{\omega C R_1^2}{1 + \omega^2 C^2 R_1^2} = Z' + jZ'' \quad 5-18$$

where Z' and Z'' are the real and imaginary parts, typically depicted in a Nyquist plot [29-30].

Two limiting cases for this circuit are easily recognized [30],

1. When $\omega \rightarrow \infty$, $Z \rightarrow Z'' = -j/\omega C$, the Z'' is small and Z is determined by the C , which provides the main ac current pathway.
2. When $\omega \rightarrow 0$, $Z'' \rightarrow \infty$, so the only (then dc) current pathway is through R and $Z \rightarrow Z' = R$

In most systems of practical significance, an additional series resistance, R_s , representing the ohmic resistance of the solution and separator and any internal resistance of the electrode material must be included [30]. The equivalent circuit is displayed in Figure 6.12b and the overall impedance Z is given by

$$Z = \frac{R_1}{1 + \omega^2 C^2 R_1^2} + R_2 - j \frac{\omega C R_1^2}{1 + \omega^2 C^2 R_1^2} \quad 5-19$$

$$\text{where } Z' = \frac{R_1}{1 + \omega^2 C^2 R_1^2} + R_2, \text{ and } Z'' = \frac{-\omega C R_1^2}{1 + \omega^2 C^2 R_1^2}.$$

Out of convention, since Z'' is almost always capacitive rather than inductive, Z'' is plotted vs. Z' in the EIS Nyquist as shown in Figure 5.14a.

5.3. Experimental Procedures

The working electrode was a high purity polycrystalline Nb (99.9999%, Teledyne Wah-Chang) electrode with dimensions of 22mm x 22 mm x 4 mm embedded into a Teflon sample holder, providing an exposed surface area of 2.5 cm². The counter electrode was a high purity Al plate with a surface area fraction of either 0.1 or 2 as compared to the exposed Nb surface. The cathode-to-anode separation was 98 mm, in agreement with the typical distance between the equator of an SRF cavity and the Al counter electrode used during cavity EP process. The reference electrode was a saturated mercury mercurous sulfate electrode (MSE) placed 10 mm from the Nb sample. The electrolytes were prepared from analytic grade 49 % hydrofluoric (48.8 ~ 49.2 %, J. T. Baker) and 96 % sulfuric acid (95 ~97%, J. T. Baker). In order to protect the reference electrode from HF contamination, the reference electrode was placed in an electrode bridge tube with a Vycor frit. The electrode bridge tube was filled with 1 M H₂SO₄ as the conductive electrolyte.

The polarization curves were conducted stepwise/step size=0.25 volts, dwell time=1 second over the potential range from 0 to 22~25 volts (using a Sorensen DCS 33-33E power supply). The potential between the Nb electrode and the reference

electrode (V_{Nb}) was recorded using a Keithley 6517A electrometer. This is not the typical three electrode electrochemical cell, but rather a two electrode set-up: controlling the potential (ΔV) between the working and counter electrode. The addition of the reference electrode is for monitoring the potentials on the cathode and anode independently. This set-up was chosen to reproduce the two electrode EP process used in SRF cavity production. The current was recorded with a HP 3478A multi-meter. The data acquisition system was supported by a customized LabView program. Prior to the polarization measurement, the electrodes were immersed in the electrolyte in an open circuit condition for 3 to 5 minutes.

Impedance measurements were performed using a potentiostat (Series G 300, Gamry Instruments) controlled with a commercial software package (Gamry Instrument Framework, Gamry Instruments) and the same configuration, including reference electrode as described above. Impedance measurements were performed at constant potential after 120s, the time at which a steady-state current is attained. The amplitude of potential modulation was 10 mV. Starting with 200 kHz, the modulation frequency was swept automatically down to 0.2 Hz.

5.4. Results

5.4.1. Polarization Behavior

Figure 6.3 shows the typical polarization behavior for the anode and cathode as indicated. The potential of cathode was calculated by $\Delta V - V_{Nb}$ (ΔV , the potential

between anode and cathode controlled by the power supply; V_{Nb} , the potential between Nb and the reference electrode measured by a Keithley 6517A electrometer). This value was not corrected for electrolyte resistance as discussed below. Several features are noteworthy: the cathode exhibits well-behaved polarization behavior and accounts for a significant fraction of the applied potential. However, to date the potential drop across the cathode has been ignored in typical Nb electropolishing process descriptions. The potential drop across the electrolyte is purely resistive, the effective bath resistivity was determined to be $\sim 8 \Omega\text{-cm}^2/\text{cm}$ with $T_{\text{bath}} = 32 \text{ }^\circ\text{C}$. For a typical cavity polishing condition $\Delta V = 15 \text{ V}$, the anode polarization potential corresponds to approximately 9 V, the cathode $\sim 4 \text{ V}$, and the potential drop across the electrolyte $\sim 2 \text{ V}$. These values are dependent upon the electrolyte composition, temperature, relative surface areas of cathode and anode as well as the applied potential.

5.4.2. Area Ratio of Anode and Cathode

Figure 5.4 is the schematic drawing of horizontal single cell cavity EP set-up, which was developed at KEK [12], later on modified and used among many laboratories. During the cavity EP process, the niobium cavity itself behaves as an anode, and a certain diameter of high purity Al tube was used as the cathode. The size of beam tube of the niobium SRF cavity limits the diameter of Al tube, for example, 25.4 mm for DESY horizontal EP, 33 mm for J-lab horizontal EP and 25mm for KEK horizontal EP [12-13], which usually gives about 10: 1 area ratio of anode and cathode. The over-driving of the cathode might exist considering the

limited cathode reactive area, which motivated us to conduct a detailed study of the effect of different area ratio of anode and cathode on the polarization curves. Figure 5.5a and 5.5b presents the anode polarization curves for different area ratio of niobium and aluminum. We found the anode current density was not affected by the reactive area of cathode and anode current increases with niobium reactive area but current density kept constant.

5.4.3. Effect of HF Volume Concentration

A standard Nb EP procedure consists of a 1:9 volume ratio mixture of concentrated HF (49%) to concentrated H₂SO₄ (96%). The effect of increasing the HF volume content above 1: 9 has been reported by others [14]. We explored decreasing the HF volume ratio to assess the sensitivity of the EP process to HF loss which may be expected due to evaporation and chemical reaction [14]. Figure 5.6 shows the polarization curves measured in freshly prepared electrolytes of hydrofluoric (49%) and sulfuric (96%) as a function of HF to H₂SO₄ volume ratio. The corresponding molar concentration decreases for HF and H₂O from the classical 2.8 mol/L and 6.9 mol/L (HF/H₂SO₄ volume ratio = 1:9) to 0.56 mol/L and 4.65 mol/L (HF/H₂SO₄ volume ratio = 0.02:9.8) respectively, and increases for H₂SO₄ from 16.22 mol/L to 17.66 mol/L. All anode polarization curves exhibit a limiting current plateau. The anode plateau current density fell approximately linearly with the decreasing HF/H₂SO₄ volume ratio, while the cathode polarization behavior was substantially unaffected, as shown in Figures 5.6 and 5.7. This suggests that the polishing rate is strongly affected by the composition of electrolyte as shown in Figure 6.6; the current

density changes by a factor of 5 for a factor of 5 change of HF (49 %) volume content. The understanding of the detailed role of HF involved in Nb dissolution during the EP process requires further electrochemical studies; in particular a separation of the contribution of salvation effects from F⁻ diffusion to the Nb electrode.

5.4.4. Effect of Electrolyte Temperature

Past EP studies identified that an electrolyte temperature of 25°C ~ 35°C gave the best gloss on Nb surfaces [12]. To assess the electrochemical sensitivity to temperature, polarization measurements were taken at electrolyte temperatures of 54.6°C, 45.6°C, 33.5°C, 26.3°C and 21.3°C, as shown in Figures 5.8a and 5.8b. In order to maintain a stable temperature during the measurement, the electrochemical cell was immersed into a water bath which has the circulation of a certain proportion of hot (~70 °C) and cold (~ 17 °C) water constantly. Two thermocouples were used to monitor the temperature of the electrolyte. One was placed within 5 mm of the anode surface; the other was positioned between and equidistant from anode and cathode to record the temperature of bulk electrolyte.

All anode polarization curves exhibit a limiting current plateau. During the experiment, we noticed that the temperature of a thermocouple within 5 mm of the anode recorded a temperature greater than that of the bulk electrolyte by 0.4 °C to 6.3 °C as the bulk electrolyte temperature increased from 21.3 °C to 54.6 °C. At the two highest temperatures, the plateau current is not well defined and rises at increasing voltage. We attributed this effect to the local heating. Along the limited current region, the strong dependence of the measured anode current density on the local electrolyte

temperature is shown in Figure 5.9. Given the high sensitivity of the reaction rate to temperature, one may expect non-uniform polishing effects when local temperature conditions are not well controlled, such conditions are to be expected under practical polishing conditions when the electrolyte itself is also used as the process coolant [31]. From the cathode polarization curves (see Figure 5.8b); we also found the power dissipated on the cathode increases with electrolyte temperature. For a operation potential $\Delta V = 20$ V, the cathode polarization potential doubles as the electrolyte temperature increases from 21.3 °C to 54.6 °C. This result would be impossible to identify if only using the power supply voltage as a measurement.

5.4.5. Impedance Experiments

Impedance experiments were performed using a typical freshly prepared electrolyte of hydrofluoric and sulfuric acid by volume ratio of 1: 9 with an Nb/Al area ratio of 1: 2 under potentiostatic control. Impedance measurements were started after 120 s, the time at which a steady-state current is attained. A series of EIS measurements were made as a function of applied potential under static flow condition and are presented as Nyquist plots in Figure 5.10. In order to minimize convective diffusion caused by local heating for one set of measurements, the solution was cooled to 5.5 °C in advance and the temperature was maintained by constantly circulating ice water in an external water bath. During the measurement, no temperature increasing caused by local heating was observed through a thermocouple within 5 mm of the anode as compared with the bulk electrolyte. From Figure 5.10, we observed that the diameter of the high-frequency loop increases with

increasing applied potential, but the high frequency limit (200 kHz) of the impedance remains constant. These results will be discussed in the next section.

Impedance experiments also have been conducted during electrolyte agitation with a magnetic bar directly in the electrochemical cell. The flow rate near the anode surface was estimated to be 4~5 cm/sec, which is the scale relevant to typical nine-cell cavity horizontal EP processing [31]. The effect of electrolyte agitation on the impedance response at 9.2 °C at a potential of 7 volts is shown in Figure 5.11. The impedance response was measured as a function of voltage from 3 to 7 volt relative to MSE. At all potentials, the high-frequency limit of the impedance remained constant and the diameter of the high frequency loop increased as compared to the static conditions as summarized in Figure 5.12 and 5.31.

5.5. Discussion

The study of the mass transport mechanism in polishing systems is critical for the optimization of electrolyte formulation and of operating parameters. It has been studied theoretically and experimentally over the past several years. Several different models have been proposed, the applicability of each model to a given system is a matter for study. Grimm et al. proposed the duplex salt film model [25-27] and it was further discussed by Matlosz et al. [32]. The physical picture of this model is that the origin of the anodic limiting current is the presence of a salt film precipitate, which fixes the concentration of metal cations at its saturation value at the salt film/electrolyte interface. The rate of transport of cations across the diffusion layer

into the bulk electrolyte limits the chemical dissolution of the salt film and hence the anodic dissolution rate. The precipitate itself is viewed as being composed of two regions: the compact salt film region and porous salt film region. In the compact film region, the precipitate forms a thin solid dielectric barrier through which the cations are transported by solid-state ionic conduction. In the porous film region, the pores of the precipitate are filled with electrolyte solution at the saturation concentration of the metal cation. Mobile charge carriers (anions and cations) transport the current by migration in the electric field in the pores. The salt film need not be duplex in nature, but may consist of either a porous salt film or a compact salt film only [32]. Due to the low mobility of the ions for solid state transport, compact salt films are generally considered to have a thickness on the order of 10 nm, while a porous layer may have a thickness up to a few microns. Matlosz et al. investigated the adsorbate-acceptor model through a complete impedance analysis [10]. Contrary to the salt film model, where the surface concentration is fixed by a saturation value, the limiting current in this model is reached when the concentration of the acceptor species drops to near zero at the anode/electrolyte interface and its transport process is limited by the diffusion of the acceptor species through the electrolyte diffusion or depletion layer.

Figure 6.12 shows a schematic Nyquist plot and equivalent circuit corresponding to the high frequency part of the impedance diagram, where R_s is the solution resistance, R_p is the polarization resistance given by the diameter of circle and C_{dl} is the effective double layer capacitance C_{dl} , determined from the angular frequency at the top of the semicircle and R_p from the relation $\omega_{max} = 1/R_p C_{dl}$. The low frequency

phenomena, which for a simple salt film should yield a vertical line on the Nyquist plot and which for an acceptor diffusion-limited process should exhibit a 45° Warburg-Nernst impedance signature [10], are difficult to obtain in a polishing system undergoing high rate dissolution and are therefore not included in Figure 5.14a or the analysis of Matlosz [32].

The general responses expected for the three electropolishing mechanism following Matlosz are as follows. (1) For a compact salt film in which a solid-state conduction process occurs in parallel to capacitive charging of the film, polarization resistance, R_p increases with applied potential as the anodic film thickness grows and decreases with applied surface flow, while the interface capacitance, C_{dl} decreases with applied potential and increases with flow. (2) For a porous salt film in which ionic transport occurs in the electrolyte filling the pores of the film, the measured solution resistance, R_s increases with applied potential or increased flow condition. (3) In the case of the absorbate-acceptor mechanism without a salt film, the polarization resistance is inversely proportional to the steady-state current density and should therefore decrease with flow. Table 6.1 summarizes the results from the theoretical analyses in references [25] and [10], which can be used to determine expected trends for targeted experiments aimed at comparing impedance spectra obtained under different steady-state operating conditions. Examples are: a series of impedance diagrams obtained at different applied potentials along the limiting current plateau or a series of impedance diagrams obtained at a fixed applied potential along the limiting current plateau, but with varying electrolyte agitation.

The measured high frequency data between 0.2 Hz and 200 kHz were fitted to a semicircle to estimate solution resistance R_s , polarization resistance R_p and double layer capacitance C_{dl} . Figures 5.12 and 5.13 summarize the results for $T = 9.0 \pm 0.2$ °C for static and flowing conditions at different applied potential. The anode potential displayed in Figures 5.12 and 5.13 is ohmic (IR) corrected; the IR drop is determined from impedance measurements. By considering Table 5.1, we find that our high frequency impedance data is consistent with a compact salt film model. To summarize; we find that solution resistance, R_s remains constant at different potentials and flow rates, which rules out application of the porous salt film model. Polarization resistance, R_p increases with applied potential, while the double layer capacitance decreases. These results are consistent with the compact salt film model only. Static versus agitated electrolyte results in further support for the compact salt film model.

Results obtained in this study support that the high-rate dissolution of niobium in an electrolyte of 49% hydrofluoric and 96 % sulfuric acid of volume ratio of 1: 9 is mass-transport controlled with a compact salt film mechanism involved. Possible mass transport limiting species taking part directly or indirectly in the dissolution reaction are the cations of dissolving niobium in the anodic salt film, the electrolyte anions (SO_3^{2-} , F^-) and water molecules in the diffusion layer between niobium and bulk solution. Dilute sulfuric acid (1 M) produces the anodization of Nb to Nb_2O_5 with a corresponding rapid decay in current as the oxide film increases in thickness [34-35]. Increasing additions of HF (0.5 ~ 2 wt %) to the electrolyte results in a

corresponding increase in the steady state current under potentiostatic control [35]. This suggests that the mass transport of SO_3^{2-} anions is not responsible for the limiting current. In the presence of HF, a dielectric Nb_2O_5 film tends to be transformed into soluble fluoride or oxifluoride [14]. The anodic dissolution rate of niobium might be limited by (1) the transport of soluble Nb-fluoride or Nb-oxifluoride complex to the bulk electrolyte or (2) The transport of F^- through the diffusion layer to the electrode or (3) The transport of H_2O to hydrate the soluble niobium species so they can be transported away. In this study, the anode plateau current density is observed to fall approximately linearly with decreasing HF/ H_2SO_4 volume ratio. But, the decreasing HF content is accompanied with decreasing water content. Recently, increasing water content by adding one proportion water to the typical 1: 9 mixture HF (46 %) and H_2SO_4 (96%) was studied by F. Eozénou et.al [14]. This new mixture increases the water molar concentration from 6.72 mol/L * to 11.15 mol/L, (* The weight concentration of HF is 46 % which is lower than that of we used -J. T. Baker: 48.8 ~ 49.2 %) corresponding to the decrease of mass concentration of HF and H_2SO_4 , but with constant HF/ H_2SO_4 molar ratio. With an additional one proportion of water (H_2O : 46% HF: 96% H_2SO_4 =1:1:9), a decreasing removal rate [36], as compared with the classical 1: 9 mixture was found, and the limiting current was even less or not at all affected by stirring, as reported. In addition to the results depicted in Figure 5.6 and 5.7 that increasing HF (49%) content, contrary to the addition of water, favors high niobium dissolution rate. The low frequency response of the impedance diagram (see Figure 5.10) also suggests that the diffusion-limited

access of the F^- anion to the salt film limits the transport of dissolving across the diffusion layer into the bulk electrolyte.

5.6. Conclusions

The present data show that electropolishing of niobium in hydrofluoric and sulfuric acid electrolyte strongly depends on the local electrolyte temperature and HF/H₂SO₄ volume ratio. High frequency impedance data provide strong evidence for the presence of a compact salt film that is speculated as Nb₂O₅ in the Nb EP process in the current-limited plateau region. The available data suggests that the diffusion-limited access of the F^- anion to the salt film surface limits the local reaction rate. The knowledge of Nb EP mechanism will be very helpful for optimization of operation parameters and guiding a further study for achieving uniform polishing, which will largely improve the cavity EP production for pursuing a high reproducibility SRF performance.

5.7. References

1. P. A. Jacquet, *Nature* 135, (1935), pp. 1076.
2. A.Kutzelnigg, *Metalloberfläche* 3, (1951), pp. 867.
3. R. Weiner, *Metalloberfläche* 27, (1973), pp. 441.
4. H. Figour, and P. A. Jacquet, French Patent No. 707526, (1930).
5. V. Palmieri, *Proc. of 11th SRF workshop*, Travemünde/Lübeck, Germany (2003).
6. R.Sautebin and D. Landolt, *Electrochimica Acta.*, 129(1982), pp. 946.
7. R.Sautebin, H. Froidevaux and D. Landolt, *J. Electrochem. Soc.* 127 (1982), pp. 1096.
8. D. Landolt, *Electrochimica Acta.*, 32 (1)(1987), pp.1.
9. H. Abrams and C.L. Mantell, - *Electrochem. Tech.* 5 (1995), pp.287.
10. M. Matlosz, S. Magaino and D. Landolt, *J. Electrochem. Soc.* 141 (2)(1994), pp. 410.
11. H. Diepers, O. Schmidt, H. Martens and F.S.Sun , *Phys. Lett.*, 37(A)(1971), pp. 139.
12. K. Satio, Y. Kojima, T. Furuya, S. Mitsunobu, S. Noguchi, K. Hosoyama, T. Nakazato, T. Tajima, K. Asano, K. Inoue, Y. Iino, H. Nomura and K. Takeuchi, 2, *Proc.of 4th SRF workshop*, KEK, Tsukuba, Japan (1989).
13. E. Kako, S. Noguchi, M.ono, K. Satio. T. Shishido, H. Safa, J. Knobloch, and L. Lilje, *Proc. of 9th SRF workshop*, Santa Fe, NM (1999).

14. F. Eozénou, A. Aspart, C. Antoine and B. Maliki. CARE Report 06-10-SRF. Eu contract number RII3-CT-2003-506395 (2006).
15. C. Boffo, P. Bauer, T. Reid , and R, Geng, *Proc. of 12th SRF workshop*, Ithaca, NY (2005).
16. Solartron Analytic, "*Understanding electrochemical cells*", Technical report 17.
17. Solartron Analytic, "*An introduction to electrochemical impedance measurement*", Technical report 6.
18. Solartron Analytic, "*Analysis and interpretation of EIS data for metals and alloys*", Technical report 26.
19. Solartron Analytic, "*Use and applications of electrochemical impedance techniques*", Technical report 24.
20. J. O. Bockris, and A.K. Reddy, "*Modern Electrochemistry*", Vol. 2 Plenum Press, New York (1970).
21. A. J. Bard, and L. R. Faulkner, "*Electrochemical Methods Fundamentals and Applications*", 2nd edition, John Wiley & Sons, Inc. New York (2001).
22. S. H. Glarumm, and J. H. Marshall, *J. Electrochem. Soc.*, 132(1985), pp. 2872.
23. S. H. Glarumm, and J. H. Marshall, *J. Electrochem. Soc.*, 132(1985), pp. 2878.
24. R. D. Grimm, A.C. West and D. Landolt, *J. Electrochem. Soc.* 139(6)(1992), pp. 1622.
25. R. D. Grimm and D. Landolt, *Corr. Sci.* 36(11) (1994), pp. 1847

26. O. Piotrowski, C. Madore and D. Landolt, *J. Electrochem. Soc.* 145(7)(1998), pp. 2362.
27. S. Magaion, M. Matlosz and D. Landolt, *J. Electrochem. Soc.*, 140 (5)(1993), pp. 1365.
28. S. Park, and J. Yoo, *Analytic Chem.*(2003), pp. 455 .
29. E. Barsoukov, and J. R. Macdonald, "*Impedance Spectroscopy: Theory, Experimental, and Application*", 2nd edition, John Wiley & Sons, Inc. New York (2005).
30. B. E. Conway, "*Electrochemical Supercapacitor: Scientific Fundamentals and Technological Applications*", Kluwer Academic/Plenum, New York (1999).
31. C. E. Reece, J. Ortega and J. Mammosser, TUP 62 , Proc. of 13th SRF workshop, Beijing, China (2007),
<http://www.pku.edu.cn/academic/srf2007/proceeding.html>.
32. M. Matlosz, *Electrochimica Acta.* 40(4)(1995), pp. 393.
33. . M. A. Biason Gomes, S. Onofer, S. Juanto and L.O.de and S. Bulhões, *J. Appl. Electrochem.* 21(1991), pp. 1923.
34. I. Arsova, and J. Serb., *Chem. Soc.* 71(2), (2006), pp. 177-187.
35. I. Sieber, H.Hildebrand, A. Friedrich and P.Schmuki, *Electrochem. Comm.* 7, (2005), pp. 97.
36. H. Shou, Internal report DAPNIA, (2003).

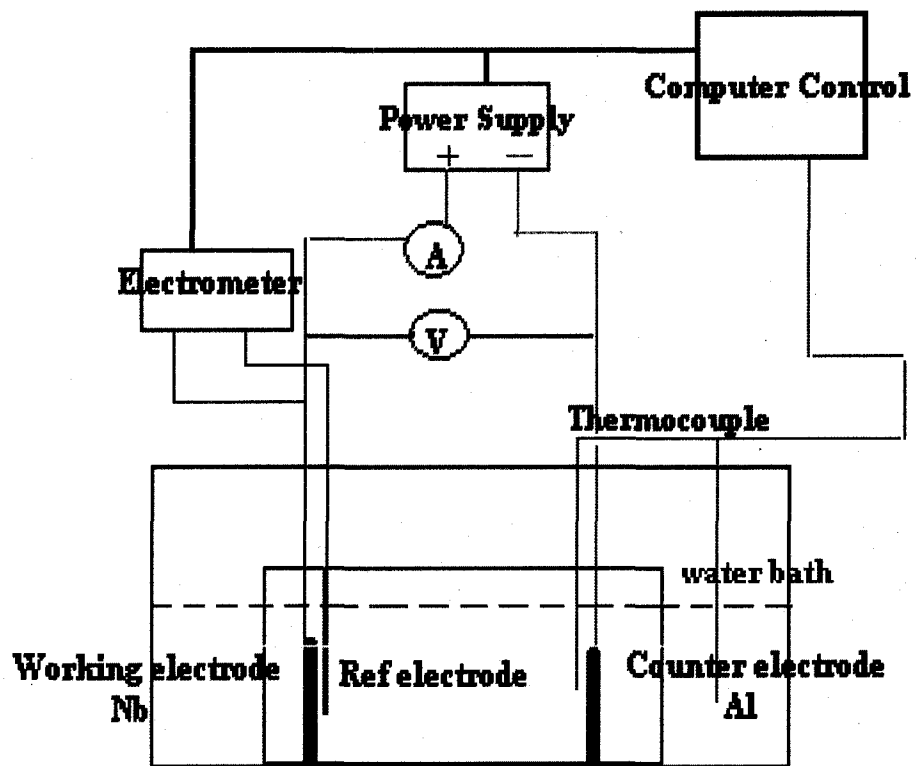


Figure 5.1: The Nb electropolishing cell set up and data acquisition scheme.

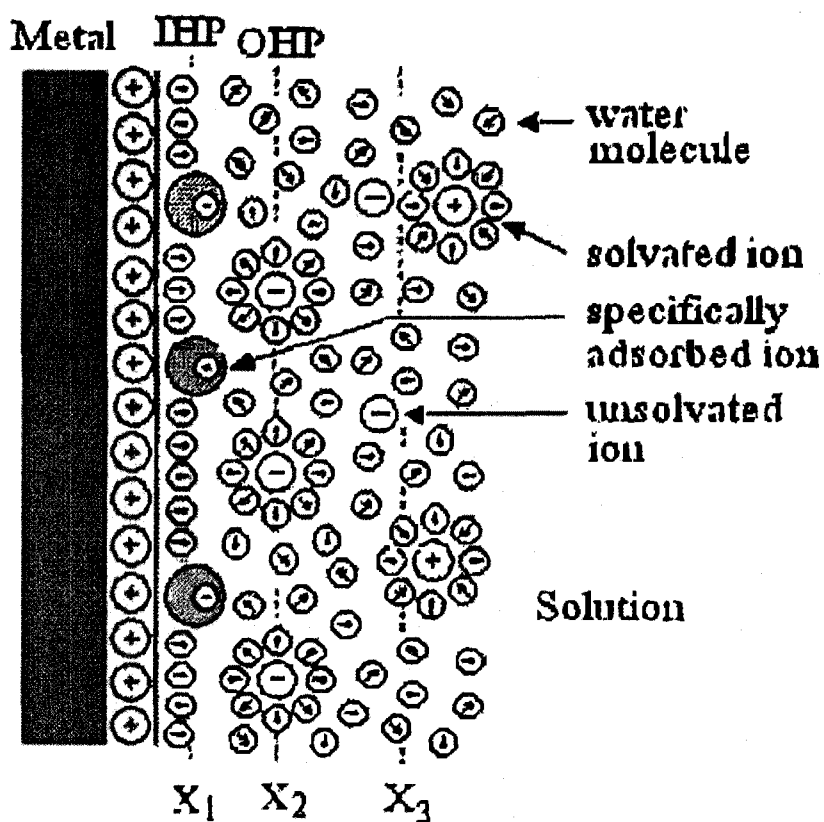


Figure 5.2: Double layer formed at the electrode-electrolyte interface (From A. J. Bard, and L. R. Faulkner, *Electrochemical Methods Fundamentals and Applications*, 2nd edition, 2001. Reprint with the permission of John Wiley & Sons, Inc)

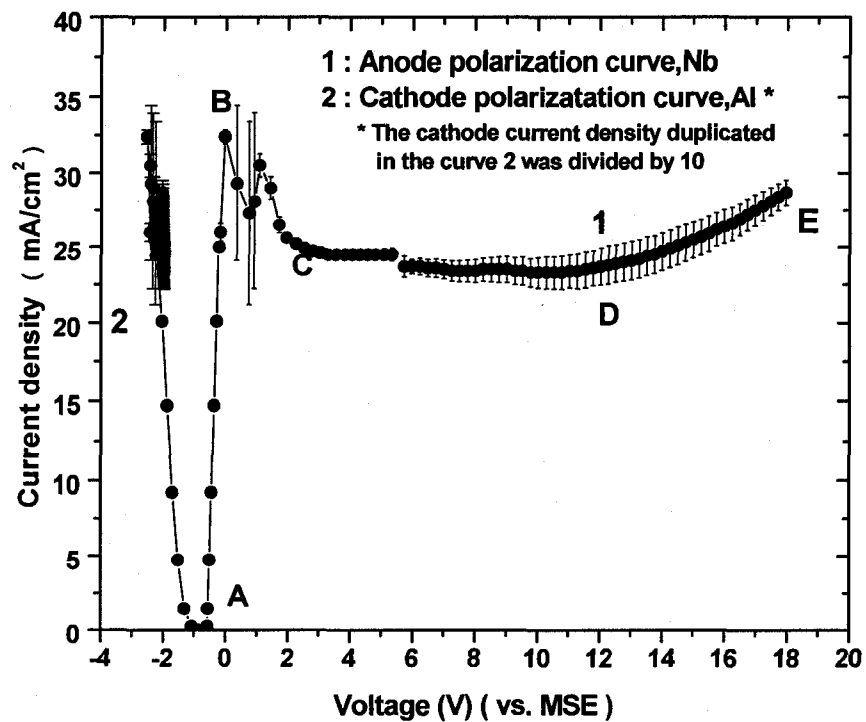


Figure 5.3: Typical polarization behavior for the Nb-Al system in HF (49%): H₂SO₄ (96%) = 1: 9 (volume ratio) at 31.5 ± 1.5 C.

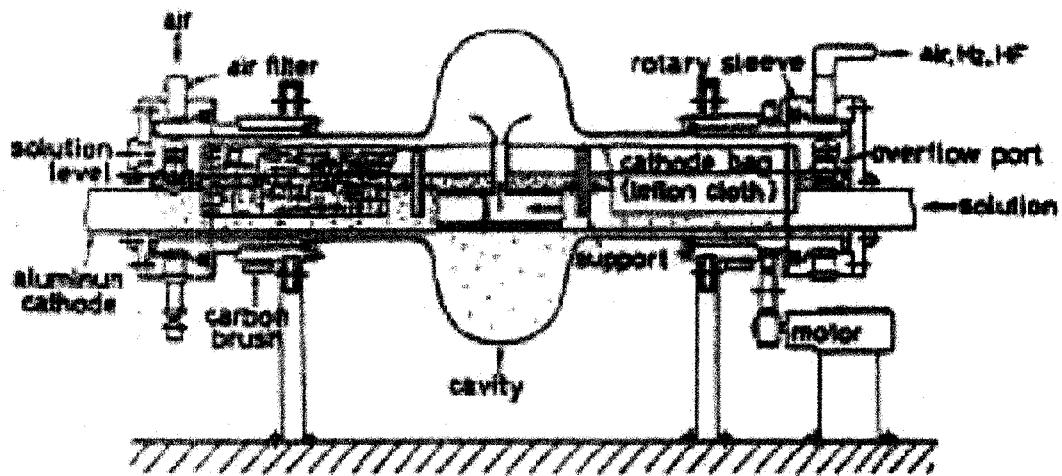


Figure 5.4: Horizontal EP set-up developed at KEK, courtesy of (From K. Satio, Y. Kojima, T. Furuya, S. Mitsunobu, S. Noguchi, K. Hosoyama, T. Nakazato, T. Tajima, K. Asano, K. Inoue, Y. Iino, H. Nomura and K. Takeuchi, *Proc. of 4th SRF workshop*, Vol .2, 1989. Reprint with permission of KEK, Tsukuba, Japan)

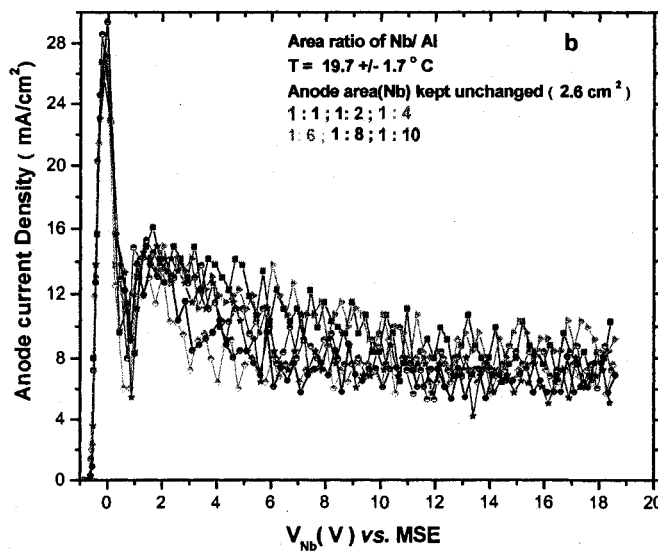
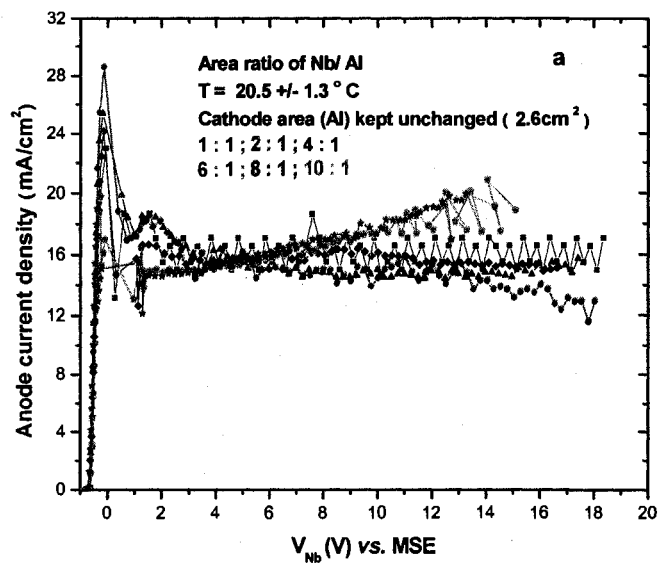


Figure 5.5: Polarization curves were determined for the different area ratio Nb and Al in 1:9 HF (49%): H₂SO₄ (96%). (Above: cathode area kept constant; below: anode area kept constant)

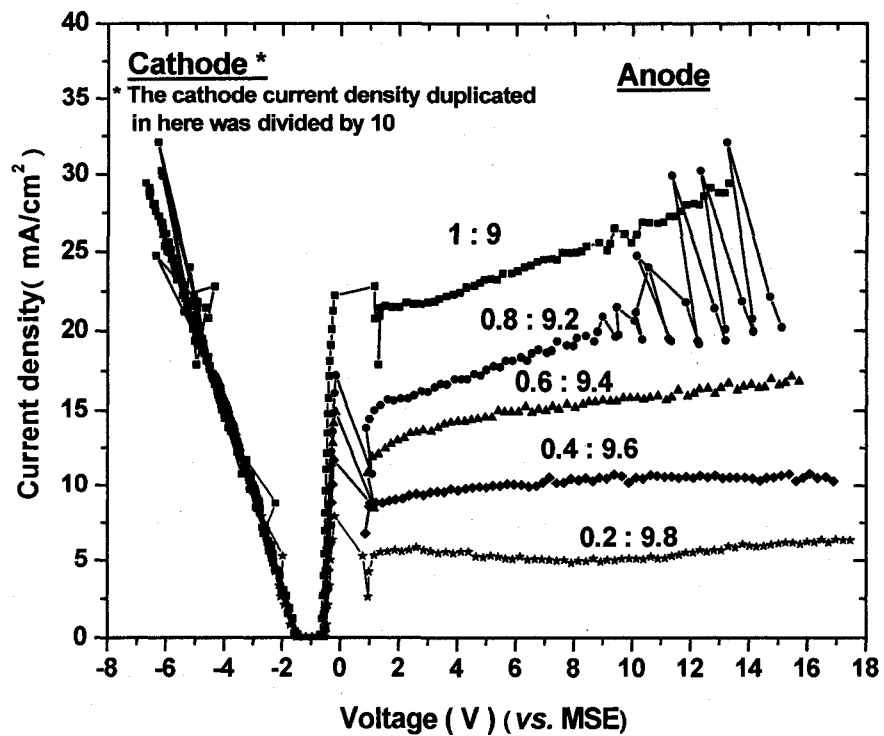


Figure 5.6: Polarization curves were determined for the Nb-Al system in different volume ratios of HF (49%): H₂SO₄ (96%).

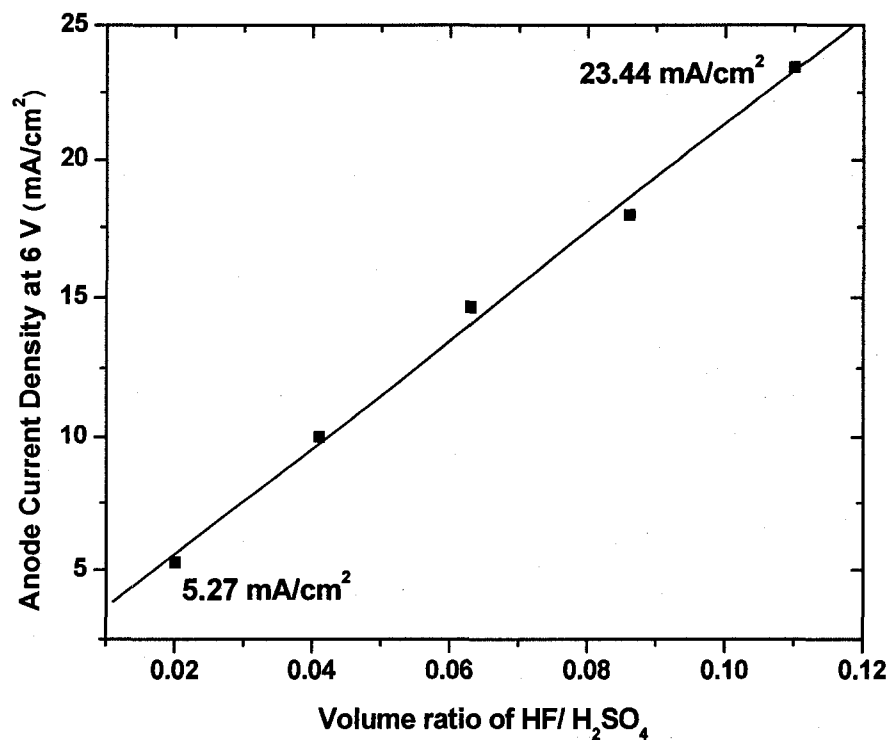


Figure 5.7: The anode plateau current density decreases with decreasing HF volume ratio. A typical 1:9 volume ratio HF and H₂SO₄ corresponds to 0.111. The data plotted below corresponds to the current density at the anode voltage of 6 V from Figure 5.6.

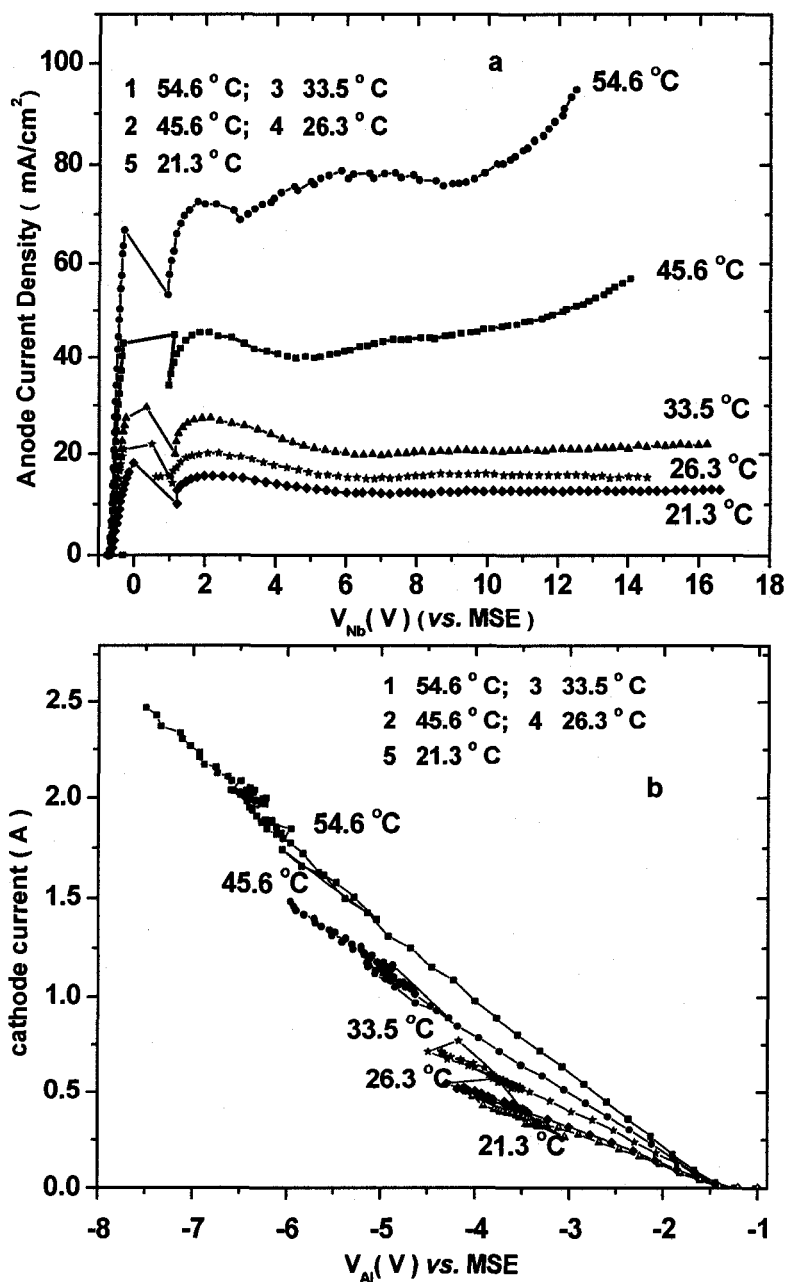


Figure 5.8: Anode (a) and cathode (b) polarization curves determined for Nb in HF (49%): H₂SO₄ (96%) = 1: 9 (volume ratio) at 54.6 °C, 45.6 °C, 33.5 °C, 26.3 °C and 21.3 °C under static electrolyte conditions.

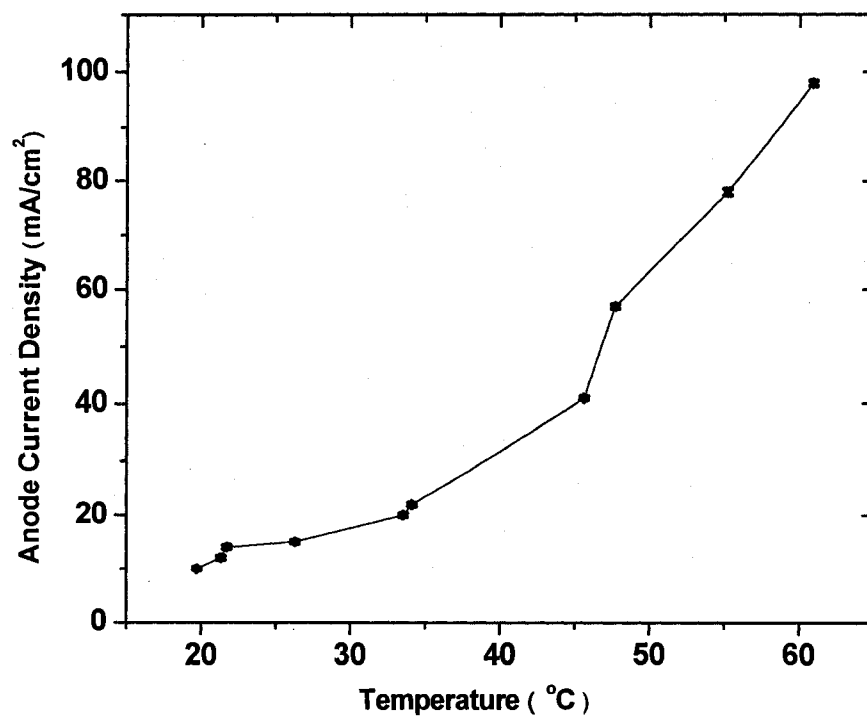


Figure 5.9: Anode current density along the limiting current region of polarization curves as a function of electrolyte temperature. Data was taken from polarization curves of Figure 5.8a.

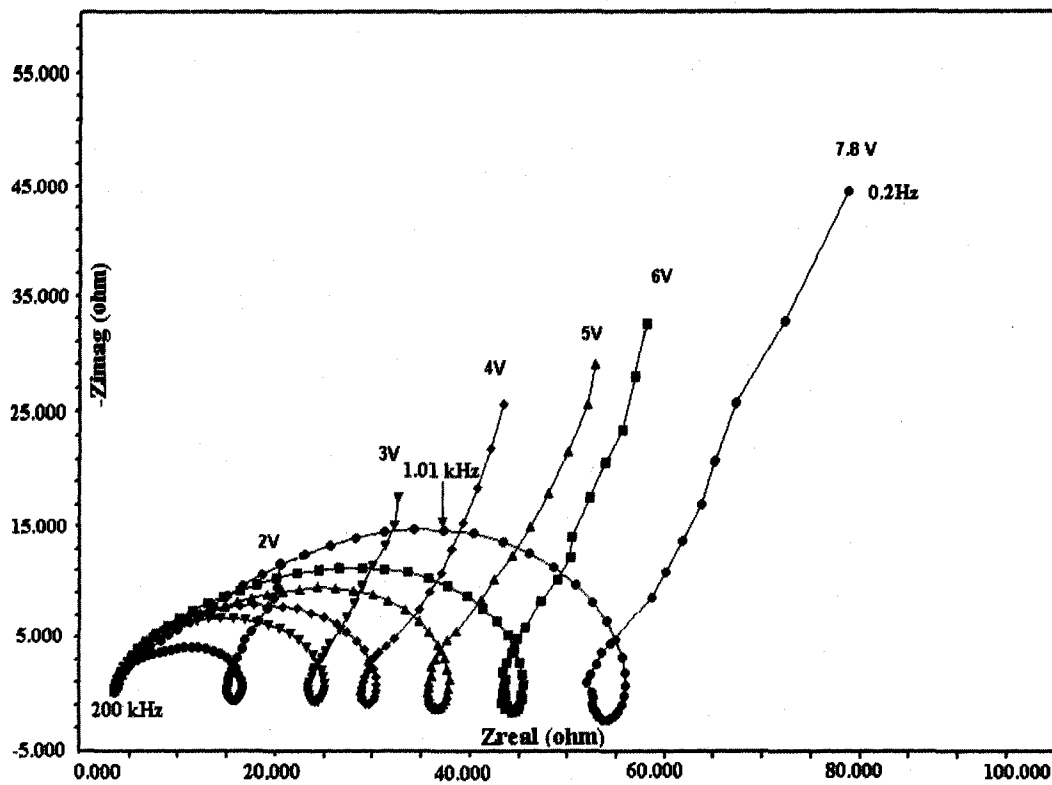


Figure 5.10: Impedance diagrams determined for Nb in HF (49%): H₂SO₄ (96%) = 1:9 (volume ratio) at different applied potential as indicated.

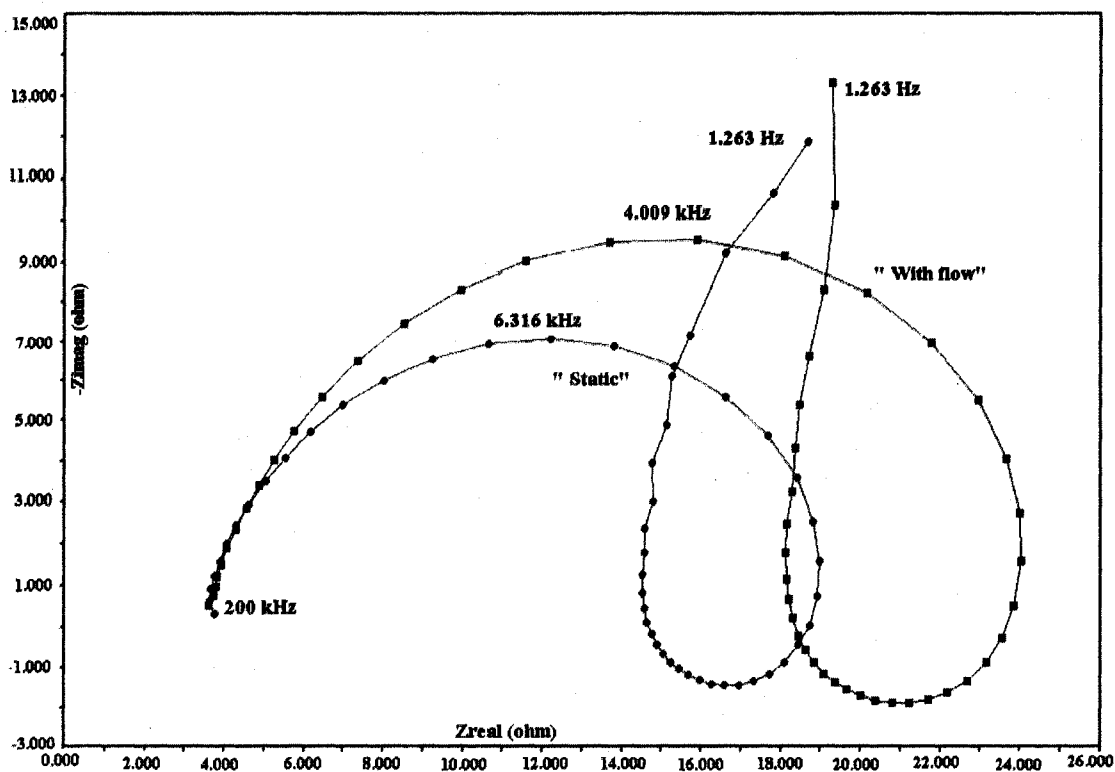


Figure 5.11: High frequency Nyquist impedance diagrams determined for Nb in HF (49%): H₂SO₄ (96%) = 1: 9 (volume ratio) at static vs. flow condition. The flow rate was estimated to be 4~ 5 cm/sec.

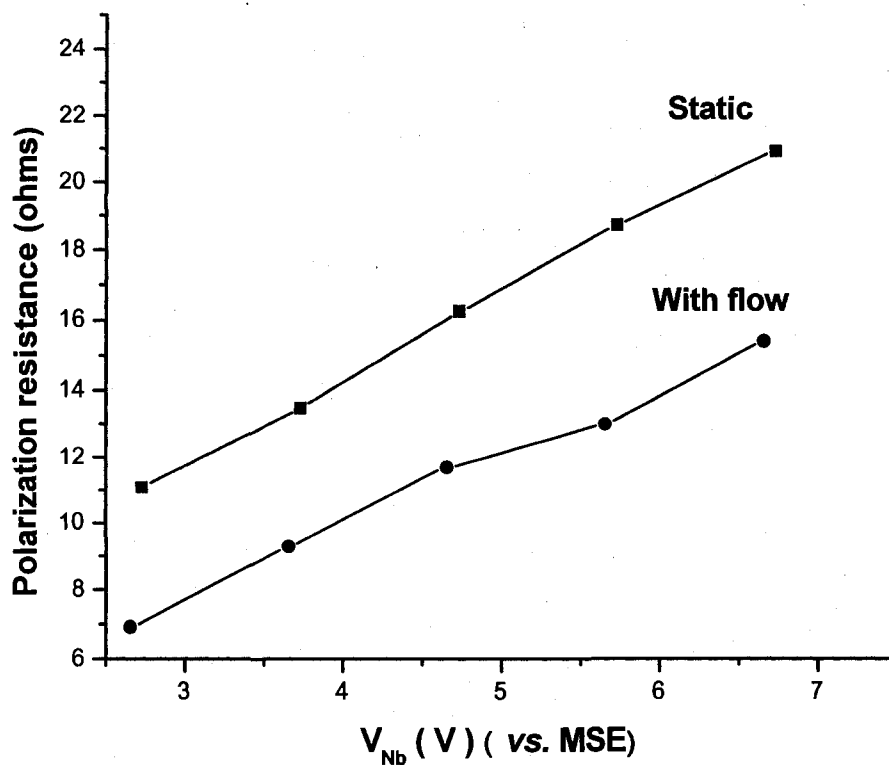


Figure 5.12: Polarization resistance (R_p) obtained from the high frequency impedance response as a function of different potential and flow rate for Nb in HF (49%): H_2SO_4 (96%) = 1: 9 (volume ratio) at 9.0 ± 0.2 °C.

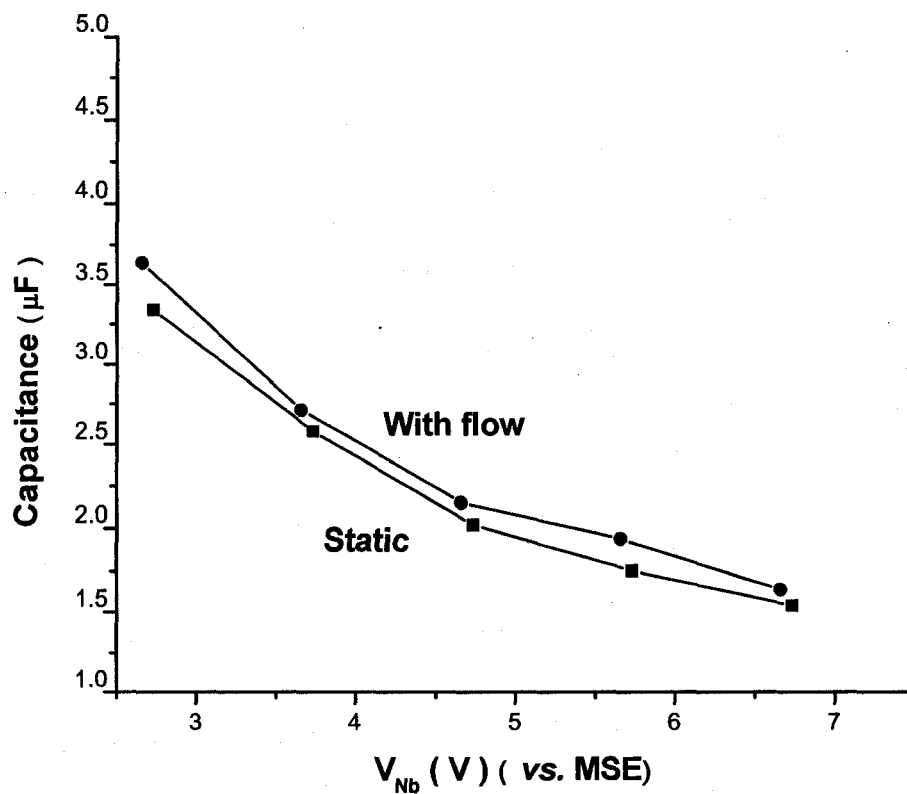


Figure 5.13: Effective double layer capacitance (C_{dl}) obtained from the high frequency loop as a function of applied potential and flow for Nb in HF (49%): H_2SO_4 (96%) = 1: 9 (volume ratio) at 9.0 ± 0.2 °C.

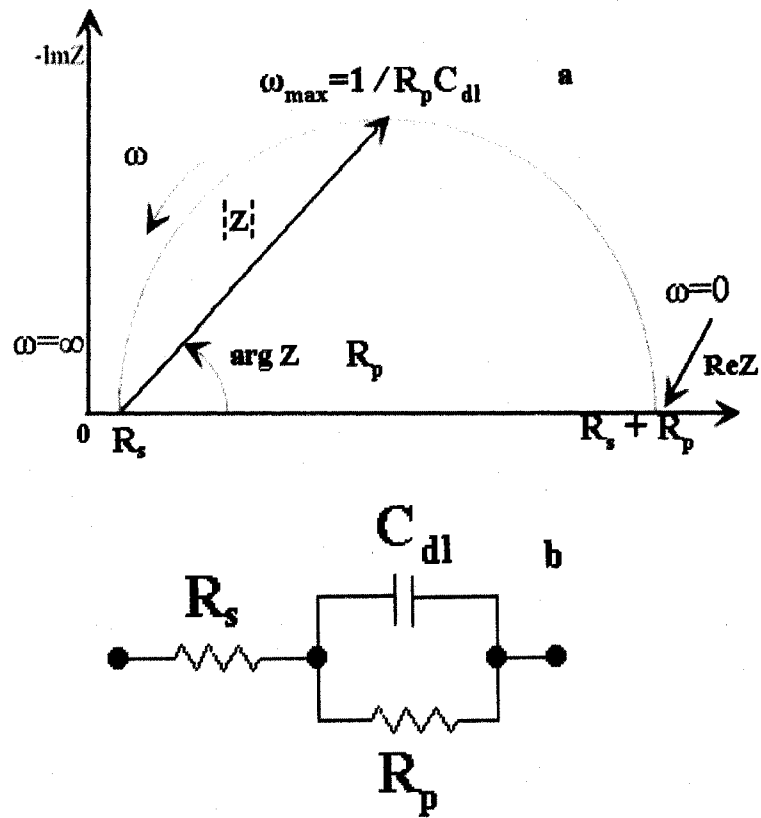


Figure 5.14: Schematic Nyquist plot (a, top) and equivalent circuit (b, bottom) corresponding to the high-frequency part of the impedance diagram.

Experimental condition	Salt film models						Adsorbates-acceptor model		
	Porous film			Compact film			R_s	R_p	C_{dl}
	R_s	R_p	C_{dl}	R_s	R_p	C_{dl}			
Potential ↑	↑	C	C	↘	↗	↘	C	C	C
Flow rate ↑	↓	↓	C	↘	↘	↗	C	↓	C

* "C" = constant; "↑" = increase; "↓" = decrease, R_s , R_p , and C_{dl} correspond to the circuit model described in Figure 8.

Table 5.1: Characteristic features of Nyquist diagram expected for various EP models obtained from the high frequency loops, (Curtsey of M. Matlosz, S. Magaino, D. Landolt, J. Electrochem. Soc., Issue 2, Vol. 141, 1994, pp. 410 and M. Matlosz, Electrochimica Acta. Issue 4, Vol. 40, 1995, pp. 393.)

Vita

Hui Tian was born in Jinchang City, Gansu Province, China on February 4, 1974. She received her B.A. in Materials Science and Engineering at Central South University in July, 1997. She received her M.S degree at Guangxi University in December, 1999, with a concentration in Materials Science. After that she was admitted to Ph.D program in the Materials Science and Engineering Department of Tsinghai University. In August, 2002, she entered the Applied Science Department of the College of William and Mary. With the completion of the thesis and satisfaction in all other degree requirements, Hui Tian received her Ph.D degree in Applied Science in August, 2008